QUANTUM CONTROL OF A MANY-BODY SYSTEM IN A SPIN-1 BOSE-EINSTEIN CONDENSATE

A Thesis
Presented to
The Academic Faculty

by

Thai M. Hoang

In Partial Fulfillment
of the Requirements for the Degree
Doctor of Philosophy in the
School of Physics

Georgia Institute of Technology
December 2013

QUANTUM CONTROL OF A MANY-BODY SYSTEM IN A SPIN-1 BOSE-EINSTEIN CONDENSATE

Approved by:

Professor Michael S. Chapman,
Advisor
School of Physics
Georgia Institute of Technology

Professor John H. Wise
School of Physics
Georgia Institute of Technology

Professor Kurt A. Wiesenfeld
School of Physics
Georgia Institute of Technology

Professor Kenneth R. Brown
School of Chemistry and Biochemistry
Georgia Institute of Technology

Professor Daniel I. Goldman
School of Physics
Georgia Institute of Technology

Date Approved: October 8, 2013

To my parents, Mr. Thuong Gia Hoang and Mrs. Tu Thi Vu

My wife, Thao Thi Nguyen

My daughter, Ngoc Minh Hoang

ACKNOWLEDGEMENTS

My graduate studies at Georgia Tech has been a wonderful and unforgettable time of my life. My doctoral journey would not have been possible without the guidance and support from many people.

My advisor, Professor Michael Chapman, has put his footprint on my every memorable moment during my time at Tech. He gave me an opportunity to join the group, despite the fact that I had no experience in atomic physics, optics, and electronics. His nonstop curiosity, patient guidance, and ability to rephrase complexity into simplicity have made this work possible. Prof Chapman has been always a supportive advisor in both academia and life, and at the same time he leaves me enough room to grow in my own way. I could not ask for a better advisor.

I would like to extend my gratitude to my committee members. It is pleasant to take a class with Prof Kurt Wiesenfeld; he has an ability to deliver a complicated subject in a way that every student can understand. I have gained useful knowledge for my research about non-linear dynamics and noise analysis from his classes. I had three classes with Prof Carlos Sa de Melo through which I learned about other many-body systems and theories besides Bose-Einstein condensate. I have not taken any astronomy related class until the cosmology and galaxy class with Professor John Wise. I gain useful knowledge about astrophysics from his class. Prof Kenneth Brown belongs to the Chemistry department; however, his quantum computing and quantum control works are quite similar to the atomic research and our works. Moreover, he is always very supportive of our group. I also would like to thanks Prof Daniel Goldman for his generosity to be on my thesis committee at the very last minute. I am very impressed with by his interdisciplinary research connecting physics to biological

organisms (lizards, crabs...) and robotics which brings physics closer to daily life.

My research briefly overlapped with Dr. Eva Bookjans who instructed me on how to run the experiment. Since the first day joining the group, I have been working closely with Dr. Chris Hamley who has been very patient to instruct me about different aspects of our experiment. I have gained useful knowledge throughout my discussions with Chris due to his expertise in electronics and physics. I am also very grateful to work with Dr. Corey Gerving and Martin Anquez. I am very impressed with Corey's early morning schedule and his ability to simplify a complicated task. Martin has been very supportive to me, and his works are always very neat. His willingness to show up early in the morning and work during the weekend has been valuable in helping take data. Benjamin Land is a very clever and talented student. He has helped me a lot in doing simulations, and we had a lot of interesting conversations about computers and programming. Our new members, Bryce Robbins and Xiaoyun Yang have adopted quickly to the group, executes their tasks neatly as they start to master their experimental skills.

In addition to BEC groups, I would like to express my gratitude to the former and present members in our lab: Dr. Michael DePalatis, Dr. Chung-Yu Shih, Dr. Michael Gibbons, and Dr. Layne Churchill. I have had a lot of interesting conversations with Michael D from Python programming, to his ion-trapping, amongst many other topics. I have not had the opportunity to work with Dr. Ming-Shien Chang; however, his well-written thesis is very instructive. I would also like to thank Dr. Rafael Hipolito for many useful theoretical discussions. I also would like to thanks Prof Maya Chhetri and Prof Joseph M. Starobin at UNC-Greensboro for their valuable instructions during my undergraduate time.

In addition, I would like to thanks my family, especial my mom and dad, for their endless support. I would like to thanks my wife for her understanding. My nephews Khanh Hoang, Anh Viet Hoang, Minh Hoang, and my daughter Ngoc Minh Hoang

who have always inspired me on my doctoral journey. I hope one day they are inspired by this thesis.

TABLE OF CONTENTS

LIST OF TABLES

LIST OF FIGURES

SUMMARY

Ultracold atoms provide a powerful tool for studying quantum control of interacting many-body systems with well-characterized and controllable Hamiltonians. In this thesis, we demonstrate quantum control of a many-body system consisting of a ferromagnetic spin-1 Bose-Einstein condensate (BEC). By tuning the Hamiltonian of the system, we can generate either a phase space with an unstable hyperbolic fixed point or a phase space with an elliptical fixed point. A classical pendulum with a stable oscillation about the "down" position and an inverted pendulum with unstable non-equilibrium dynamics about the "up" position are classical analogs of the quantum spin dynamics we investigate in this thesis. In one experiment, we dynamically stabilize the system about an unstable hyperbolic fixed point, which is similar to stabilizing an inverted pendulum. In a second experiment, we parametrically excite the system by modulating the quadratic Zeeman energy. In addition, we demonstrate rectifier phase control as a new method to manipulate the quantum states of the many-body system. This is similar to parametric excitation and manipulation of the oscillation angle of a classical pendulum. These experiments demonstrate the ability to control a quantum system realized in a spinor BEC, and they also can be applied to other quantum systems. In addition, we extend our studies to atoms above the Bose-Einstein transition temperature, and we present results on thermal spin relaxation processes and equilibrium spin populations.

CHAPTER 1

INTRODUCTION

1.1 A Brief History of Bose-Einstein Condensate

The idea of Bose-Einstein condensation (BEC) was formulated about 100 years ago by Satyendra Nath Bose and Albert Einstein in 1924-1925. In 1924, Bose sent Einstein his paper, "Planck's Law and the Hypothesis of Light Quanta," which derived Plank's distribution of light quanta, or the statistics of photons. Earlier, he could not get his paper published when he submitted it to *Philosophical Magazine*. Einstein translated the paper into German, submitted it to *Zeitschrift für Physik* for Bose, and remarked that Bose's idea was an important step forward [1]. Einstein realized that Bose's idea also could be applied to an ideal gas. He developed the statistical theory for monatomic gas that predicted that at low energy temperatures a part of an ideal gas occupies a single quantum state of the lowest energy, later called the Bose-Einstein condensate [2, 3].

It took about 70 years from the first theoretical prediction of Einstein to the first observation of the Bose-Einstein condensate by groups at NIST-JILA, MIT, and Rice [4, 5, 6]. The first BECs were created in magnetic traps [4, 5, 6]; Georgia Tech was the first to create a BEC using an all optical trap [7].

Extending Bose's work for massless photons, Einstein derived the statistics for a Bose gas whose spin is an integer number. The prediction of Bose-Einstein condensation comes from the equation of the average number of particles [2, 8]

$$\langle N \rangle = V \left(\frac{2\pi m k_B T}{h^2} \right)^{3/2} g_{3/2}(z) + \langle N_0 \rangle \tag{1.1}$$

where N is the total number of atoms, V is the volume, T is the temperature, k_B is the Boltzmann's constant, h is the Planck's constant, m is the mass of atom, $\langle N_0 \rangle$

is the number of particles in the ground state, and the function $g_\nu(z)$ called the Bose-Einstein function [8], and is defined as

$$g_\nu(z) = \frac{1}{\Gamma(\nu)} \int_0^\infty \frac{x^{\nu-1}}{z^{-1}e^x - 1} dx \tag{1.2}$$

The integral part is a polylogarithm, a special function called Jonquière's function [9], the variable z is the fugacity of the gas, $z = \exp(\mu/k_B T)$, and $\Gamma(\nu)$ is the Gamma function.

For a real physical system, the function $g_{3/2}(z)$ is finite for any given N, V and T; hence the value of fugacity must be $0 \leq z \leq 1$. This condition implies that the function $g_{3/2}(z)$ is bounded and has its maximum at $g_{3/2}(1) = \zeta(3/2)$. The Riemann zeta function is approximated as $\zeta(3/2) = 2.612$. Substitute back into Eqn 1.1,

$$\langle N \rangle \leq V \left(\frac{2\pi m k_B T}{h^2} \right)^{3/2} \zeta(3/2) + \langle N_0 \rangle \tag{1.3}$$

In Eqn 1.3, when the number of particles N and the volume V are fixed, and the temperature T is decreasing, at one point we have

$$\langle N \rangle \geq V \left(\frac{2\pi m k_B T}{h^2} \right)^{3/2} \zeta(3/2) \tag{1.4}$$

To satisfy the condition in Eqn 1.3, atoms must fall into the ground state; in other words, a portion of atoms will form a Bose-Einstein condensate. When the temperature is at absolute zero, all the atoms will remain in the BEC. A critical temperature for BEC can be extracted from Eqn 1.4

$$T_c = \left(\frac{\langle N \rangle}{V \zeta(3/2)} \right)^{2/3} \frac{h^2}{2\pi m k_B T} \tag{1.5}$$

In a unit of the thermal de Broglie wavelength $\lambda_{dB} = \frac{h}{\sqrt{2\pi m k_B T}}$, boson gas particles start to form a BEC when the distance between particles is less than λ_{dB}. Rewriting Eqn 1.4 in term of λ_{dB}, the relation between separation of particles and the thermal de Broglie wavelength of the condensate is

$$\langle N \rangle \geq \frac{V \zeta(3/2)}{\lambda_{dB}^3} \qquad \text{or} \qquad n\lambda_{dB}^3 \geq 2.612$$

The quest for the Bose-Einstein condensate was triggered in the 1970s by a number of experimental groups [10]. BEC can be achieved by increasing the density of particles and reducing the temperature to give a longer de Broglie wavelength. However for traditional gas at low temperatures, it would make the transition to liquid and solid first. Liquid and solid have strong interactions between particles while the BEC model is based on a non-interacting ideal gas and is also proposed as mechanism for superfluidity in ^{4}He [11]. For this reason, searching for a chemical substance that can remain in the gas phase near zero temperature seemed to be the key to create a BEC. Hecht (1959) and Stwalley-Nosanow (1976) suggested that spin-polarized hydrogen gases would never become liquid, but remain as a gas at any temperature [12, 13]. Different groups started to search for the BEC by cooling hydrogen in a liquid helium cell [14, 15, 16, 17] ; hydrogen atoms were cooled by exchanging heat with the liquid helium wall. However, making the BEC in hydrogen atoms is extremely difficult. Firstly, the density required for a hydrogen BEC is too high so that the three-body recombination become dominant. Secondly, to create BEC at low density, the temperature of the hydrogen gas must be reduced; however, this leads to three-body recombination due to the high surface density of the hydrogen atoms [18]. Therefore, a different approach is necessary to solve the problem.

With the breakthroughs in laser cooling developed by 1997 Nobel laureates Chu, Cohen-Tannoudji, Phillips [19, 20, 21] , and others, lasers quickly became a workhorse in the BEC quest. Laser cooling together with a magnetic coils trap, known as a magneto optical trap (MOT), can trap and cool atoms to the mK regime [22]. To achieve a BEC, a technique called evaporative cooling is applied. During this process, the potential well of the trap is adiabatically lowered such that hot atoms with high kinetic energy escape from the trap, resulting in a Bose-Einstein condensate of very cold atoms. In 1995, three groups reported the evidence of Bose-Einstein

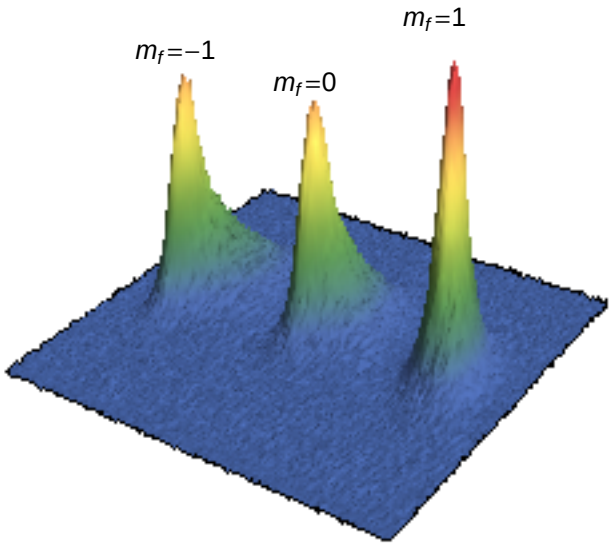

Figure 1.1: Momentum distribution of spinor BEC. Image of BEC after 22 ms time of flight. Three peaks show the density plot of BEC components which separate by Stern-Gerlach gradient.

condensate in rubidium, sodium, and lithium gases [4, 5, 6]. The problem of three-body recombination was solved by using alkali gases at low density (10^{14} cm^{-3}) in ultrahigh vacuum. To account for the low density, the temperature of the gas was cooled to the nK regime so that the thermal de Broglie wavelength was larger than the separation between the atoms. Bose-Einstein condensate in hydrogen was eventually achieved in 1998 [23]. The achievement of BEC was recognized by the Nobel prizes for Cornell, Ketterle, and Wieman in 2001. An image of a spin-1 condensate of ^{87}Rb atoms from our lab is show in Figure 1.1. The three peaks correspond to the three spin component, $mf_f = 0, \pm 1$, which are separated by Stern-Gerlach fields following a release from the trap.

1.2 Early Bose-Einstein Condensate

The achievement of BEC opened up a new era for ultracold atomic research. Early BECs were created in magnetic traps, later in an optical trap [24], and in all optical trap in our lab [7]. In the trapping potential at the lowest energy state, the condensate can be treated as a quantum harmonic oscillator. The condensate can be excited to higher energy modes by modulating the trapping potential. The energy excitation in the density oscillation is an analog of the phonon effect in superfluid helium or sound waves [25] and parametric excitation of the spatial mode [26, 27] of a condensate. Moreover, the fundamental phenomenon of liquid, and superfluid, vortices can exist in the condensate. By stirring the condensate, angular momentum is added to the condensate. The vortices corresponding to the quantized angular momentum can be observed as empty holes in the middle of the condensate [28, 29, 30].

A BEC condensate lives in the quantum world where the wave function is sufficient to describe all the quantum aspects of the condensate. An individual Bose condensate atom has a wave function overlapping, and a system of many-body atoms superimposes the wave functions into a macroscopic quantum object. The comparable length scale of de Broglie wavelength and the separation between atoms makes it a perfect candidate for studying wave-particle duality. Made from atoms, the BEC inherits all the physical properties of particles, for example, the mass and volume. The wavelike properties of condensate come from the thermal de Broglie wavelength. The interference between two condensates was first observed at MIT [31], and the interference of the double slit condensates was demonstrated at the Max Planck Institute [32]. The condensate with a same overall wave function is a macroscopic coherent source of matter wave which suggests atom laser applications of the condensate [33, 34, 35]. The wave-like characteristics allow a condensate to overcome the limits set by classical physics. The condensate can tunnel through a potential barrier which is prohibited by the classical relation of potential and kinetic energy [36, 37].

Like any other physical system, the quantum phase transitions in Bose-Einstein condensate are fundamental phenomena. The quantum phase transitions, including the transition from bose gas to Bose-Einstein condensate [8], the transition from superfluid to Mott insulator [38], and the ground state phase transition [39, 40, 41], allow the study of universality in a condensate.

1.3 Spinor BEC

One advantage of a BEC in an optical trap is the ability to confine multiple Zeeman sub-level spin components [24]; this triggered some of the early work in spin domains [42, 43], Feshbach resonances [44], and spin relaxation [45]. Later more phenomena have been observed and investigated in spinor BECs including quantum phase transitions by quenching magnetic fields [46, 47, 48] or tuning the interaction strength [49], spinor population dynamics [50, 51, 52, 53, 54, 55], and spin squeezing [56, 57, 58, 59, 60].

In this section, we introduce some of the background work related to the study of this thesis including spin population dynamics and squeezing.

1.3.1 Spin Population Dynamics

In 2001, the first all optical BEC was created in our lab [7] by laser cooling rubidium atoms to the mK regime and evaporative cooling to the nK regime in a CO_2 laser optical dipole trap. This method could possibly create a BEC for any species of atoms possessing an electric dipole moment [7]. Also, the optical dipole trap enables the study of spinor dynamics of the condensate [50, 51]. Similar works have also been done by other groups for Rb and Na [52, 53, 54, 55].

For a spin-1 system, there are 3 possible Zeeman levels of spin states $m_f = 0, \pm 1$. The spin exchange occurs through atom collisions as $2|0\rangle \rightleftharpoons |1\rangle + |-1\rangle$. The magnetic field contributes linear and quadratic Zeeman energy to the spinor Hamiltonian. In order for spinor dynamics to happen, the spinor energy must be a dominant term;

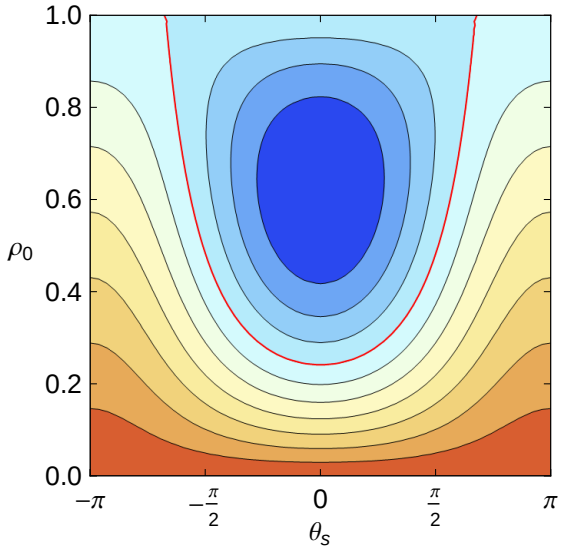

Figure 1.2: Spinor phase space. Spinor energy contours in spinor phase space for $B = 0.22$ (G). The red curve represents the separatrix (zero energy contour). Negative energy contours (blue region) are inside the separatrix, and positive energy contours (red region) are outside.

otherwise the equilibrium ground state will be $|f = 1, m_f = 0\rangle$ [50, 22] due to the high magnetic field. For our condensate, the spinor energy is less than 10 Hz. In order for spinor dynamics happens, the magnetic field should be in the μG regime [50, 22]. Zeroing magnetic field to the μG regime is a technical challenge. However, conservation of magnetization $m = 0$ cancels the linear Zeeman effect and leaves the quadratic Zeeman. The quadratic Zeeman effect is much smaller compare to the linear effect. This allows the observation of spinor dynamics, spin mixing and coherent oscillation in the mG to G regime [50, 22].

Spin mixing dynamics evolves along the separatrix (zero spinor energy contour, red curve in Figure 1.2), and coherent oscillation dynamics evolves along the nonzero energy contours on spinor phase space $\theta_s\rho_0$. Here, the spinor phase is the relative phase of spinor components, $\theta_s = \theta_1 + \theta_{-1} - 2\theta_0$. The example of population dynamics $\rho_0 = \frac{N_0}{N}$ of spin mixing is shown in Figure 1.3. The condensate is initiated in $m_f = 0$

state at high magnetic field $B = 2$ G. The dynamics are triggered by lowering magnetic field to $B = 0.22$ G. In the spin-nematic phase sphere $S_\perp Q_\perp x$, the condensate is initiated at the unstable hyperbolic fixed point Figure 1.4 (left). The uncertainties in the distribution drive the condensate out of the equilibrium point by squeezing along the separatrix Figure 1.4 (right). During the first 100 ms, the population ρ_0 is paused, then it starts to oscillate. Moreover, the distribution of ρ_0 population, standard deviation $\delta\rho_0$, and it higher moments possess a non-Gaussian distribution during spin mixing evolution [61].

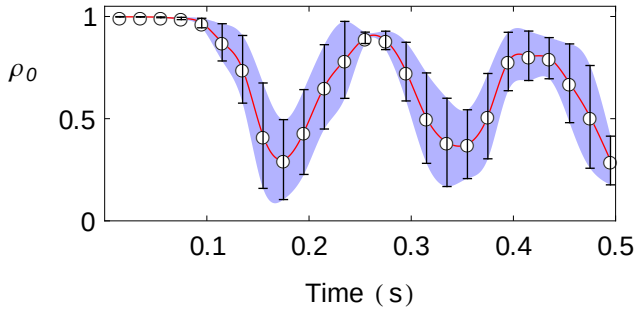

Figure 1.3: Quantum spin mixing. Dynamics of population $\rho_0 = N_0/N$ during spin mixing for $B = 0.22$ G.

1.3.2 Spin-Nematic Squeezing

In spin-1 system, beside three spin operators $\{S_x, S_y, S_z\}$, there are five other quadrupole operators $\{Q_{xx}, Q_{yy}, Q_{zz}, Q_{xy}, Q_{xz}, Q_{yz}\}$ in order to describe the system. We will discuss the details of these operators later; however, we can think of spin operator as the magnetic dipole moment and quadrupole operator as the magnetic quadrupole moment. Since the Hamiltonian matrix of the interaction is traceless and symmetric, only five of those operators are linearly independent [56]. From these operators, there are seven SU(2) subspaces [56]. For atoms in $|m_f = 0\rangle$, there are only two subspaces whose commutators has the non-zero expectation values. If the expectation values of the commutators are zeros, the uncertainty would always be greater than or equal

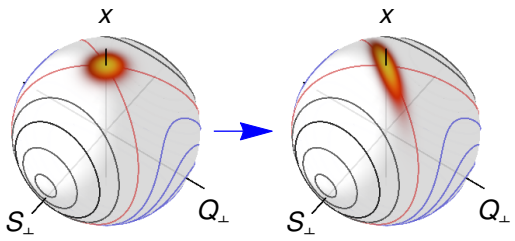

Figure 1.4: Spin-Nematic Phase Sphere. (Left) Initial distribution in spin-nematic space with uncertainty equal to SQL ($1/\sqrt{N}$). (Right) Squeezing along separatrix in spin-nematic phase space results in the uncertainty below SQL on the axis perpendicular to the divergent separatrix.

to the standard quantum limit (Heisenberg uncertainty limit). Therefore, there is no squeezing if the expectation value of the commutator is zero. We are only searching for squeezing in the subspaces $(S_x, Q_{yz}, Q_{zz} - Q_{yy})$ and $(S_y, Q_{xz}, Q_{xx} - Q_{zz})$ where the expectation values of commutators are non-zero. Since the dynamics in these two spaces are degenerate, we introduce the variable $S_\perp^2 = S_x^2 + S_y^2$, $Q_\perp^2 = Q_{xz}^2 + Q_{yz}^2$, and $x = 2\rho_0 - 1$ to reduce the dynamics into a single spin nematic $S_\perp Q_\perp x$ space. The cartoon demonstration for squeezing in the $S_\perp Q_\perp x$ spin-nematic sphere is shown in Figure 1.4.

An improvement of imaging detection and the studying of sub-Poissonian spin correlation [62] show that the detection noise is below the standard quantum limit (SQL). This enables the observation of spin-nematic squeezing [56] in a spin-1 system. Squeezing happens during the first 100 ms pausing of spin mixing (Figure 1.3). Initially the distribution of condensate has an uncertainty ($\sqrt{N}$ atoms) at the SQL located at an unstable hyperbolic fixed point on the top pole of the $S_\perp Q_\perp x$ sphere as shown in Figure 1.4 (left). As the dynamics freely evolve, the distribution squeezes along the separatrix. The uncertainty grows on the divergent separatrix and squeezes below the SQL on the transverse axis as shown in Figure 1.4 (right).

1.3.2.1 *Definition of Squeezing*

The idea of squeezing is very easy to be misunderstood. In quantum optics, squeezed states have been studied in an electromagnetic field [63]. In the second quantization, the field can be represented as annihilation and creation operators $\hat{a}_k$ and $\hat{a}_k^\dagger$ where k is a wave vector. The commutation of these operators follows the boson relations $[\hat{a}_k, \hat{a}_k^\dagger] = \delta_{k,k'}$. The electromagnetic field can be decomposed into the real and imaginary parts using the quadrature operators defined as [64, 65],

$$\hat{Q}_1 = \frac{1}{\sqrt{2}}\hat{a} + \hat{a}^\dagger \qquad \hat{Q}_2 = -\frac{i}{\sqrt{2}}(\hat{a} - \hat{a}^\dagger) \qquad \left[\hat{Q}_1, \hat{Q}_2\right] = i$$

The generalized uncertainty principle requires that

$$\langle(\Delta\hat{Q}_1)^2\rangle\langle(\Delta\hat{Q}_2)^2\rangle \geq \frac{1}{4}|\langle[\hat{Q}_1, \hat{Q}_2\rangle|^2 = \frac{1}{4}$$

An electromagnetic field is said to be squeezed if the uncertainty in one of the quadratures is less than the standard quantum limit (SQL) [66]

$$\langle(\Delta\hat{Q}_1)^2\rangle \leq \frac{1}{2}|\langle[\hat{Q}_1, \hat{Q}_2\rangle| = \frac{1}{2}$$

For a spin-$\frac{1}{2}$ system, one can reduce the uncertainty of the quadrature to less than the SQL by choosing an appropriate coordinate system[67], for instance, rotating a coherent spin state (CSS). As another example, a circle becomes ellipse if we look at it from an angle. The circle itself does not squeeze. Therefore, solely based on the uncertainty of quadrature will not be a fundamental definition of squeezing state.

To establish a more appropriate definition for a squeezed state, let look at a spin-S system. A spin-S system can be thought as a set of 2 S elementary $\frac{1}{2}$ spin [67]. The commutation relations read

$$\left[\hat{S}_i, \hat{S}_j\right] = i\epsilon_{ijk}\hat{S}_k$$

where the indices i, j, k denote the orthogonal spin directions. The generalized uncertainty principle reads

$$\langle(\Delta\hat{S}_i)^2\rangle\langle(\Delta\hat{S}_j)^2\rangle \geq \frac{1}{4}|\langle[\hat{S}_i, \hat{S}_j\rangle|^2 = \frac{1}{4}|\langle\hat{S}_k\rangle|^2$$

Let k be the mean spin direction of the S-spin; the indices i, j thus become the normal components. If all elementary $\frac{1}{2}$ spins are uncorrelated, the spin variance of the system is the sum of the individual variance of $\frac{1}{2}$ elementary spin. The variance is $\frac{S}{2}$ which is also a SQL. If there are correlations between the elementary $\frac{1}{2}$ spins, the uncertainty could be reduced less than the SQL in the one of the normal components and grow in another component. The S-spin state then is the squeezed state. This definition of a squeezed state requires a definite coordinate system where squeezing quadrature axes are defined. In this case, one of the coordinate components is the mean spin direction. For a spin-$\frac{1}{2}$ system, squeezing does not occur under the spin rotational Hamiltonian. To create squeezing, the nonlinear interaction should be added to the system [67].

1.4 Motivation and Contribution

Ultracold gases have shown to be one of the greatest candidates for studying quantum control of interacting many-body systems with a well-characterized and controllable Hamiltonian [68]. In a spin-1 ferromagnetic condensate, the quantum phase transition tunable through the quadratic Zeeman energy of the magnetic field [46, 47, 48].

When the magnetic field B is small such that the quadratic Zeeman effect $q = q_Z B^2 < 2|c|$, there exists an unstable equilibrium hyperbolic fixed point at the top pole of the spin-nematic $S_\perp Q_\perp x$ sphere. The dynamics of the condensate are an analog of an inverted pendulum. Here, the quadratic Zeeman constant $q_Z \approx 71.6$ Hz/G^2. The non-equilibrium dynamics can generate squeezed states [56, 57, 58, 59, 60] which preserve the uncertainty below the standard quantum limit (SQL). The non-Gaussian states of non-equilibrium dynamics [61] are the potential resources for quantum enhanced measurements [69] and quantum information processing [70].

When the magnetic field is high such that the quadratic Zeeman effect $q = q_Z B^2 >$

$2|c|$, there exists a stable equilibrium elliptic fixed point at the top pole of the spin-nematic $S_\perp Q_\perp x$ sphere and the dynamics of the condensate are an analog of a classical pendulum. The coherent spinor dynamics [51] is the result of stable equilibrium about elliptical fixed point.

The ability to control the quantum phase generates different scenarios of quantum spin dynamics and is a great framework to study various control techniques in a many-body system. In this thesis, we demonstrate the quantum control techniques by stabilizing non-equilibrium dynamics, parametric exciting an equilibrium coherent oscillation, and rectifier phase control of coherent oscillation explored in a spin-1 ferromagnetic Bose-Einstein condensate. In addition, we investigate the spin relaxation in the finite temperature atoms above the BEC critical transition temperature.

1.4.1 Dynamic Stabilization

Stabilizing an unstable equilibrium system by external periodic forcing is a non-intuitive physical phenomenon. This idea introduced a new concept of stabilization method for a physical system, a dynamical stabilization instead of a static stabilization. Over 100 years ago, the first demonstration was the stabilization of an inverted pendulum ('Kapitza's pendulum') by vibrating its pivot point [71]. Understanding the dynamic stabilization of an unstable system is an important area in control theory not only for classical systems but also for quantum system. In atomic physics, the rf ion traps, mass spectrometers [72], and particle synchrotron [73] all relate to the idea of dynamical stabilization. In Bose-Einstein condensates, the non-equilibrium dynamics can be stabilized by tuning the sign of the scalar [74, 75, 76] and spin-dependent interaction strength [77]. In a double well BEC [78, 79, 80], the stabilization uses the time-varying the trapping potential. The dynamic stabilization can also control the superfluid-Mott insulator phase transition in the optical lattice systems [81].

In this thesis, we demonstrate the dynamic stabilization on the internal spin states

of a strongly interacting quantum many-body system by periodic manipulation of the spinor phase of a Bose-Einstein condensate [82]. The condensate is initial at the unstable hyperbolic fixed point on the spin-nematic phase space. The uncertainty in states distribution around the unstable hyperbolic fixed point leads to the evolution dynamics of squeezing [83, 56] and quantum spin mixing [84, 50, 85, 61]. Periodic microwave pulses are applied to rotate the phase of the states away from the divergent separatrix to keep its dynamics about the hyperbolic fixed point. A similar experimental concept was applied in nuclear magnetic resonance (NMR) [86] and bang-bang control of non-interacting two-level quantum systems (qubits) [87].

1.4.2 Parametric Excitation

Parametric excitation phenomenon was first scientifically observed by Michael Faraday (1831) in vibrating fluid tanks [88] and was generalized by Lord Rayleigh (1883) [89]. Parametric excitation occurs in oscillating systems where a parameter of the dynamics are varied periodically [90]. It is observable in various systems from a child on a swing, to the fifth century B.C. Tibetan singing bowls [91], to the collective excitations of Bose-Einstein condensate density modes [26, 27]. In superconducting systems, the Shapiro resonance [92] was suggested as a source for parametric amplification in theory and experiment [93, 94], with the plasma oscillation of the Josephson junction [95] as the input source and an external signal as a pump. Parametric phenomena in atomic systems have also been observed in the photon-assisted tunneling by modulating the local interaction-tunneling constant in optical lattices [96, 97], the photon-assisted superexchange by modulating tunneling constant in double well systems [98], and the coherent super Bloch oscillations by modulating an optical lattice potential [99, 100, 101, 102].

Parametric excitation is a primarily classical phenomena, but one wonders whether it could be observed in a system where a quantum description is most applicable. In

this thesis, we demonstrate parametric excitation in a quantum many-body system, a spin-1 Bose-Einstein condensate. We will discuss the parametric excitation in terms of the semi-classical theory and the quantum Fock state.

1.4.3 Rectifier Phase Control

There exists a stable elliptical fixed point in the spin-nematic $S_\perp Q_\perp$ phase space of spinor condensate for $q > 2|c|$, and the coherent oscillation follows the elliptical energy contours. In spinor phase space $\theta_s \rho_0$, the population ρ_0 dynamics can be decomposed into an ac coherent oscillation with a dc offset. By applied the $\Delta\theta_s = -\pi$ spinor phase shift at the right moment during coherent oscillation, one can transfer a condensate between energy contours. This is equivalent to changing the dc offset of the coherent oscillation. The ability of moving a condensate across energy contours is another method to control the state of spinor system. This technique is the rectifier control. In electronics, a rectifier is the device which converts alternative current (ac) to direct current (dc).

1.4.4 Thermal Spin Relaxation

There are several reasons that thermal atoms above BEC critical temperature are interesting to us. Creating a thermal cloud at finite temperature is easier than making a BEC. The trap lifetime of a thermal cloud is longer than that of a BEC; therefore, the cold atoms could be practical in application. We have investigated different aspects of spinor BEC but not on the thermal atoms. Understanding thermal spin relaxation is one of first steps into the study of thermal atoms.

CHAPTER 2

THEORY OF SPIN-1 CONDENSATES

The theory of Bose-Einstein condensation has a long history and evolves along with the development of modern physics. At the beginning, the theory was based on statistical mechanics and the idea of energy quantization [1, 2, 3]. The emergence of quantum mechanics from classical mechanics introduced the idea of the Schrödinger equation and the wave function. Consequently, Bose-Einstein condensate, a many-body system in the presence of potential energy, is described by the Gross-Pitaevskii equation [103, 104]. Furthermore, by adopting the idea of quantum field theory, the Gross-Pitaevskii equation can be written in the second quantization form [105, 84, 106] where the basis represents the number of particles in each state. For a spin-1 BEC, second quantization enables us to write the Hamiltonian in terms of the spinor field operators $|m_f = 0, \pm 1\rangle$ and separate the spin-independent and spin-dependent parts of the Hamiltonian. The single mode approximation reduces the spatial mode and simplifies the Hamiltonian into the internal spinor modes [107, 105, 84, 108]. Now the Hamiltonian is simpler, and can be solved either by mean field theory [109, 51, 22] or quantum approach [84, 110]. Moreover, it has been shown that spin-1 system requires SU(3) group to describe the system [56]. In this thesis, we introduce another approach to the dynamics of the system using the Heisenberg picture and make a comparison between a spin-1 system and the double well condensates.

2.1 Gross-Pitaevskii Equation

In 1900, Planck proposed an revolutionary idea that blackbody radiation was emitted by quantized vibrating resonators. The famous Bose statistics for photons were

original developed to derive Planck's law. According to Planck, the vibrational energy is discrete, quantized, and proportional to vibrational frequency $\epsilon = h\nu$ [111]. The constant h was later called Planck's constant. The quantum energy of radiation emitted is called a photon. Planck's work triggered the eventual emergence of quantum mechanics from whereby. Physical objects can be described at the microscopic level using wave function representations. With new tools from quantum physics, Bose-Einstein condensate can be studied deeper into the internal states.

Originally, a BEC was proposed in the context of a non-interacting gas. However, the interactions of gas particles through elastic two-body collisions play a necessary role for atoms to reach thermal equilibrium in the cooling process, in the characterization of the ground state [112, 113], and in spinor dynamics [50, 51, 52, 53, 54, 55]. The Hamiltonian of the condensate includes the kinetic energy, the potential energy of the confined trap V_T, and the two-body interaction energy,

$$H = \sum_{i=1}^{N} \left(-\frac{\nabla^2}{2m} + V_T(\mathbf{r}_i) \right) + \sum_{i<j} g\delta(\mathbf{r}_i - \mathbf{r}_j) \tag{2.1}$$

Eqn 2.1 is called the Gross-Pitaevskii equation (or nonlinear Schrödinger equation) [103, 104], and $U(\mathbf{r}_i - \mathbf{r}_j) = \sum_{i<j} g\delta(\mathbf{r}_i - \mathbf{r}_j)$ is the two-body interaction. During the two-body collision, the total spin is the sum of individual spin, $\vec{F} = \vec{f_1} + \vec{f_2}$. Because the wave functions of bosons are symmetric, the total spin during the collision must be an even number. For spin-1 system, possible spin numbers are $F = 0, 2$. For a typical BEC trap, the frequency of the trap is many orders of magnitude smaller than the transition frequency between hyperfine levels. Therefore, two body collisions will not change the hyperfine state of an individual atom [84]. An atomic BEC has low enough energy to preclude collisions with higher order angular momentum configurations $(p, d, f, g...)$ which require overcoming the long-range van der Waals potential barrier [114]. Therefore, the scattering length of BEC is dominated by s-wave scattering at low energy. The s-wave dominance can also be obtained from the scattering cross

section [103, p.109]:

$$\sigma = \frac{4\pi}{k^2}\sum_{l=0}^{\infty}(2l+1)\sin^2(\delta_l)$$

Here, k is the wave number, δ_l is the phase shift of incoming and outgoing wave, and l is angular momentum number of Legendre polynomials. For $k \to 0$, the dominate term is $\delta_{l=0}$ or s-wave scattering [103, p.109]. The two-body collision term therefore can be rewritten as [105, 84, 106],

$$U(\mathbf{r}_i - \mathbf{r}_j) = \delta(\mathbf{r}_i - \mathbf{r}_j)\sum_{F=0}^{2} g_F \sum_{m_F=-F}^{F} |F, m_F\rangle\langle F, M_F|$$

The constant $g_F = \frac{4\pi\hbar^2 a_F}{m}$ is the two-body mean-field coupling strength and proportional to s-wave scattering length of two bosons a_F. In the basis of individual atom's hyperfine quantum number $|f_1, m_{f1}; f_2, m_{f2}\rangle$, one can write

$$|F, m_F\rangle = \sum_{m_{f1}=-f_1}^{f_1}\sum_{m_{f2}=-f_2}^{f_2} |f_1, m_{f1}; f_2, m_{f2}\rangle\langle f_1, m_{f1}; f_2, m_{f2}|F, m_F\rangle$$

Where $\langle f_1, m_{f1}; f_2, m_{f2}|F, m_F\rangle$ is a Clebsch-Gordon coefficient. In the case of a spin-1 system $f_1 = f_2 = 1$, the two-body interaction operator can be written as [105, 84]

$$\begin{aligned}
&\sum_{F=0}^{2} g_F \sum_{m_F=-F}^{F} |F, m_F\rangle\langle F, m_F| \\
&= g_0\left(\frac{4}{3}\hat{\psi}_1^\dagger\hat{\psi}_{-1}^\dagger\hat{\psi}_1\hat{\psi}_{-1} + \frac{1}{3}\hat{\psi}_0^\dagger\hat{\psi}_0^\dagger\hat{\psi}_0\hat{\psi}_0 - \frac{2}{3}\hat{\psi}_1^\dagger\hat{\psi}_{-1}^\dagger\hat{\psi}_0\hat{\psi}_0 - \frac{2}{3}\hat{\psi}_0^\dagger\hat{\psi}_0^\dagger\hat{\psi}_1\hat{\psi}_{-1}\right) \\
&\quad + g_2\left(\hat{\psi}_1^\dagger\hat{\psi}_1^\dagger\hat{\psi}_1\hat{\psi}_1 + 2\hat{\psi}_1^\dagger\hat{\psi}_0^\dagger\hat{\psi}_1\hat{\psi}_0 + \frac{2}{3}\hat{\psi}_1^\dagger\hat{\psi}_{-1}^\dagger\hat{\psi}_1\hat{\psi}_{-1} + \frac{2}{3}\hat{\psi}_0^\dagger\hat{\psi}_0^\dagger\hat{\psi}_0\hat{\psi}_0\right. \\
&\quad \left. + \frac{2}{3}\hat{\psi}_1^\dagger\hat{\psi}_{-1}^\dagger\hat{\psi}_0\hat{\psi}_0 + \frac{2}{3}\hat{\psi}_0^\dagger\hat{\psi}_0^\dagger\hat{\psi}_1\hat{\psi}_{-1} + 2\hat{\psi}_0^\dagger\hat{\psi}_{-1}^\dagger\hat{\psi}_0\hat{\psi}_{-1} + \hat{\psi}_{-1}^\dagger\hat{\psi}_{-1}^\dagger\hat{\psi}_{-1}\hat{\psi}_{-1}\right)
\end{aligned}$$

where the shorthand notation for field operator $\hat{\psi}_a^\dagger \to |f = 1, m_f = a\rangle$

The second quantized Hamiltonian of the system can be decomposed into the spin-independent symmetric and the spin-dependent asymmetric Hamiltonian [105, 84].

$$\mathcal{H}_S = \sum_i \int d^3r \hat{\psi}_i^\dagger \left(-\frac{\nabla^2}{2m} + V_T\right) \hat{\psi}_i + \frac{\lambda_s}{2} \sum_{i,j} \int d^3r \hat{\psi}_i^\dagger \hat{\psi}_j^\dagger \hat{\psi}_i \hat{\psi}_j \tag{2.2}$$

$$\begin{aligned}\mathcal{H}_A = \frac{\lambda_a}{2} \int d^3r \Big(&\hat{\psi}_1^\dagger \hat{\psi}_1^\dagger \hat{\psi}_1 \hat{\psi}_1 + \hat{\psi}_{-1}^\dagger \hat{\psi}_{-1}^\dagger \hat{\psi}_{-1} \hat{\psi}_{-1} + 2\hat{\psi}_1^\dagger \hat{\psi}_0^\dagger \hat{\psi}_1 \hat{\psi}_0 \\ &+2\hat{\psi}_{-1}^\dagger \hat{\psi}_0^\dagger \hat{\psi}_{-1} \hat{\psi}_0 - 2\hat{\psi}_1^\dagger \hat{\psi}_{-1}^\dagger \hat{\psi}_1 \hat{\psi}_{-1} + 2\hat{\psi}_0^\dagger \hat{\psi}_0^\dagger \hat{\psi}_1 \hat{\psi}_{-1} + 2\hat{\psi}_1^\dagger \hat{\psi}_{-1}^\dagger \hat{\psi}_0 \hat{\psi}_0\Big)\end{aligned} \tag{2.3}$$

where $\lambda_s = \frac{2g_2+g_0}{3}$, $\lambda_a = \frac{g_2-g_0}{3}$, and $i = 0, \pm 1$.

The symmetric Hamiltonian $\mathcal{H}_S$ does not change the spin components of the system. The asymmetry Hamiltonian changes the spin components of the system.

2.2 Single Mode Approximation

The full Hamiltonian of the BEC includes the symmetric Hamiltonian $\mathcal{H}_S$ of Eqn 2.2 and the asymmetric Hamiltonian $\mathcal{H}_A$ of Eqn 2.3. The symmetric part of the Hamiltonian, which includes the kinetic energy and the external potential, creates the spatial structure and spatial energy of the condensate. In order to see the full extent, we have to consider the coupling of spinor and spatial structure in the wave functions. When the size of the condensate is smaller than the spin healing length $\xi_s = h/\sqrt{2m|\lambda_a|n}$, where n is number density, the spin components have the same spatial wave function [84, 107, 105] which leads to the single mode approximation (SMA),

$$\hat{\psi}_i \approx \hat{a}_i \phi(\mathbf{r})$$

here, $\hat{a}_i = |1, i\rangle$ is the annihilation operator of the spin state of the wave function, which obeys the bosonic commutation relation $[a_k, a_l] = 0$ and $\left[a_k, a_l^\dagger\right] = \delta_{kl}$. For ^{87}Rb and ^{23}Na, $\lambda_s \gg |\lambda_a|$ [105], the symmetric Hamiltonian is the dominant term and determines the partial wave function $\phi(\mathbf{r})$. In the SMA, $\phi(\mathbf{r})$ is the spatial wave function of the condensate, which satisfie the Gross-Pitaevskii equation [84]

$$\left(-\frac{\nabla^2}{2m} + V_T + \lambda_s N|\phi|^2\right)\phi = \mu\phi \tag{2.4}$$

here, μ is the chemical potential of the condensate. Substituting into Eqn 2.2 and 2.3 yields

$$\begin{aligned}
\mathcal{H}_S &= \sum_i \int d^3r \hat{\psi}_i^\dagger \left(\mu - \lambda_s N|\phi|^2\right) \hat{\psi}_i + \frac{\lambda_s}{2} \sum_{,j} \int d^3r \hat{\psi}_i^\dagger \hat{\psi}_j^\dagger \hat{\psi}_i \hat{\psi}_j \\
&= \sum_i \hat{a}_i^\dagger \left(\mu - 2\lambda_s' N\right) \hat{a}_i + \sum_{i,j} \hat{a}_i^\dagger \hat{a}_j^\dagger \hat{a}_i \hat{a}_j \\
&= \mu \hat{N} - \lambda_s' \hat{N}(\hat{N}+1) \qquad (2.5) \\
\mathcal{H}_A &= \lambda_a' \Big(\hat{a}_1^\dagger \hat{a}_1^\dagger \hat{a}_1 \hat{a}_1 + \hat{a}_{-1}^\dagger \hat{a}_{-1}^\dagger \hat{a}_{-1} \hat{a}_{-1} + 2\hat{a}_1^\dagger \hat{a}_0^\dagger \hat{a}_1 \hat{a}_0 \\
&\quad + 2\hat{a}_{-1}^\dagger \hat{a}_0^\dagger \hat{a}_{-1} \hat{a}_0 - 2\hat{a}_1^\dagger \hat{a}_{-1}^\dagger \hat{a}_1 \hat{a}_{-1} + 2\hat{a}_0^\dagger \hat{a}_0^\dagger \hat{a}_1 \hat{a}_{-1} + 2\hat{a}_1^\dagger \hat{a}_{-1}^\dagger \hat{a}_0 \hat{a}_0 \Big) \qquad (2.6)
\end{aligned}$$

where $\lambda_k' = \frac{\lambda_k}{2} \int d^3r |\phi|^4$. The symmetric Hamiltonian Eqn 2.5 is a constant thus does not affect to the spinor dynamics of the system, which are governed by Eqn 2.6.

2.3 Mathematical Background

As discussed in the Section 2.2, the wave function can be decomposed into three internal spinor modes of $\hat{a}_1$, $\hat{a}_0$, $\hat{a}_{-1}$ with the same overall spatial wave function. Any Hermitian operator can be written as a linear combination of $\hat{a}_i^\dagger \hat{a}_k$ for $i, k = 0, \pm 1$, we thus have a total of 9 operators. The completeness relation $\frac{1}{N} \sum_i \hat{a}_i^\dagger \hat{a}_i = \hat{1}$ reduces the number of linearly independent operators to 8. Using a SU(3) group to describe the spinor-1 BEC was discussed by different groups [84, 83, 115] and summarized in Refs. [56, 64]. In the quantum approach, the operators are represented by second quantization operators [56], while in the mean field approach, the operators are represented by 3×3 matrices [116, 115]. In this section, we will derive the spin-1 operators in the quantum and mean field representations.

Let z be the quantization axis of the system. The spin operator S_z will have three possible eigenvalues of $0, \pm 1$ corresponding to three eigenstates $|f = 1, m_f = 0, \pm 1\rangle$. For the eigenstate $|f = 1, m_f = 1\rangle$, all the atoms are in the $m_f = 1$ state and similarly for $|f = 1, m_f = 0\rangle$, and $|f = 1, m_f = -1\rangle$. In the mean field regime, the

wave function can be represented by a vector of three complex numbers,

$$|1,1\rangle = (1,0,0)^T; \quad |1,0\rangle = (0,1,0)^T; \quad |1,-1\rangle = (0,0,1)^T$$

Using the eigenvalues and eigenstates of the spin operator, we have

$$\hat{S}_z|1,1\rangle = 1|1,1\rangle; \quad \hat{S}_z|1,0\rangle = 0|1,0\rangle; \quad \hat{S}_z|1,-1\rangle = -1|1,-1\rangle$$

hence

$$\begin{aligned} \hat{S}_z|1,1\rangle\langle 1,1| &= 1|1,1\rangle\langle 1,1| \\ \hat{S}_z|1,0\rangle\langle 1,0| &= 0|1,0\rangle\langle 1,0| \\ \hat{S}_z|1,-1\rangle\langle 1,-1| &= -1|1,-1\rangle\langle 1,-1| \end{aligned}$$

Applying the completeness condition $\sum_i |i\rangle\langle i| = \hat{1}$, the spin operator S_z can be written as

$$S_z = |1,1\rangle\langle 1,1| - |1,-1\rangle\langle 1,-1|$$

The corresponding second quantization spin operator can be written as

$$\hat{S}_z = \hat{a}_1^\dagger \hat{a}_1 - \hat{a}_{-1}^\dagger \hat{a}_{-1}$$

In the matrix representation, the spin operator can be written as

$$S_z = (1,0,0)^T \cdot (1,0,0) - (0,0,1)^T \cdot (0,0,1) = \begin{pmatrix} 1 & 0 & 0 \\ 0 & 0 & 0 \\ 0 & 0 & -1 \end{pmatrix}$$

We can construct a raising and lowering spin operator using the relations

$$\hat{S}_\pm|f,m_f\rangle = \sqrt{f(f+1) - m_f(m_f \pm 1)}|f,m_f \pm 1\rangle \tag{2.7}$$

The other Cartesian spin operators $\hat{S}_x, \hat{S}_y$ can be derived by the relations

$$\hat{S}_+ = \hat{S}_x + i\hat{S}_y \qquad \hat{S}_- = \hat{S}_x - i\hat{S}_y \tag{2.8}$$

From Eqn 2.7 and 2.8, we obtain the spin operators in matrix forms

$$S_+ = \sqrt{2}\begin{pmatrix} 0 & 1 & 0 \\ 0 & 0 & 1 \\ 0 & 0 & 0 \end{pmatrix} \quad , \quad S_- = \sqrt{2}\begin{pmatrix} 0 & 0 & 0 \\ 1 & 0 & 0 \\ 0 & 1 & 0 \end{pmatrix}$$

$$S_x = \frac{1}{\sqrt{2}}\begin{pmatrix} 0 & 1 & 0 \\ 1 & 0 & 1 \\ 0 & 1 & 0 \end{pmatrix} \quad , \quad S_y = \frac{i}{\sqrt{2}}\begin{pmatrix} 0 & -1 & 0 \\ 1 & 0 & -1 \\ 0 & 1 & 0 \end{pmatrix}$$

and in second quantization operator forms [56, 64]

$$\begin{aligned} \hat{S}_+ &= \sqrt{2}(\hat{a}_1^\dagger \hat{a}_0 + \hat{a}_0^\dagger \hat{a}_{-1}) \\ \hat{S}_- &= \sqrt{2}(\hat{a}_0^\dagger \hat{a}_1 + \hat{a}_{-1}^\dagger \hat{a}_0) \\ \hat{S}_x &= \frac{1}{\sqrt{2}}\left(\hat{a}_1^\dagger \hat{a}_0 + \hat{a}_0^\dagger \hat{a}_{-1} + \hat{a}_0^\dagger \hat{a}_1 + \hat{a}_{-1}^\dagger \hat{a}_0\right) \\ \hat{S}_y &= \frac{1}{\sqrt{2}}\left(-\hat{a}_1^\dagger \hat{a}_0 - \hat{a}_0^\dagger \hat{a}_{-1} + \hat{a}_0^\dagger \hat{a}_1 + \hat{a}_{-1}^\dagger \hat{a}_0\right) \end{aligned}$$

The basis can be decomposed into dipole (spin operator) and quadrupole moments [116]. In matrix form, the quadrupole moments can be generated by the combination of two dipoles [115]

$$Q_{ij} = S_i S_j + S_j S_i - \frac{4}{3}\delta_{ij} \tag{2.9}$$

In second quantization form, the quadrupole moments are formulated as [56, 64]

$$\hat{Q}_{ij} = -\hat{c}_{ij} - \hat{c}_{ji} + \frac{2}{3}\delta_{ij}\hat{c}_{kk} \tag{2.10}$$

$$\hat{c}_{ij} = \hat{b}_i \hat{b}_j \qquad \hat{b}_x^\dagger = (-\hat{a}_1^\dagger + \hat{a}_{-1}^\dagger)/\sqrt{2} \qquad \hat{b}_y^\dagger = i(\hat{a}_1^\dagger + \hat{a}_{-1}^\dagger)/\sqrt{2} \qquad \hat{b}_z^\dagger = \hat{a}_0^\dagger$$

With the spin operators obtained previously, and using the formulas in Eqn 2.9 and 2.10, we can obtain a representation for quadrupole operators in matrices and second quantization form. The spin and quadrupole operators are shown in Table 2.1 and their commutators are shown in the Appendix Table B.1

Table 2.1: Operators of spin-1 system. Matrices are in the spherical polar basis $|f, m_f\rangle$. [64]

$S_x =$	$\frac{1}{\sqrt{2}}\begin{pmatrix} 0 & 1 & 0 \\ 1 & 0 & 1 \\ 0 & 1 & 0 \end{pmatrix}$	$\hat{S}_x = \frac{1}{\sqrt{2}}\left(\hat{a}_1^\dagger\hat{a}_0 + \hat{a}_0^\dagger\hat{a}_{-1} + \hat{a}_0^\dagger\hat{a}_1 + \hat{a}_{-1}^\dagger\hat{a}_0\right)$
$S_y =$	$\frac{\imath}{\sqrt{2}}\begin{pmatrix} 0 & -1 & 0 \\ 1 & 0 & -1 \\ 0 & 1 & 0 \end{pmatrix}$	$\hat{S}_y = \frac{\imath}{\sqrt{2}}\left(-\hat{a}_1^\dagger\hat{a}_0 - \hat{a}_0^\dagger\hat{a}_{-1} + \hat{a}_0^\dagger\hat{a}_1 + \hat{a}_{-1}^\dagger\hat{a}_0\right)$
$S_z =$	$\begin{pmatrix} 1 & 0 & 0 \\ 0 & 0 & 0 \\ 0 & 0 & -1 \end{pmatrix}$	$\hat{S}_z = \left(\hat{a}_1^\dagger\hat{a}_1 - \hat{a}_{-1}^\dagger\hat{a}_{-1}\right)$
$Q_{yz} =$	$\frac{\imath}{\sqrt{2}}\begin{pmatrix} 0 & -1 & 0 \\ 1 & 0 & 1 \\ 0 & -1 & 0 \end{pmatrix}$	$\hat{Q}_{yz} = \frac{\imath}{\sqrt{2}}\left(-\hat{a}_1^\dagger\hat{a}_0 + \hat{a}_0^\dagger\hat{a}_{-1} + \hat{a}_0^\dagger\hat{a}_1 - \hat{a}_{-1}^\dagger\hat{a}_0\right)$
$Q_{xz} =$	$\frac{1}{\sqrt{2}}\begin{pmatrix} 0 & 1 & 0 \\ 1 & 0 & -1 \\ 0 & -1 & 0 \end{pmatrix}$	$\hat{Q}_{xz} = \frac{1}{\sqrt{2}}\left(\hat{a}_1^\dagger\hat{a}_0 - \hat{a}_0^\dagger\hat{a}_{-1} + \hat{a}_0^\dagger\hat{a}_1 - \hat{a}_{-1}^\dagger\hat{a}_0\right)$
$Q_{xy} =$	$\imath\begin{pmatrix} 0 & 0 & -1 \\ 0 & 0 & 0 \\ 1 & 0 & 0 \end{pmatrix}$	$\hat{Q}_{xy} = \imath\left(-\hat{a}_1^\dagger\hat{a}_{-1} + \hat{a}_{-1}^\dagger\hat{a}_1\right)$
$Q_{xx} =$	$\begin{pmatrix} -\frac{1}{3} & 0 & 1 \\ 0 & \frac{2}{3} & 0 \\ 1 & 0 & -\frac{1}{3} \end{pmatrix}$	$\hat{Q}_{xx} = -\frac{1}{3}\hat{a}_{+1}^\dagger\hat{a}_{+1} + \frac{2}{3}\hat{a}_0^\dagger\hat{a}_0 - \frac{1}{3}\hat{a}_{-1}^\dagger a_{-1} + \hat{a}_{+1}^\dagger\hat{a}_{-1} + \hat{a}_{-1}^\dagger\hat{a}_{+1}$
$Q_{yy} =$	$\begin{pmatrix} -\frac{1}{3} & 0 & -1 \\ 0 & \frac{2}{3} & 0 \\ -1 & 0 & -\frac{1}{3} \end{pmatrix}$	$\hat{Q}_{yy} = -\frac{1}{3}\hat{a}_{+1}^\dagger\hat{a}_{+1} + \frac{2}{3}\hat{a}_0^\dagger\hat{a}_0 - \frac{1}{3}\hat{a}_{-1}^\dagger\hat{a}_{-1} - \hat{a}_{+1}^\dagger\hat{a}_{-1} - \hat{a}_{-1}^\dagger\hat{a}_{+1}$
$Q_{zz} =$	$\begin{pmatrix} \frac{2}{3} & 0 & 0 \\ 0 & -\frac{4}{3} & 0 \\ 0 & 0 & \frac{2}{3} \end{pmatrix}$	$\hat{Q}_{zz} = \frac{2}{3}\hat{a}_{+1}^\dagger\hat{a}_{+1} - \frac{4}{3}\hat{a}_0^\dagger\hat{a}_0 + \frac{2}{3}\hat{a}_{-1}^\dagger\hat{a}_{-1}$

2.4 Quantum Approach

Using second quantization operators, we can rewrite the asymmetric Hamiltonian part of Eqn 2.6 in a simple form [84, 106, 56]

$$\mathcal{H}_a = \lambda_a'(\hat{S}^2 - 2\hat{N}) \tag{2.11}$$

The magnetic field introduces energy shifts to the Zeeman sub-levels of the hyperfine state. The Zeeman energy for total atoms in each spinor state becomes [64]

$$\begin{aligned} E_{B1} &= pN_1 + qN_1 + N_1E_0 \\ E_{B0} &= N_0E_0 \\ E_{B-1} &= -pN_{-1} + qN_{-1} + N_1E_0 \end{aligned}$$

where $p = -\mu_B B_z g_f$ is the linear Zeeman effect, $q = \mu_B^2 B_z^2/(\hbar^2 E_{HFS})$ is the quadratic Zeeman effect, g_f is the Landé g-factor, μ_B is the Bohr magneton, and E_{HFS} is the ground state hyperfine splitting. The total magnetic field energy will then be

$$E_B = p(N_1 - N_{-1}) + q(N_1 + N_{-1}) + NE_0$$

The Hamiltonian of a spinor BEC in a finite magnetic field takes the form [110, 61]

$$\mathcal{H}_a = \lambda_a'(\hat{S}^2 - 2\hat{N}) + p(\hat{N}_1 - \hat{N}_{-1}) + q(\hat{N}_1 + \hat{N}_{-1}) + \hat{N}E_0$$

The last term $\hat{N}E_0$ is a constant; therefore in the Heisenberg picture, this will not evolve and will not affect the dynamics of the system. Note that $\hat{S}_z = \hat{N}_1 - \hat{N}_{-1}$. If we ignore the constant term, the quadratic Zeeman operator can be represented by the quadrupole moment

$$Q_{zz} = 2(\hat{N}_1 + \hat{N}_{-1}) - \frac{4}{3}\hat{N}$$

The Hamiltonian can thus take a simple form [84, 56]

$$\mathcal{H}_a = \lambda_a'(\hat{S}^2 - 2\hat{N}) + p\hat{S}_z + \frac{q}{2}\hat{Q}_{zz} \tag{2.12}$$

Since $\hat{Q}_{zz}$ and $\hat{S}^2$ do not commute [64], it is non-trivial to find the common eigenstate basis for all the operators. However, the Hamiltonian Eqn 2.6 has eigenstates in the Fock states $|N_{-1}, N_0, N_1\rangle$ or the equivalent representation $|N, M, k\rangle$ where N is the total number of atoms, M is the magnetization, and k is the number of pairs of atoms in the $m_f = \pm 1$ state. Moreover, the Hamiltonian conserves the total number

of atoms $N = N_{-1} + N_0 + N_1$ and the magnetization $M = N_1 - N_{-1}$; these two constraints simplify the Fock state to a single parameter k. The Fock states basis of the Hamiltonian has dimensions of $N/2+1$ and can be represented in the vector form

$$|k\rangle = (0, 0, .., k^{th} = 1, .., 0)^T \qquad k \in [0, \frac{N}{2}]$$

The Hamiltonian in Eqn 2.12 can be written as [84, 110]

$$\begin{aligned}\mathcal{H}_a &= \lambda_a' \Big((\hat{N}_1 - \hat{N}_{-1})^2 + (2\hat{N}_0 - 1)(\hat{N}_1 + \hat{N}_{-1}) + 2\hat{a}_1^\dagger \hat{a}_{-1}^\dagger \hat{a}_0 \hat{a}_0 + 2\hat{a}_0^\dagger \hat{a}_0^\dagger \hat{a}_1 \hat{a}_{-1} \Big) \\ &\quad + p(\hat{N}_1 - \hat{N}_{-1}) + q(\hat{N}_1 + \hat{N}_{-1}) + \hat{N} E_0\end{aligned}$$

For an initial state where all atoms are in the state $|f, m_f = 0\rangle$, the conservation of magnetization reads that $M = N_1 - N_{-1} = 0$. The matrix element of the Hamiltonian will take the form [110, 56]

$$\begin{aligned}\mathcal{H}_{k,k'} &= (2\lambda_a' k(2(N-2k)-1) + 2qk)\, \delta_{k,k'+1} \\ &\quad + 2\lambda_a' \Big((k'+1)\sqrt{(N-2k')(N-2k'-1)}\delta_{k,k'+1} \\ &\quad + k\sqrt{(N-2k'+1)(N-2k'+2)}\delta_{k,k'-1} \Big) \end{aligned} \tag{2.13}$$

The exact Hamiltonian of the system in Eqn 2.13 (within SMA) is a symmetric tridiagonal matrix. The dynamics of the system can be calculated by numerical integration of the Schrödinger equations, $i\hbar\frac{\partial}{\partial t}\psi = \hat{\mathcal{H}}\psi$. Even though the symmetric tridiagonal characteristic of the matrix reduces the number of computational operators, this is still an intensive computation. The details of the computational method are described in Appendix A.

2.5 Mean Field Approach

In the quantum approach, there are $N/2 + 1$ eigenstates for a system of N particles. The mathematical abstraction of the quantum approach is beautiful; however, finding an analytical solution is computationally intensive. For a typical condensate of $40,000$ atoms, $20,001$ parameters are required to describe the condensate. Using mean field

theory for a system of identical particles with a reasonable large number of atoms, the interaction between all particles can be described by an order parameter or a macroscopic wave function determined by the average inter-particle interaction. For a spin-1 Bose-Einstein condensates, all atoms have the same internal spinor wave function given by the number of atoms in the spin projection and the definite phase: $\hat{a}_i = \sqrt{N}|\zeta_i|e^{i\theta_i}$ for $|\zeta_i|^2 = \rho_i = N_i/N$ [106]. This reduces the number of parameters from $N/2+1$ to a few parameters ρ_i, θ_i for $i = 0, \pm 1$. In this section, we revisit the dynamics using the Schrödinger picture and introduce the Heisenberg picture into the spinor system. We also make a direct comparison between the spin-1 system and the double-well condensate system.

2.5.1 Schrödinger Picture

The single mode approximation decouples the spatial wave function from the internal spinor state. The spatial part of the wave function is governed by the symmetric Hamiltonian part. The asymmetric Hamiltonian governs the spinor dynamics of the condensate. The spinor dynamics of the condensate can be derived using the Heisenberg equation of motion

$$i\hbar\frac{\partial\hat{\psi}_i}{\partial t} = \left[\hat{\psi}_i, \mathcal{H}\right] \qquad i = 0, \pm 1 \tag{2.14}$$

The equation of motion of the field operators in the Heisenberg picture can be represented as a system of 3 coupled equations [105, 106, 108] by substituting Eqn 2.2 and Eqn 2.3 into Eqn 2.14, and applying the bosonic commutation relations

[105, 84, 109]

$$
\begin{aligned}
i\hbar\frac{\partial\hat{\psi}_1}{\partial t} &= \left(-\frac{\nabla^2}{2m}+V_T\right)\hat{\psi}_1+\lambda_s'\hat{\psi}_i^\dagger\hat{\psi}_i\hat{\psi}_1 \\
&\quad +2\lambda_a'\left(\hat{\psi}_1^\dagger\hat{\psi}_1\hat{\psi}_1-\hat{\psi}_{-1}^\dagger\hat{\psi}_1\hat{\psi}_{-1}+\hat{\psi}_0^\dagger\hat{\psi}_1\hat{\psi}_0+\hat{\psi}_{-1}^\dagger\hat{\psi}_0\hat{\psi}_0\right) \\
i\hbar\frac{\partial\hat{\psi}_0}{\partial t} &= \left(-\frac{\nabla^2}{2m}+V_T\right)\hat{\psi}_0+\lambda_s'\hat{\psi}_i^\dagger\hat{\psi}_i\hat{\psi}_0 \\
&\quad +2\lambda_a'\left(\hat{\psi}_1^\dagger\hat{\psi}_1\hat{\psi}_0+\hat{\psi}_{-1}^\dagger\hat{\psi}_0\hat{\psi}_{-1}+2\hat{\psi}_0^\dagger\hat{\psi}_1\hat{\psi}_{-1}\right) \\
i\hbar\frac{\partial\hat{\psi}_{-1}}{\partial t} &= \left(-\frac{\nabla^2}{2m}+V_T\right)\hat{\psi}_{-1}+\lambda_s'\hat{\psi}_i^\dagger\hat{\psi}_i\hat{\psi}_{-1} \\
&\quad +2\lambda_a'\left(\hat{\psi}_{-1}^\dagger\hat{\psi}_{-1}\hat{\psi}_{-1}-\hat{\psi}_1^\dagger\hat{\psi}_1\hat{\psi}_{-1}+\hat{\psi}_0^\dagger\hat{\psi}_0\hat{\psi}_{-1}+\hat{\psi}_1^\dagger\hat{\psi}_0\hat{\psi}_0\right)
\end{aligned}
\tag{2.15}
$$

The time dependent field operator of the condensate can be written in the mean field using the single mode approximation as $\hat{\psi}_i \approx \phi(\mathbf{r})e^{-i\mu t/\hbar}\hat{a}_i = \sqrt{N}\phi(\mathbf{r})e^{-i\mu t/\hbar}|\zeta_i|e^{i\theta_i}$ [84]. Substituting back into Eqn 2.15 and using the relation in Eqn 2.4 we obtain the coupled Gross-Pitaevskii equations [109],

$$
\begin{aligned}
i\hbar\frac{\partial\zeta_1}{\partial t} &= c\left[(\rho_1-\rho_{-1}+\rho_0)\zeta_1+\zeta_{-1}^\dagger\zeta_0^2\right] \\
i\hbar\frac{\partial\zeta_0}{\partial t} &= c\left[(\rho_1+\rho_{-1})\zeta_0+2\zeta_0^\dagger\zeta_1\zeta_{-1}\right] \\
i\hbar\frac{\partial\zeta_{-1}}{\partial t} &= c\left[(\rho_{-1}-\rho_1+\rho_0)\zeta_{-1}+\zeta_1^\dagger\zeta_0^2\right]
\end{aligned}
\tag{2.16}
$$

where $c = 2\lambda_a' N$ is the spinor dynamical rate. The experiments occur at a finite magnetic field which shifts the Zeeman energy of the spin projections. The energies shift can be calculated from the Breit-Rabi formula [117]. The magnetic field shifts spinor energy of $m_f = 0, \pm 1$ by an amount of $E_{m_f} = -m_f p_Z B + q_Z B^2$. Here p_Z is the linear Zeeman effect, q_Z is the quadratic Zeeman effect, and B is the magnetic field. The symmetric Hamiltonian Eqn 2.2 then becomes [109]

$$
\mathcal{H}_S = \sum_i \int d^3r\hat{\psi}_i^\dagger\left(-\frac{\nabla^2}{2m}+V_T+E_i\right)\hat{\psi}_i+\frac{\lambda_s}{2}\sum_{i,j}\int d^3r\hat{\psi}_i^\dagger\hat{\psi}_j^\dagger\hat{\psi}_i\hat{\psi}_j
$$

The coupled Gross-Pitaevskii equations with the magnetic field thus becomes [109]

$$\begin{aligned} i\hbar\frac{\partial\zeta_1}{\partial t} &= E_1\zeta_1 + c\left[(\rho_1-\rho_{-1}+\rho_0)\zeta_1 + \zeta_{-1}^{\dagger}\zeta_0^2\right] \\ i\hbar\frac{\partial\zeta_0}{\partial t} &= E_0\zeta_0 + c\left[(\rho_1+\rho_{-1})\zeta_0 + 2\zeta_0^{\dagger}\zeta_1\zeta_{-1}\right] \\ i\hbar\frac{\partial\zeta_{-1}}{\partial t} &= E_{-1}\zeta_{-1} + c\left[(\rho_{-1}-\rho_1+\rho_0)\zeta_{-1} + \zeta_1^{\dagger}\zeta_0^2\right] \end{aligned} \tag{2.17}$$

The wave function of condensate can be represented by a vector of three complex numbers $\psi = (\zeta_1, \zeta_0, \zeta_{-1})^T$. The normalization condition reads $\sum_{i=1}^{3}\rho_i = \sum_{i=1}^{3}|\zeta_i|^2 = 1$, and the conservation of magnetization is $m = \rho_1 - \rho_{-1}$. Therefore the wave function becomes $\psi = (\sqrt{\frac{1-\rho_0+m}{2}}e^{i\chi_+}, \rho_0, \sqrt{\frac{1-\rho_0-m}{2}}e^{i\chi_-})^T$ [109, 51, 64]. This reduces the dynamical equations into a pair of equations in spinor phase space [109]

$$\begin{aligned} \dot{\rho}_0 &= \frac{2c}{\hbar}\rho_0\sqrt{(1-\rho_0)^2-m^2}\sin\theta_s \\ \dot{\theta}_s &= \frac{2c}{\hbar}\left[(1-2\rho_0) + \frac{(1-\rho_0)(1-2\rho_0)-m^2}{\sqrt{(1-\rho_0)^2-m^2}}\cos\theta_s\right] - \frac{2q}{\hbar} \end{aligned} \tag{2.18}$$

where $\chi_\pm = \theta_{\pm1} - \theta_0 = \frac{\theta_s \pm \theta_m}{2}$ is the phase of spin states, $\theta_s = \theta_{+1} + \theta_{-1} - 2\theta_0 = \chi_+ - \chi_-$ is the spinor phase, and $\theta_m = \theta_{+1} - \theta_{-1}$ is the magnetization phase.

2.5.1.1 Spinor Phase Space

The spinor population dynamics occurs in the spinor phase space $\theta_s\rho_0$. In the mean field, the spinor energy is given by [118, 109]

$$\mathcal{E} = \frac{c}{2}m^2 + c\rho_0\left[(1-\rho_0) + \sqrt{(1-\rho_0)^2-m^2}\cos\theta_s\right] + pm + q(1-\rho_0) \tag{2.19}$$

For zero magnetization $m = 0$, which is similar to our experimental condition, the spinor phase spaces for different magnetic fields are shown in Figure 2.1 (top row). When the quadratic Zeeman $q = q_Z B^2 = 0$, there are no positive energy contours, one separatrix energy contour, and the ground state has $\rho_0 = 0.5$ as shown in Figure 2.1 a. When $q > 0$, the separatrix separating negative and positive energy contour appears (Figure 2.1 b). When $q = 2|c|$, the critical phase transition value, the

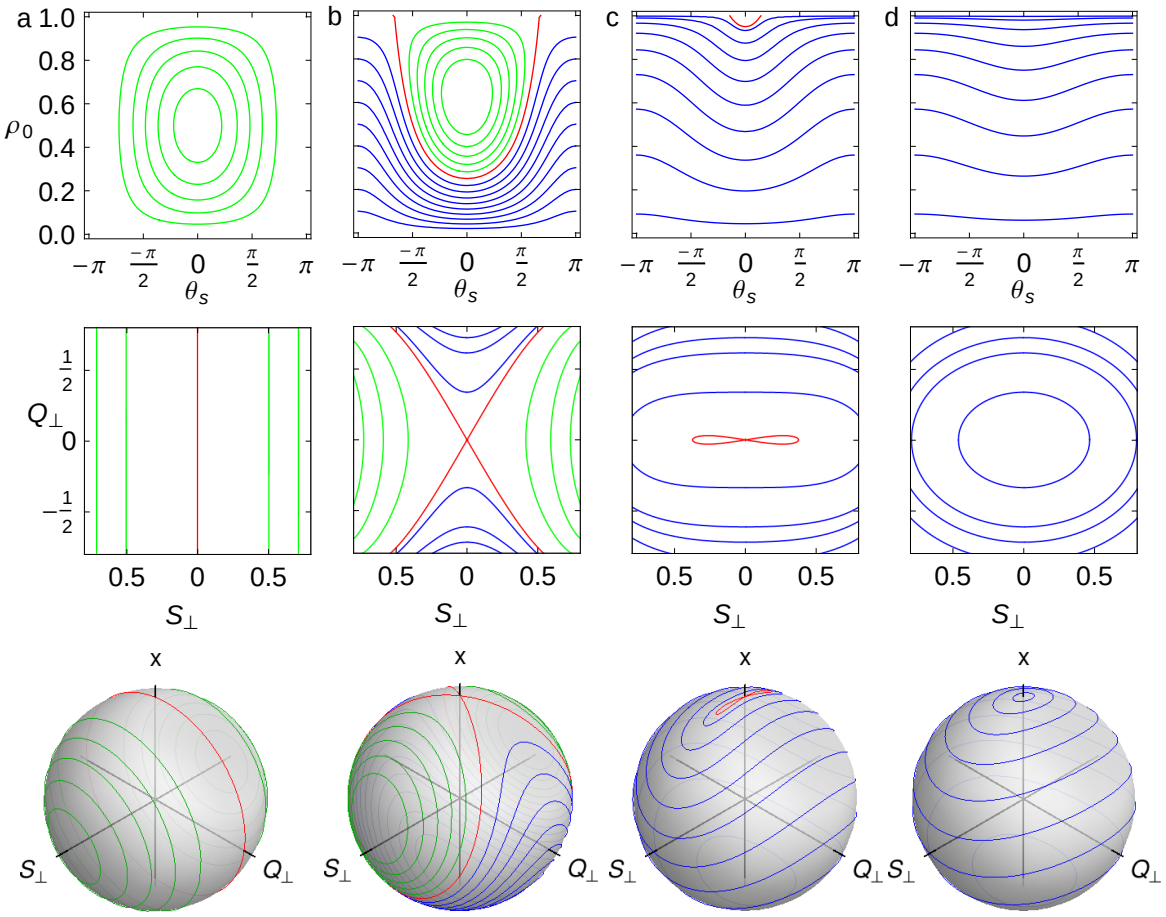

Figure 2.1: The spinor phase and spin-nematic sphere for different magnetic fields. Spinor energy contours in spinor phase space (top) and spin-nematic sphere (bottom) for $q = 0$, $q = 0.5|c|$, $q = 1.95|c|$, $q = 4|c|$ are shown in (a), (b), (c), and (d). The red curve represents the separatrix (zero energy contour). Negative energy contours (green) are inside the separatrix, and positive energy contours (blue) are outside. The separatrix starts to appear at $2|c|$.

separatrix disappears and the ground state becomes $\rho_0 = 1$ (2.1 c). When $q > 2|c|$, there are only positive energy contours (2.1 d). We will refer to the dynamics along the separatrix as spin mixing, and the dynamics inside or outside the separatrix as coherent oscillations.

2.5.1.2 Spin-Nematic Phase Space

The mean field expectation of the operators can be calculated from the matrix form (Table 2.1) and the wave function $\psi = (\sqrt{\frac{1-\rho_0+m}{2}}e^{i\chi_+}, \rho_0, \sqrt{\frac{1-\rho_0-m}{2}}e^{i\chi_-})^T$ for the case

of zero magnetization $m = 0$,

$$\begin{aligned}
S_x &= \langle\vec{\psi}|S_x|\vec{\psi}\rangle = 2\sqrt{\rho_0(1-\rho_0)}\cos\theta\cos\theta_L = S_\perp\cos\theta_L \\
Q_{yz} &= -2\sqrt{\rho_0(1-\rho_0)}\sin\theta\cos\theta_L = -Q_\perp\cos\theta_L \\
S_y &= -2\sqrt{\rho_0(1-\rho_0)}\cos\theta\sin\theta_L = -S_\perp\sin\theta_L \\
Q_{xz} &= -2\sqrt{\rho_0(1-\rho_0)}\sin\theta\sin\theta_L = -Q_\perp\sin\theta_L \\
Q_{0+}+Q_{0-} &= Q_{xx}-Q_{yy} = 2(1-\rho_0)\cos(2\theta_L) = 2Q_q\cos 2\theta_L \\
Q_{0+}-Q_{0-} &= 3Q_{zz} = 2-6\rho_0 = Q_0 \\
Q_{xy} &= (-1+\rho_0)\sin(2\theta_L) = -Q_q\sin 2\theta_L
\end{aligned}$$

Here $\theta = \theta_s/2$ is the quadrature angle, and $\theta_L = \theta_m/2$ is the Larmor phase. Defining $x = 2\rho_0 - 1$, $S_\perp^2 = S_x^2 + S_y^2$ and $Q_\perp^2 = Q_x^2 + Q_y^2$, we get the relation

$$S_\perp^2 + Q_\perp^2 + x^2 = 1 \tag{2.20}$$

From Eqn 2.20, we see that the mean field dynamics can be described in the Bloch sphere representation [119]. In order to observe squeezing, we need to consider the dynamics in the spin-nematic space $S_\perp Q_\perp$. The spin-nematic phase spaces and spheres for different quadratic Zeeman energies are shown in Figure 2.1 (second row and third row).

2.5.2 Heisenberg Picture

The Hamiltonian of the system in the single mode approximation is given in Eqn 2.12 [84, 56]

$$\mathcal{H} = \lambda\hat{S}^2 + p\hat{S}_z + \frac{q}{2}\hat{Q}_{zz}$$

where $\hat{S}^2 = \hat{S}_x^2 + \hat{S}_y^2 + \hat{S}_z^2$ and $\lambda = \lambda_a'$. In order to simplify dynamics we use the interaction picture to transform into a rotating frame synchronized with the Larmor

precession,

$$\begin{aligned}
\mathcal{H}_0 &= p\hat{S}_z \\
\mathcal{H}_I &= \hat{U}^\dagger \left(\lambda \hat{S}_\perp^2 + \lambda \hat{S}_z^2 + \frac{q}{2}\hat{Q}_{zz}\right)\hat{U} \\
&= \lambda \hat{S}_\perp^2 + \lambda \hat{S}_z^2 + \frac{q}{2}\hat{Q}_{zz}
\end{aligned} \tag{2.21}$$

where $\hat{U} = \exp(-\frac{\imath \hat{\mathcal{H}}_0 t}{\hbar}) = \exp(-\frac{\imath p \hat{S}_z t}{\hbar})$, and $\hat{S}_\perp^2 = \hat{S}_x^2 + \hat{S}_y^2$. We define operators in the rotating frame $\hat{\mathcal{A}} = \hat{U}^\dagger \hat{A} \hat{U}$ and using the Campbell-Hausdorff lemma, these operators are explicitly

$$\begin{aligned}
\hat{\mathcal{S}}_x &= \hat{S}_x \cos(\frac{pt}{\hbar}) - \hat{S}_y \sin(\frac{pt}{\hbar}) \\
\hat{\mathcal{S}}_y &= \hat{S}_x \sin(\frac{pt}{\hbar}) + \hat{S}_y \cos(\frac{pt}{\hbar}) \\
\hat{\mathcal{Q}}_{yz} &= \hat{Q}_{xz} \sin(\frac{pt}{\hbar}) + \hat{Q}_{yz} \cos(\frac{pt}{\hbar}) \\
\hat{\mathcal{Q}}_{xz} &= \hat{Q}_{xz} \cos(\frac{pt}{\hbar}) - \hat{Q}_{yz} \sin(\frac{pt}{\hbar}) \\
\hat{\mathcal{Q}}_{0+} &= \hat{\mathcal{Q}}_{zz} - \hat{\mathcal{Q}}_{yy} = \frac{1}{2}(\hat{Q}_{0+} - \hat{Q}_{0-}) \\
&\quad + \frac{1}{2}(\hat{Q}_{0+} + \hat{Q}_{0-}) \cos(\frac{2pt}{\hbar}) - \hat{Q}_{xy} \sin(\frac{2pt}{\hbar}) \\
\hat{\mathcal{Q}}_{0-} &= \hat{\mathcal{Q}}_{xx} - \hat{\mathcal{Q}}_{zz} = -\frac{1}{2}(\hat{Q}_{0+} - \hat{Q}_{0-}) \\
&\quad + \frac{1}{2}(\hat{Q}_{0+} + \hat{Q}_{0-}) \cos(\frac{2pt}{\hbar}) - \hat{Q}_{xy} \sin(\frac{2pt}{\hbar}) \\
\hat{\mathcal{Q}}_{xy} &= \hat{Q}_{xy} \cos(\frac{2pt}{\hbar}) + \frac{1}{2}(\hat{Q}_{0+} + \hat{Q}_{0-}) \sin(\frac{2pt}{\hbar})
\end{aligned}$$

The interaction picture does not change the commutator relations $\left[\hat{\mathcal{A}}, \hat{\mathcal{B}}\right] = \hat{U}^\dagger \left[\hat{A}, \hat{B}\right] \hat{U}$. The evolution dynamics of operator can be obtained from Heisenberg equation of motion, $\dot{\hat{\mathcal{A}}} = \frac{\imath}{\hbar}\left[\mathcal{H}_I, \hat{\mathcal{A}}\right]$

$$\begin{aligned}
\dot{\hat{\mathcal{S}}}_x &= -\frac{q}{\hbar}\hat{\mathcal{Q}}_{yz} \\
\dot{\hat{\mathcal{S}}}_y &= \frac{q}{\hbar}\hat{\mathcal{Q}}_{xz} \\
\dot{\hat{\mathcal{Q}}}_{yz} &= -\frac{\lambda}{\hbar}(\{\hat{\mathcal{Q}}_{0+}, \hat{\mathcal{S}}_x\} + \{\hat{\mathcal{Q}}_{xy}, \hat{\mathcal{S}}_y\} \\
&\quad - \{\hat{\mathcal{Q}}_{xz}, \hat{\mathcal{S}}_z\}) + \frac{q}{\hbar}\hat{\mathcal{S}}_x
\end{aligned}$$

$$
\begin{aligned}
\dot{\hat{\mathcal{Q}}}_{xz} &= -\frac{\lambda}{\hbar}(\{\hat{\mathcal{Q}}_{0-},\hat{\mathcal{S}}_y\}-\{\hat{\mathcal{Q}}_{xy},\hat{\mathcal{S}}_x\} \\
&\quad +\{\hat{\mathcal{Q}}_{yz},\hat{\mathcal{S}}_z\})-\frac{q}{\hbar}\hat{\mathcal{S}}_y \\
\dot{\hat{\mathcal{Q}}}_{0+} &= \frac{2\lambda}{\hbar}(2\{\hat{\mathcal{Q}}_{yz},\hat{\mathcal{S}}_x\}-\{\hat{\mathcal{Q}}_{xz},\hat{\mathcal{S}}_y\}-\{\hat{\mathcal{Q}}_{xy},\hat{\mathcal{S}}_z\}) \\
\dot{\hat{\mathcal{Q}}}_{0-} &= \frac{2\lambda}{\hbar}(2\{\hat{\mathcal{Q}}_{xz},\hat{\mathcal{S}}_y\}-\{\hat{\mathcal{Q}}_{yz},\hat{\mathcal{S}}_x\}-\{\hat{\mathcal{Q}}_{xy},\hat{\mathcal{S}}_z\}) \\
\dot{\hat{\mathcal{Q}}}_{xy} &= \frac{\lambda}{\hbar}(\{\hat{\mathcal{Q}}_{0+}+\hat{\mathcal{Q}}_{0-},\hat{\mathcal{S}}_z\}-\{\hat{\mathcal{Q}}_{xz},\hat{\mathcal{S}}_x\}+\{\hat{\mathcal{Q}}_{yz},\hat{\mathcal{S}}_y\})
\end{aligned}
\tag{2.22}
$$

Replacing the operators by the mean field expectation values, we have

$$
\begin{aligned}
\dot{\mathcal{S}}_x &= -\frac{q}{\hbar}\mathcal{Q}_{yz} \\
\dot{\mathcal{S}}_y &= \frac{q}{\hbar}\mathcal{Q}_{xz} \\
\dot{\mathcal{Q}}_{yz} &= -\frac{\lambda}{\hbar}(\{\mathcal{Q}_{0+},\mathcal{S}_x\}+\{\mathcal{Q}_{xy},\mathcal{S}_y\} \\
&\quad -\{\mathcal{Q}_{xz},\mathcal{S}_z\})+\frac{q}{\hbar}\mathcal{S}_x \\
\dot{\mathcal{Q}}_{xz} &= -\frac{\lambda}{\hbar}(\{\mathcal{Q}_{0-},\mathcal{S}_y\}-\{\mathcal{Q}_{xy},\mathcal{S}_x\} \\
&\quad +\{\mathcal{Q}_{yz},\mathcal{S}_z\})-\frac{q}{\hbar}\mathcal{S}_y \\
\dot{\mathcal{Q}}_{0+} &= \frac{2\lambda}{\hbar}(2\{\mathcal{Q}_{yz},\mathcal{S}_x\}-\{\mathcal{Q}_{xz},\mathcal{S}_y\}-\{\mathcal{Q}_{xy},\mathcal{S}_z\}) \\
\dot{\mathcal{Q}}_{0-} &= \frac{2\lambda}{\hbar}(2\{\mathcal{Q}_{xz},\mathcal{S}_y\}-\{\mathcal{Q}_{yz},\mathcal{S}_x\}-\{\mathcal{Q}_{xy},\mathcal{S}_z\}) \\
\dot{\mathcal{Q}}_{xy} &= \frac{\lambda}{\hbar}(\{\mathcal{Q}_{0+}+\mathcal{Q}_{0-},\mathcal{S}_z\}-\{\mathcal{Q}_{xz},\mathcal{S}_x\}+\{\mathcal{Q}_{yz},\mathcal{S}_y\})
\end{aligned}
\tag{2.23}
$$

Since the dynamics in $\{\hat{\mathcal{S}}_x,\ \hat{\mathcal{Q}}_{yz},\ \hat{\mathcal{Q}}_{0+}\}$ and $\{\hat{\mathcal{S}}_y,\ \hat{\mathcal{Q}}_{xz},\ \hat{\mathcal{Q}}_{0-}\}$ are degenerate, we can reduce the problem into a single space by using

$$
\mathcal{S}_\perp^2=\mathcal{S}_x^2+\mathcal{S}_y^2 \qquad \mathcal{Q}_\perp^2=\mathcal{Q}_{yz}^2+\mathcal{Q}_{xz}^2 \qquad \mathcal{Q}_q^2=\frac{1}{4}(\mathcal{Q}_{0+}+\mathcal{Q}_{0-})^2+\mathcal{Q}_{xy}^2
$$

Since $\mathcal{S}_\perp^2$ and $\mathcal{Q}_\perp^2$ synchronize to Larmor precession, we can define

$$\begin{aligned}
\mathcal{S}_x &= \mathcal{S}_\perp \cos(\theta_m/2)_{t=0} \\
\mathcal{S}_y &= -\mathcal{S}_\perp \sin(\theta_m/2)_{t=0} \\
\mathcal{Q}_{yz} &= -\mathcal{Q}_\perp \cos(\theta_m/2)_{t=0} \\
\mathcal{Q}_{xz} &= -\mathcal{Q}_\perp \sin(\theta_m/2)_{t=0} \\
\mathcal{Q}_{xy} &= -\mathcal{Q}_q \sin(2\theta_m/2)_{t=0} \\
\mathcal{Q}_{0+} + \mathcal{Q}_{0-} &= 2\mathcal{Q}_q \cos(2\theta_m/2)_{t=0} \\
\mathcal{Q}_{0+} - \mathcal{Q}_{0-} &= \mathcal{Q}_0
\end{aligned}$$

Substitute back into Eqn 2.23

$$\begin{aligned}
\dot{\hat{\mathcal{S}}}_\perp \cos(\theta_m/2) &= \frac{q}{\hbar}\mathcal{Q}_\perp \cos(\theta_m/2) \\
-\dot{\mathcal{S}}_\perp \sin(\theta_m/2) &= -\frac{q}{\hbar}\mathcal{Q}_\perp \sin(\theta_m/2) \\
-\dot{\mathcal{Q}}_\perp \cos(\theta_m/2) &= -\frac{2\lambda}{\hbar}(\mathcal{Q}_{0+}\mathcal{S}_\perp \cos(\theta_m/2) - \mathcal{Q}_{xy}\mathcal{S}_\perp \sin(\theta_m/2) \\
&\quad +\mathcal{Q}_\perp \mathcal{S}_z \sin(\theta_m/2)) + \frac{q}{\hbar}\mathcal{S}_\perp \cos(\theta_m/2) \\
-\dot{\mathcal{Q}}_\perp \sin(\theta_m/2) &= -\frac{2\lambda}{\hbar}(-\mathcal{Q}_{0-}\mathcal{S}_\perp \sin(\theta_m/2) - \mathcal{Q}_{xy}\mathcal{S}_\perp \cos(\theta_m/2) \\
&\quad -\mathcal{Q}_\perp \mathcal{S}_z \cos(\theta_m/2)) + \frac{q}{\hbar}\mathcal{S}_\perp \sin(\theta_m/2) \\
\dot{\mathcal{Q}}_{0+} &= \frac{4\lambda}{\hbar}(-2\mathcal{Q}_\perp \mathcal{S}_\perp \cos^2(\theta_m/2) - \mathcal{Q}_\perp \mathcal{S}_\perp \sin^2(\theta_m/2) - \mathcal{Q}_{xy}\mathcal{S}_z) \\
\dot{\mathcal{Q}}_{0-} &= \frac{4\lambda}{\hbar}(2\mathcal{Q}_\perp \mathcal{S}_\perp \sin^2(\theta_m/2) + \mathcal{Q}_\perp \mathcal{S}_\perp \cos^2(\theta_m/2) - \mathcal{Q}_{xy}\mathcal{S}_z) \\
-\dot{\mathcal{Q}}_q \sin(2\theta_m/2) &= \frac{\lambda}{\hbar}(\{\mathcal{Q}_{0+} + \mathcal{Q}_{0-}, \mathcal{S}_z\} + 2\mathcal{Q}_\perp \mathcal{S}_\perp \sin(\theta_m/2)\cos(\theta_m/2) \\
&\quad +2\mathcal{Q}_\perp \mathcal{S}_\perp \sin(\theta_m/2)\cos(\theta_m/2))
\end{aligned}$$

Thus the system can be reduced to the dynamics of $\mathcal{S}_\perp,\ \mathcal{Q}_\perp,\ \mathcal{Q}_q,\ \mathcal{Q}_0$. In the case of zero magnetization, $S_z = 0$ then we are left with a system of 4 operators.

$$\dot{\hat{\mathcal{S}}}_\perp = \frac{q}{\hbar}\mathcal{Q}_\perp$$

$$
\begin{aligned}
\dot{\mathcal{Q}}_\perp &= \frac{\lambda}{\hbar}(\mathcal{Q}_0\mathcal{S}_\perp + 2\mathcal{Q}_q\mathcal{S}_\perp) - \frac{q}{\hbar}\mathcal{S}_\perp \\
\dot{\mathcal{Q}}_0 &= -12\frac{\lambda}{\hbar}\mathcal{Q}_\perp\mathcal{S}_\perp \\
\dot{\mathcal{Q}}_q &= -2\frac{\lambda}{\hbar}\mathcal{Q}_\perp\mathcal{S}_\perp
\end{aligned}
$$

Defining expectation of operator $\mathcal{X} = -\frac{1}{4}(\mathcal{Q}_0 + 2\mathcal{Q}_q) = 2N_0 - N$, we are left with system of 3 equations

$$
\begin{aligned}
\dot{\mathcal{S}}_\perp &= \frac{q}{\hbar}\mathcal{Q}_\perp \\
\dot{\mathcal{Q}}_\perp &= -4\frac{\lambda}{\hbar}\mathcal{X}\mathcal{S}_\perp - \frac{q}{\hbar}\mathcal{S}_\perp \\
\dot{\mathcal{X}} &= 4\frac{\lambda}{\hbar}\mathcal{Q}_\perp\mathcal{S}_\perp
\end{aligned}
\tag{2.24}
$$

These dynamical equations of the spinor system are identical to the double-wells [120, 121] and pseudo spin-1/2 system [122].

2.5.3 Analogy to a Double-Well and Bosonic Josephson Junction

Bose-Einstein condensate in a double-well trap is commonly called a Bosonic Josephson junction (BJJ) [123, 124]. Comparing to double well, we can see the similarity in dynamics and discuss the Bose Josephson junction in a spinor condensate. The Hamiltonian of the BJJ in the second quantized form is given by [120, 121, 124]

$$
\begin{aligned}
\mathcal{H} &= \frac{\mathcal{E}_I}{8}(\hat{a}_1^\dagger\hat{a}_1 - \hat{a}_2^\dagger\hat{a}_2)^2 - \frac{\Delta\mu}{2}(\hat{a}_1^\dagger\hat{a}_1 - \hat{a}_2^\dagger\hat{a}_2) - \frac{\mathcal{E}_T}{2}(\hat{a}_1^\dagger\hat{a}_2 + \hat{a}_2^\dagger\hat{a}_1) \\
&= \frac{\mathcal{E}_I}{2}\hat{l}_z^2 - \Delta\mu\hat{l}_z - \mathcal{E}_T\hat{l}_x
\end{aligned}
$$

here $\mathcal{E}_I$ is the local two-body interaction coupling strength, $\mathcal{E}_T$ is the tunneling coupling strength between two condensate modes (tunneling), $\Delta\mu$ is the detuning, and $\hat{l}_i$ $(i = x, y, z)$ are defined as,

$$
\hat{l}_x = \frac{\hat{a}_1^\dagger\hat{a}_2 + \hat{a}_2^\dagger\hat{a}_1}{2} \qquad \hat{l}_y = \frac{\hat{a}_1^\dagger\hat{a}_2 - \hat{a}_2^\dagger\hat{a}_1}{2i} \qquad \hat{l}_z = \frac{\hat{a}_1^\dagger\hat{a}_1 - \hat{a}_2^\dagger\hat{a}_2}{2}
$$

where $\hat{a}_i^\dagger, \hat{a}_i$ are the creation/annihilation operators for the number of atoms in each well [121]. In the mean field regime, the equations 2.24 are exactly the same as the Bloch equations for the BJJ [120, 121, 122]. The mean-field Bloch equations for the BJJ are [120, 121]

$$\dot{s}_x = -\kappa s_z s_y \qquad \dot{s}_y = \mathcal{E}_T s_z + \kappa s_z s_x \qquad \dot{s}_z = -\mathcal{E}_T s_y$$

where $s_i = 2\langle l_i/N \rangle$, $\kappa = \frac{\mathcal{E}_I N}{2}$ for N is the total number of atoms. The mapping between the BJJ and the spin-1 dynamics based on Eqn 2.24 is

$$\begin{aligned} l_x &\leftrightarrow \mathcal{X}(\text{Fock}) \qquad l_y \leftrightarrow \mathcal{Q}_\perp \qquad l_z(\text{Fock}) \leftrightarrow \mathcal{S}_\perp \\ \mathcal{E}_T &\leftrightarrow q \qquad\qquad\qquad\qquad\qquad\quad \mathcal{E}_I \leftrightarrow \lambda \end{aligned}$$

In the BJJ, the Fock state basis is determined by $\hat{l}_z$, and in a spinor BEC, the Fock state basis is determined by the $\hat{\mathcal{X}}$ terms.

2.5.3.1 Bosonic Josephson Junction

To show the connection between the BEC and the BJJ [95], we describe the dynamics in an alternative phase space. To define the dynamics of the system, only two parameters are needed to define the Hamiltonian in the mean-field [125]

$$\mathcal{H}_{MF} = \frac{\Lambda}{2} z^2 - \sqrt{1 - z^2}\cos(\varphi)$$

where $z = \frac{N_2 - N_1}{N_2 + N_1}$ is the fractional imbalance, φ is the relative phase between two wells about the l_z axis, $\Lambda = \mathcal{E}_I N / 2\mathcal{E}_T$. This leads to equations of motion [125]

$$\begin{aligned} \dot{z}(t) &= -\sqrt{1 - z^2}\sin(\varphi) \\ \dot{\varphi}(t) &= \Lambda z(t) + \frac{z(t)}{\sqrt{1 - z(t)^2}}\cos\varphi(t) \end{aligned}$$

The Josephson current for the double well is $I = \dot{z}(t)$. The tunneling of atoms between double well results in an oscillation of the fractional population imbalance that has been referred as Bose-Josephson junction [120, 126, 121, 123]. Depending on

the order parameter $\Lambda = \mathcal{E}_I N/2\mathcal{E}_T$, the dynamics will be defined as Rabi, Josephson, or Fock regime [124]. Those regimes are defined explicitly based on the eigenstates [127].

• Rabi regime: $\mathcal{E}_I/2\mathcal{E}_T \ll N^{-2}$. The two-body interactions are negligible, and the tunneling between two well is strong. The number of atoms in each well is not well defined. The tunneling oscillation is compared to Rabi oscillation. There are two types of oscillations, π-oscillation on the pole where separatrix appears and plasma oscillation on another pole on the $l_x l_y l_z$ sphere.

• Josephson regime: $N^{-2} \ll \mathcal{E}_I/2\mathcal{E}_T \ll 1$. The two-body interactions and the tunneling between two well are comparable. The dynamics are highly non-linear.

• Fock regime: $1 \ll \mathcal{E}_I/2\mathcal{E}_T$. The two-body interactions dominate the Hamiltonian, and the tunneling between two well is negligible. The number of atoms in each well is well-defined.

To describe the spinor condensate in the language of Bose Josephson junction, we need to use $\mathcal{S}_\perp$ and its associated phase ϕ. However it is not convenient to describe the spinor dynamics in term of $\phi\mathcal{S}_\perp$. Instead, the spinor dynamics are often studied in the spinor phase space $\theta_s\rho_0$. Using the $\theta_s\rho_0$ spinor phase space, we can access the perpendicular axis to z axis of double well system. Therefore, we are able to observe the Bose Josephson junction from a different perspective. The spinor dynamics equation read [109, 51],

$$\begin{aligned}
\dot{\rho}_0 &= \frac{2c}{\hbar}\rho_0\sqrt{(1-\rho_0)^2 - m^2}\sin\theta_s \\
\dot{\theta}_s &= \frac{2c}{\hbar}\left[(1-2\rho_0) + \frac{(1-\rho_0)(1-2\rho_0) - m^2}{\sqrt{(1-\rho_0)^2 - m^2}}\cos\theta_s\right] - \frac{2q}{\hbar}
\end{aligned}$$

In fact, the ratio $q/|c|$ is treated as the order parameter $\Lambda = \mathcal{E}_I N/2\mathcal{E}_T$ of double well system in order to determine the Rabi, Josephson, and Fock regimes for the spinor system.

CHAPTER 3

EXPERIMENTAL APPARATUS

The current experimental apparatus was first assembled in 2007; however, a portion of the apparatus dates back to the original BEC apparatus built in 2001. Several generations of graduate students have worked on expanding and improving the apparatus as described in previous theses [128, 22, 129, 64, 130]. Here, I provide enough information in order for the reader to have a general idea about the experiment conducted in this thesis.

This work focuses on Bose-Einstein condensation in ^{87}Rb gases. Therefore, this experiment is designed to do three things: create a condensate, manipulate it, and measure it.

3.1 Creating a BEC

We create Bose-Einstein condensates by using the combination of a magneto-optical trap and a CO_2 laser optical dipole force trap as shown in Figure 3.3. The magneto optical trap (MOT) cools and traps rubidium gases inside a vacuum chamber ($10^{-10} \sim 10^{-11}$ torr). The MOT uses three pairs of retro-reflected cycling transition laser beams and two magnetic coils in a anti-Helmholtz configuration [131]. The typical trap depth of a MOT is in the mK regime and hence only captures atoms from the very low velocity tail of the Boltzmann distribution [22]. After initial loading, atoms are loaded into the CO_2 laser optical dipole trap with a trap depth of $\sim$100 μK. To achieve the temperature regime for BEC, we employ evaporative cooling that involves reducing the CO_2 laser beam waist and ramping down the power of CO_2 laser beam. Decreasing the power of the CO_2 laser allows hot atoms to escape from the trap; reducing the beam waist increases the density and hence collision rate between

atoms. The Bose-Einstein condensate is formed at the focus of the optical dipole trap. We now discuss the details of each component used to create a BEC.

3.1.1 Rubidium Atom ^{87}Rb

Early BEC experiments demonstrated that that alkali gases are one of the best candidates for studying cold atoms [4, 5, 6]. Our lab created the first all optical BEC of ^{87}Rb gas in 2001 [7]. To produce ^{87}Rb atoms, we run a current of $3 \sim 4$ A through a rubidium getter made of stainless steel. In addition, the blue uv lights kick out the atoms stuck on the chamber window; it helps to enrich the rubidium source in the chamber.

Rubidium has an atomic number of 37. Naturally rubidium mixture composes of two isotopes ^{85}Rb (72.2%) and ^{87}Rb (27.8%) [135]. For ^{87}Rb, the ground state electron configuration is $[\mathrm{Kr}]\,5\mathrm{s}^1$ or $5\,^2\mathrm{S}_{1/2}$. Recall that the conventional atomic symbol has the form $^{2S+1}L_J$ where J is the total angular momentum, S is electron spin, and L is the electron orbital angular momentum. Promoting the valence electron from $L = 0$ to $L = 1$ (S shell to P shell) results in two possible excited states $5\,^2P_{1/2}$ and $5\,^2P_{3/2}$. The optical transition from the ground state to these excited states are known as the D_1 and D_2 lines. The D_2 line is used as the cycling transition for laser cooling. The hyperfine atomic spin for the ground state is $\vec{f} = \vec{I} + \vec{J}$ where the nuclear spin $\vec{I} = \frac{3}{2}$ and total angular momentum $\vec{J} = \vec{S} + \vec{L} = \vec{S} + 0 = \frac{1}{2}$. The hyperfine ground states of ^{87}Rb thus have doublet ground states,

$$f_{lower} = \frac{3}{2} - \frac{1}{2} = 1 \qquad \text{and} \qquad f_{upper} = \frac{3}{2} + \frac{1}{2} = 2$$

Zeeman sublevels In the presence of a magnetic field, the hyperfine structure atomic spin f will induce $2f + 1$ Zeeman sublevels due to the projection of the atomic spin on the magnetic quantization axis. These Zeeman sublevels are $m_f = -f, -f+1, ..., f$. For zero magnetic field, these Zeeman sublevels are degenerate. For

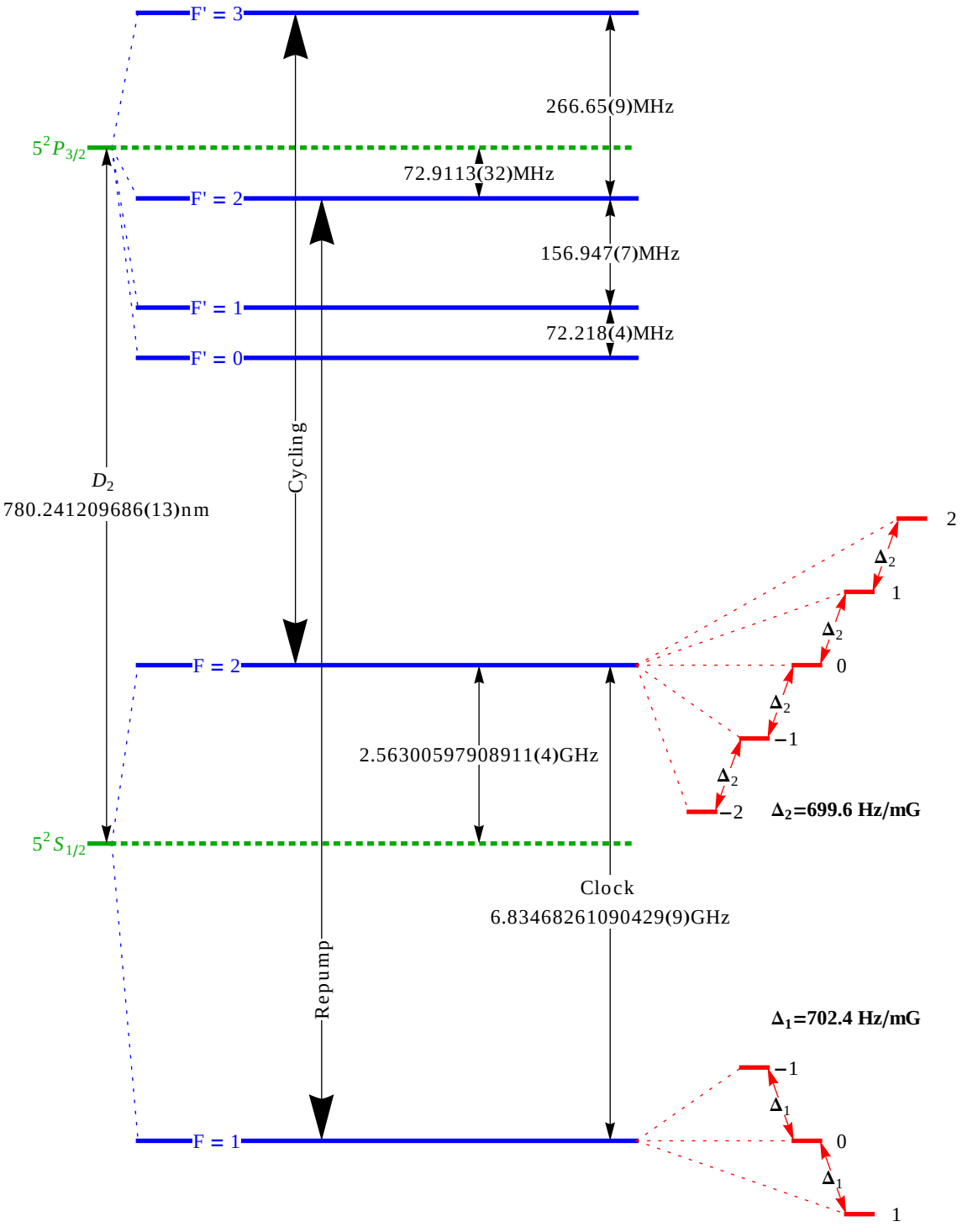

Figure 3.1: Rubidium ^{87}Rb D_2 transition hyperfine structure [132, 133, 134].

non-zero magnetic field, the Zeeman effect shifts the energy of these sublevels. The Zeeman energy shift can be calculated using the Breit-Rabi formula [132, 22]

$$\begin{aligned} E_{|f,m_f\rangle} &= -\frac{E_{hfs}}{8} - g_I \mu_I B m_f - \frac{1}{2} E_{hfs} \sqrt{1 + x m_f + x^2} \\ x &= \frac{(g_J \mu_B + g_I \mu_I) B}{E_{hfs}} \end{aligned}$$

Here E_{hfs} is the hyperfine energy splitting, g_I and g_J are the Landé g-factor of the nucleus and the valance electron, μ_I and μ_B are the nuclear magnetic moment and the Bohr magneton, and B is the magnetic field. The energy level diagram of ^{87}Rb is shown in Figure 3.1.

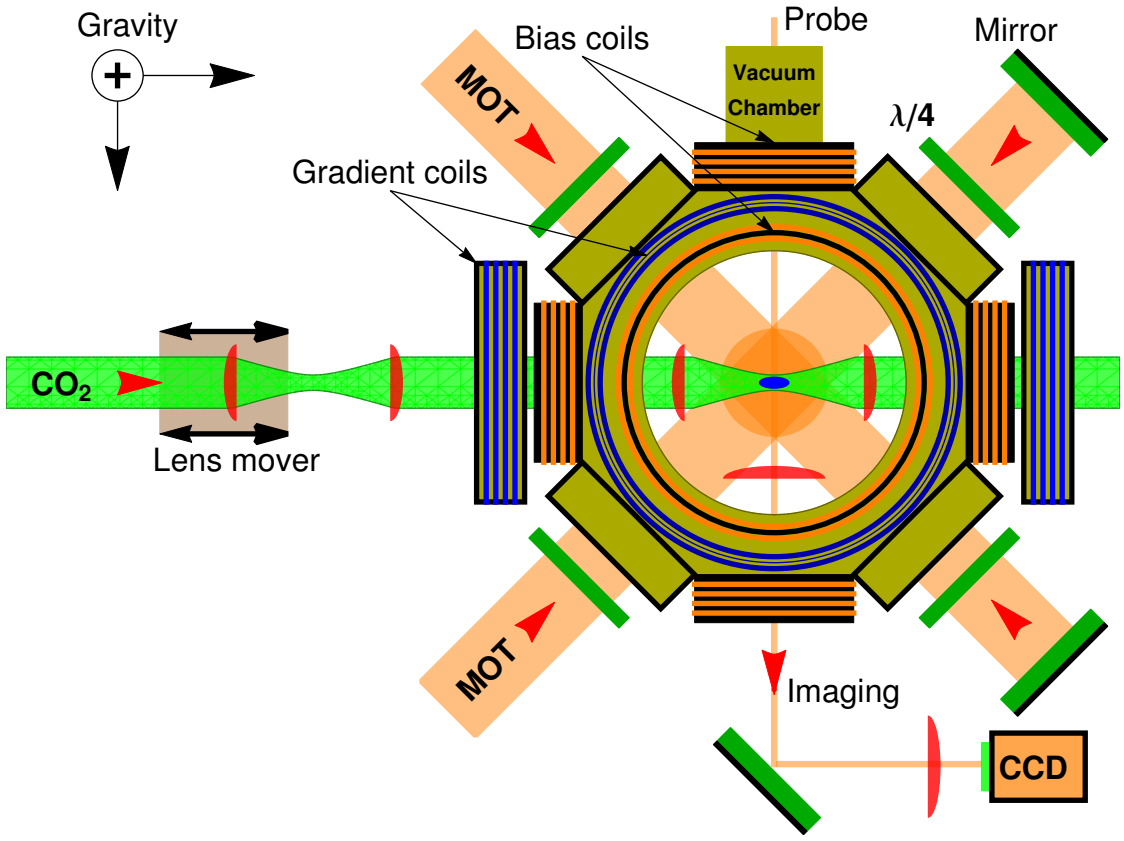

Figure 3.2: Diagram of the vacuum chamber.

3.1.2 Vacuum Chamber System

The main chamber is an stainless stainless machined octagon from Kimball physics. There are two anti-reflective 6" glass windows, five anti-reflective 2.75" glass windows for laser beams, two 2.75" zinc selenide windows for CO_2 laser beams, and one long port with an anti-reflective 2.75" glass window for the imaging probe laser beam. Inside the chamber, there are two zinc selenide focusing lenses of 3.8 cm focal length. The first lens focuses the CO_2 beam for the dipole trap, and the beam exits the chamber through the second lens. Also, there is a 5 cm focusing lens to collect light for imaging, and a rubidium getter source is inside the chamber. The pressure inside the chamber is $10^{-10} - 10^{-11}$ torr and maintained by an ion pump and a titanium sublimation pump.

3.1.3 Magneto Optical Trap (MOT)

The magneto optical trap follows the standard configuration with anti-Helmholtz gradient magnetic coils and 3 pairs of retro-reflected laser beams [131](Figure 3.3). The power of each laser beam is about $30 - 35$ mW and the beam diameter is 1.0". The anti-Helmholtz coils create a spatial dependence in the Zeeman energy splitting of atoms as shown in Figure 3.4. To describe the principle behind the MOT, let us consider atoms with a ground state of spin $|f = 0\rangle$, and excited state of spin $|f = 1\rangle$. The presence of a magnetic field shifts the energy of the Zeeman sub-levels by an amount $\Delta E = \mu m_f B$, here μ is Zeeman energy splitting constant, m_f is Zeeman sublevels, and B is the magnetic field. The laser beams are red detuned, with circular polarization σ^+ and σ^-. Atoms at $z > 0$ will absorb more σ^- photons, and atoms at $z < 0$ will absorb more σ^+ photons due to spatial dependence of Zeeman energy [131]. As a result, the MOT confines atoms at the center of the trap (the zero magnetic field position). The trap depth of a typical MOT is on the order of a few mK.

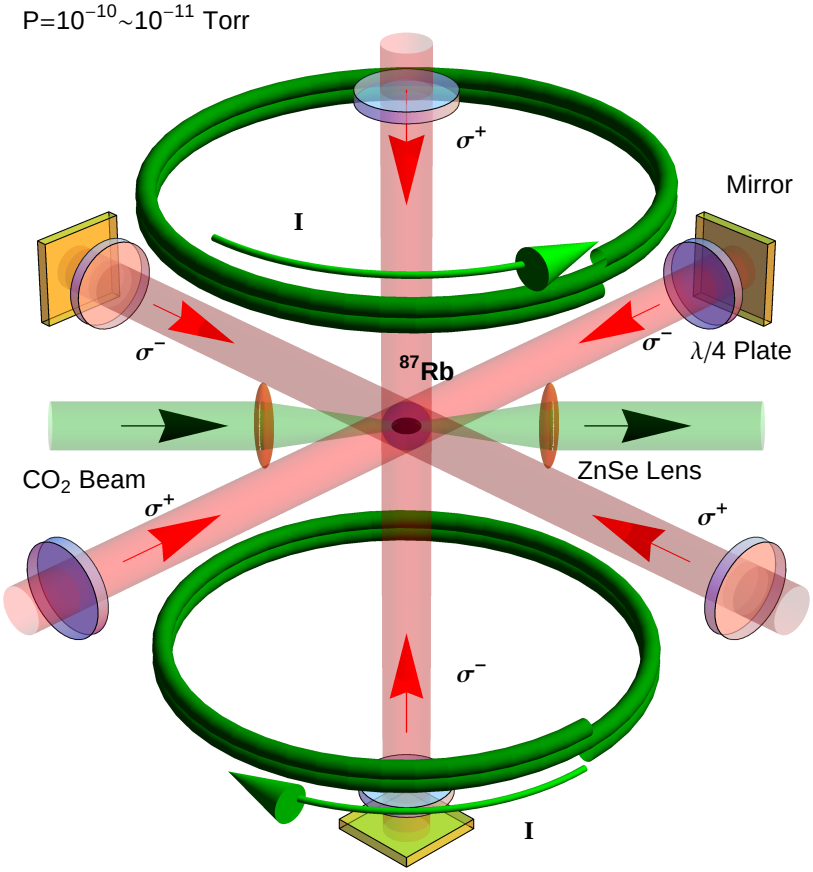

Figure 3.3: Magneto optical trap and CO_2 laser dipole force trap. The MOT configuration includes two magnetic coils in the anti-Helmholtz configuration and 3 retro-reflected laser beams.

3.1.4 MOT Laser

In the case of rubidium atoms (as seen in the energy level diagram Figure 3.1), its simple hyperfine structure does not require a very complicated laser setup for cooling. We can use 780 nm laser diodes for both the cycling and repump transitions and the lasers can be fine-tuned to the specific wavelength for a desired transition.

The cycling transition transfers atoms between $F = 2 \leftrightarrow F' = 3$. Details about the cycling transition laser setup are shown in Figure 3.5. The optical setup looks complicated; however, its goal is simple. We aim for a power of order $\sim$ 100 mW

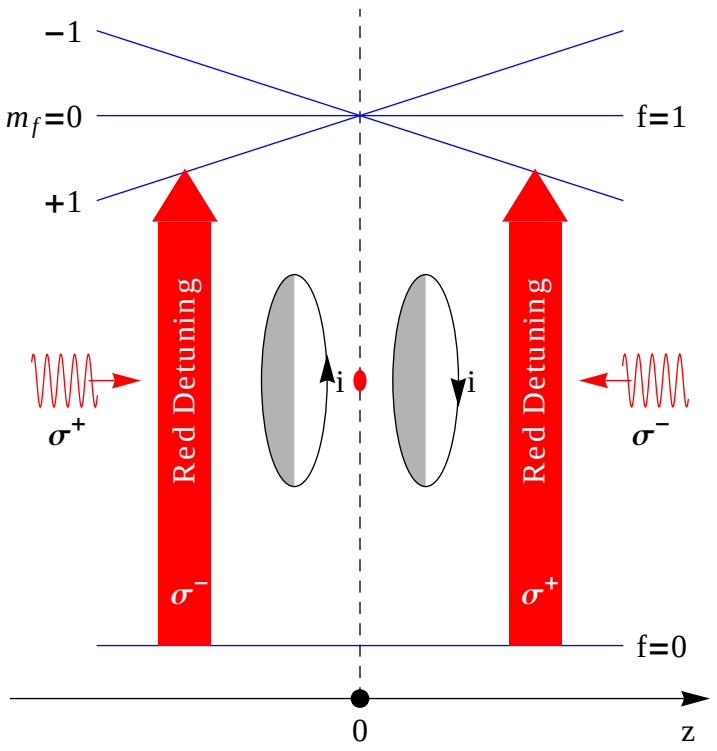

Figure 3.4: Spatial energy dependent and MOT beam polarization. The anti-Helmholtz coils create a spatial dependence in Zeeman energy for atoms. The two circularly polarized beams with opposite helicity apply stronger pressure on atoms as they move away from the center of the trap.

into the chamber and the ability to shift the laser beam frequency from −250 MHz to within a few MHz of the cycling transition. The first goal is achieved using a tapered amplifier (TA) which can emit up to 1 W of power. The frequency shifting is achieved by passing the beam through a series of acousto optical modulators (AOM).

Repump transition : during the cycling transition, there is a possibility that atoms jump from $F = 2 \rightarrow F' = 2$, and fall back from $F' = 2 \rightarrow F = 1$. We need a repump laser to put atoms back to the cycling transition. This laser transfers atoms between $F = 1 \leftrightarrow F' = 2$ if atoms fall back to $F = 1$. There is a possibility that atoms will fall from $F' = 2 \rightarrow F = 2$ which will place them back into the cycling transition. The repump laser optical setup is less complicated than the cycling

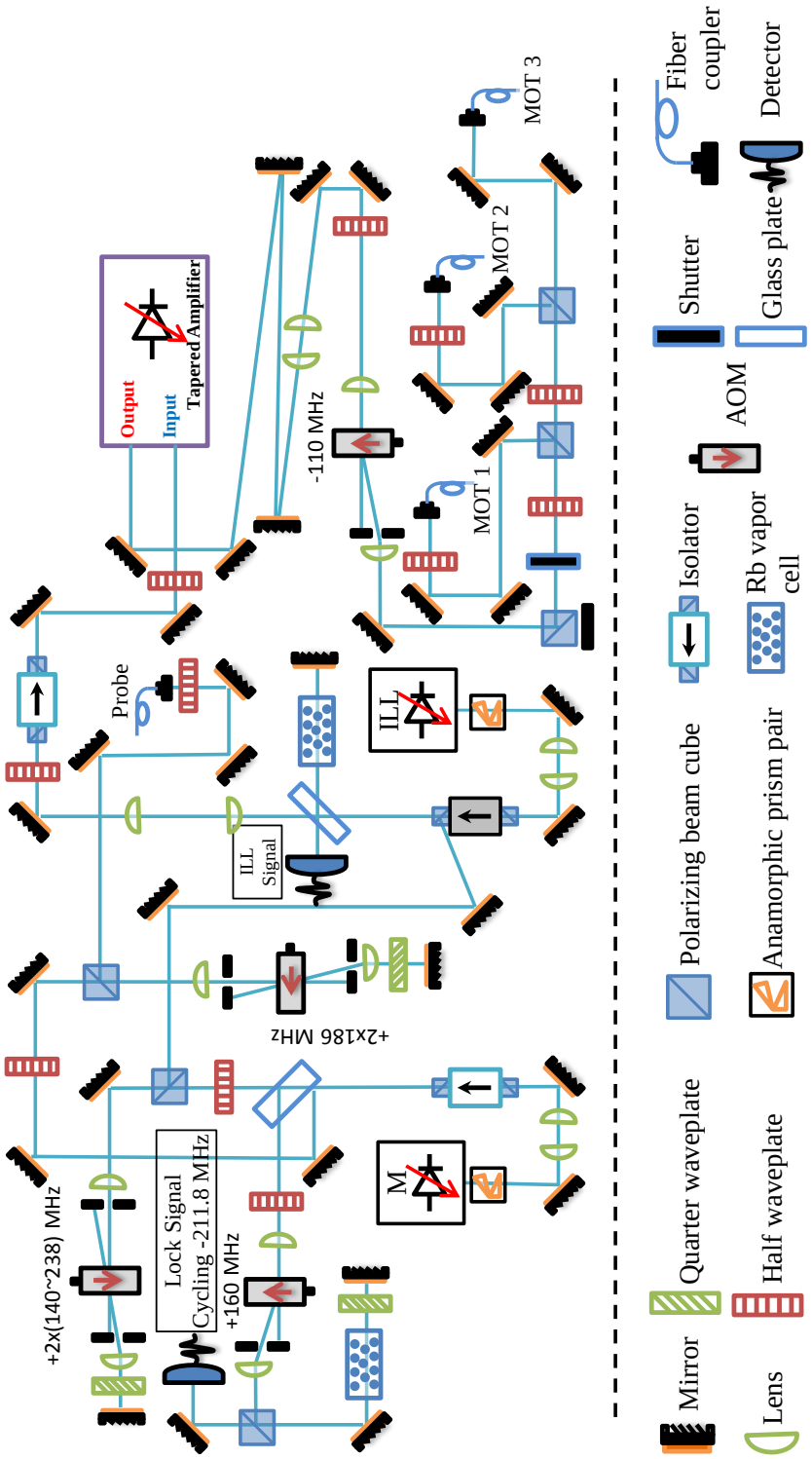

Figure 3.5: Master laser setup [130].

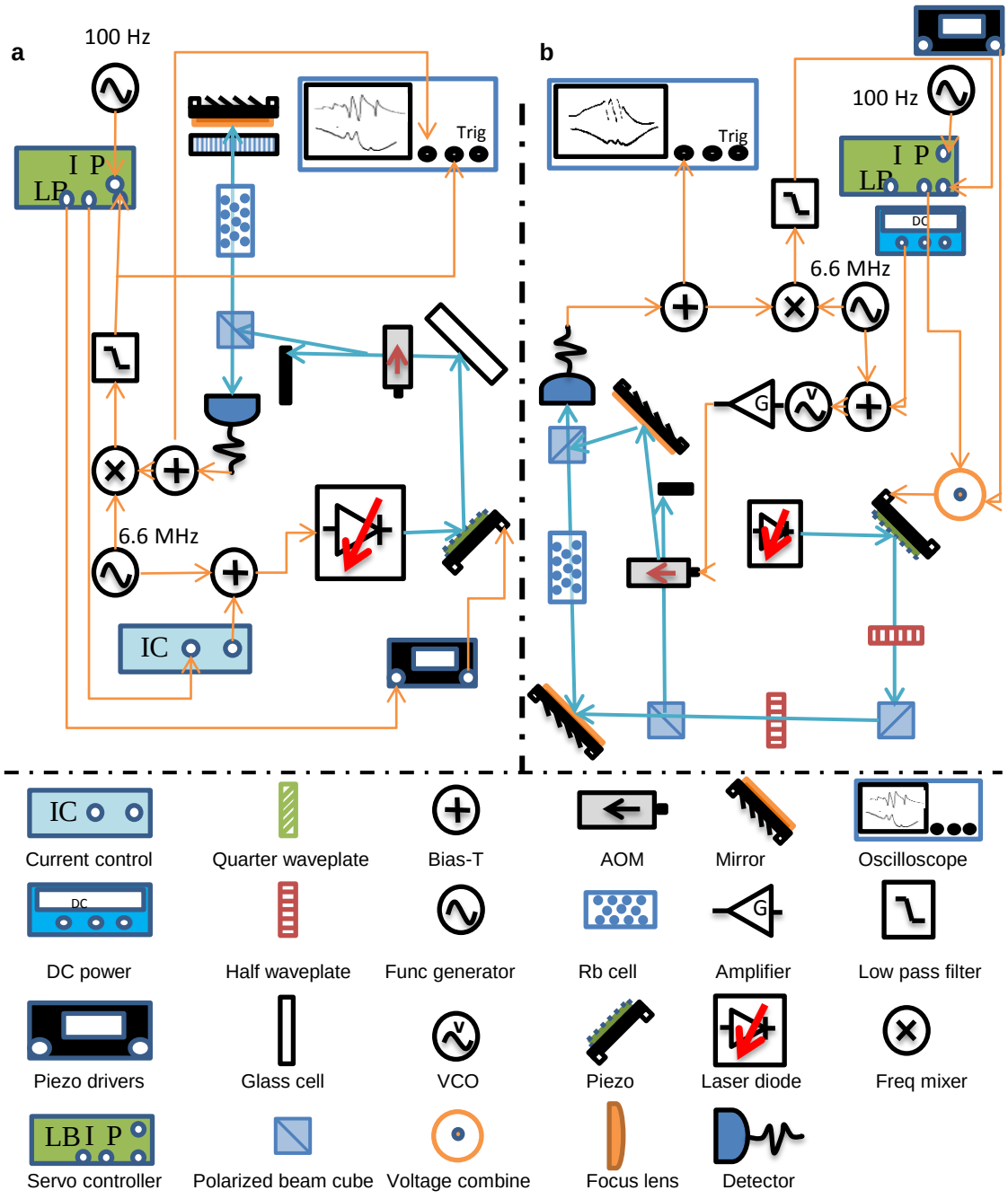

Figure 3.6: Laser locking set up. (a) Locking set up for the master laser, (b) locking set up for the repump laser.

because we only need $15 - 20$ mW into the chamber. The repump laser is locked at the repump transition, and the frequency is shifted by an AOM which results in -80 MHz from the repump transition. The beam from the repump laser then is seeded

into an injection locked laser by an optical fiber. The beam of the injection locked laser passes through a second AOM which shifts the beam frequency +80 MHz. The resulting beam, which is resonant with the repump transition, is coupled into the chamber via an optical fiber.

In order to keep the frequency of laser light tuned to the atomic transitions, the lasers are locked using a PID control. The locking signal for the cycling laser is generated by modulating its current, and the locking signal for the repump laser is generated by modulating the AOM frequency shift. The advantage of the latter method is that modulating AOM frequency shift does not induce frequency sideband on the main laser beam. Thus, no laser power is wasted in the sidebands. The laser locking diagram is shown in Figure 3.6.

3.1.5 Magnetic Coils.

Magnetic coils are among the most important components of the BEC experiment. All the coils are located outside the vacuum chamber (Figure 3.2). The magnetic coils, depending on the configuration, play different roles in the experiment.

Gradient coils. In the experiment, there are 2 pairs of gradient coils. One pair of gradient coils is for the magneto optical trap, and one pair of gradient coils is used to purify the spin components of the condensate and as Stern-Gerlach coils to spatially separate the spin components during imaging. Although, one gradient coil could do all the work, the extra pair of coils gives us more flexibility in the experiment.

Bias magnetic coils. There are three pairs of bias coils used to cancel the external magnetic field and set a desired magnetic field along the CO_2 laser axis (quantization axis). Three pairs of coils generate magnetic fields in three orthogonal directions: along gravity, along the CO_2 laser beam, and along the imaging directions.

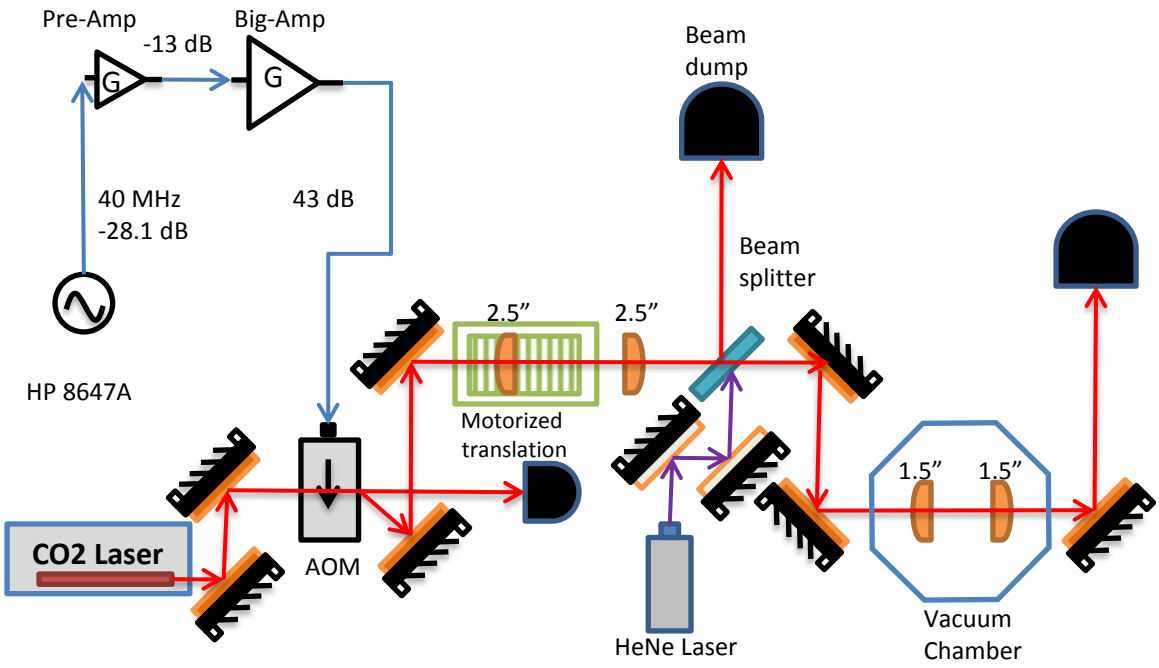

Figure 3.7: CO2 laser setup.

Gradient compensation coils The external magnetic gradient is approximately 100 mG/cm. There is a pair of small gradient coils attached to the ZnSe window. These coils generate a magnetic field gradient to cancel the external magnetic gradient along the CO_2 laser beam at the location of the BEC.

3.1.6 CO_2 Laser Dipole Trap

The CO_2 laser dipole trap is a central component of the experiment; it relies on the principle of an induce electric dipole moment interacting with the electric field gradient of the laser beam. The Bose-Einstein condensate is formed and held at the focus of the CO_2 laser. The CO_2 laser induces a dipole moment $\vec{p} = \alpha\vec{E}$ in the atom, where α is the atomic polarizability, and $\vec{E}$ is the electric field of laser. Consequently, the induced dipole moment of the rubidium atoms are effectively trapped by the potential of the laser's electric field. The intensity gradient of the laser creates a spatially dependent electric potential, $U = -\langle\vec{p}\cdot d\vec{E}\rangle = -\frac{1}{2}\langle\vec{p}\cdot\vec{E}\rangle$. Here, the brackets

represent the time averaged potential. The CO_2 laser was chosen to be the dipole trap for two main reasons. First, the laser emits a wavelength of 10.6 μm which is far detuned from any atomic transition of rubidium atoms; the radiation force due to photon scattering is negligible as compared to the dipole force [136]. Second, its effective short Rayleigh range allows a Bose-Einstein condensate to form and be confined in a single focus beam.

A detailed discussion of the CO_2 laser optical dipole force trap can be found in Refs. [136, 128, 22]. In this section, we will provide some of the basic information about the potential energy and the photon scattering rate of the dipole force trap. The laser light is far detuned with $|\Delta| = |\omega - \omega_0|$, where ω is the angular frequency of the laser, and ω_0 is the cycling resonance frequency of rubidium atoms. The potential and the scattering rate in the case of a far-off resonance trap (FORT) are [136]

$$\begin{aligned} U(\vec{r}) &= -\frac{3\pi c^2}{2\omega_0^3}\frac{\Gamma}{\omega_0-\omega}I(\vec{r}) = -\frac{3\pi c^2}{2\omega_0^3}\frac{\Gamma}{\Delta}I(\vec{r}) \\ \Gamma_{sc}(\vec{r}) &= \frac{3\pi c^2}{2\hbar\omega_0^3}\left(\frac{\Gamma}{\omega_0-\omega}\right)^2 I(\vec{r}) = \frac{3\pi c^2}{2\hbar\omega_0^3}\left(\frac{\Gamma}{\Delta}\right)^2 I(\vec{r}) = \frac{\Gamma}{\hbar\Delta}U(\vec{r}) \end{aligned}$$

where the on resonance damping rate $\Gamma = (\frac{\omega_0}{\omega})^2\Gamma_\omega$ and damping rate $\Gamma_\omega = -\frac{F_{rad}}{m_e} = \frac{e^2\omega^2}{6\pi\epsilon_0 m_e c^3}$. In fact, the wavelength of the CO_2 laser is extremely off resonant $\omega \ll \omega_0$. In this scenario

$$\begin{aligned} U(\vec{r}) &= -\frac{3\pi c^2\Gamma}{\omega_0^4}I(\vec{r}) = -\frac{\alpha_s}{2\epsilon_0 c}I(\vec{r}) \\ \Gamma_{sc}(\vec{r}) &= \frac{3\pi c^2}{2\hbar\omega_0^3}(2\frac{\Gamma}{\omega_0})^2 I(\vec{r}) = 2\frac{\Gamma}{\hbar\omega_0}(\frac{\omega}{\omega_0})^3 U(\vec{r}) \end{aligned}$$

where $\alpha_s = \frac{6\pi\epsilon_0 c^3\Gamma}{\omega_0^4}$ is the static polarizability. For a CO_2 laser, the scattering rate is 1.1 photon per atom every hours![22]

The experimental CO_2 laser setup is illustrated in Figure 3.7. The CO_2 laser outputs ~100 W. It first passes through an AOM; the zero order diffraction goes to a beam dump, and the +1 diffracted order is used for the experiment. The main purpose of the AOM is to control the power of the laser beam. The beam then

passes through the first set of 1:1 telescopes with the first focus lens motorized on a translation stage (lens mover). The second set of 1:1 telescopes are fixed inside the chamber. Moving the lens gives us the ability to change the focus of the beam inside the vacuum chamber. Tightening the beam focus increases the trap depth and the confinement of the trap. To load more atoms during initial trap loading, we us the maximum power of the CO_2 laser with a large beam waist inside chamber. To create a BEC, we apply evaporative cooling by lowering CO_2 laser power such that the hot atoms escape, at the same time decreasing the trap volume by focusing the beam to increase the density and thus the collision rate. In general, the first lens moves forward 10 mm in order to decrease the beam waist inside chamber to about 25 μm.

3.2 Interacting with a BEC

Creating a Bose-Einstein condensate is only the first step of our investigation. In order to prepare condensates in different experimental scenarios, we must interact with the condensate. In the context of our experiment, we interact with the condensate through a microwave horn, an rf coil, and the magnetic field coils. The microwave transition works in the hyperfine regime, and the rf transition works in the Zeeman sub-levels of the hyperfine states. The magnetic field introduces the quadratic Zeeman energy into the spinor energy. The schematics of the microwave and rf system are described in Figure 3.8 and the magnetic field is produced by the magnetic coils previously discussed.

3.2.1 Microwave

A microwave transition transfers atoms between sub-levels of the hyperfine structure of $f = 1$ and $f = 2$. In a large enough magnetic field to lift the degeneracy of the sub-levels, the microwave transition can be approximated as a 2-level system, for instance, microwave transition between $|f = 1, m_f = 0\rangle$ and $|f = 2, m_f = 0\rangle$. A sample of the microwave Rabi flopping is shown in Figure 3.9 a; the microwave pulse transfers the

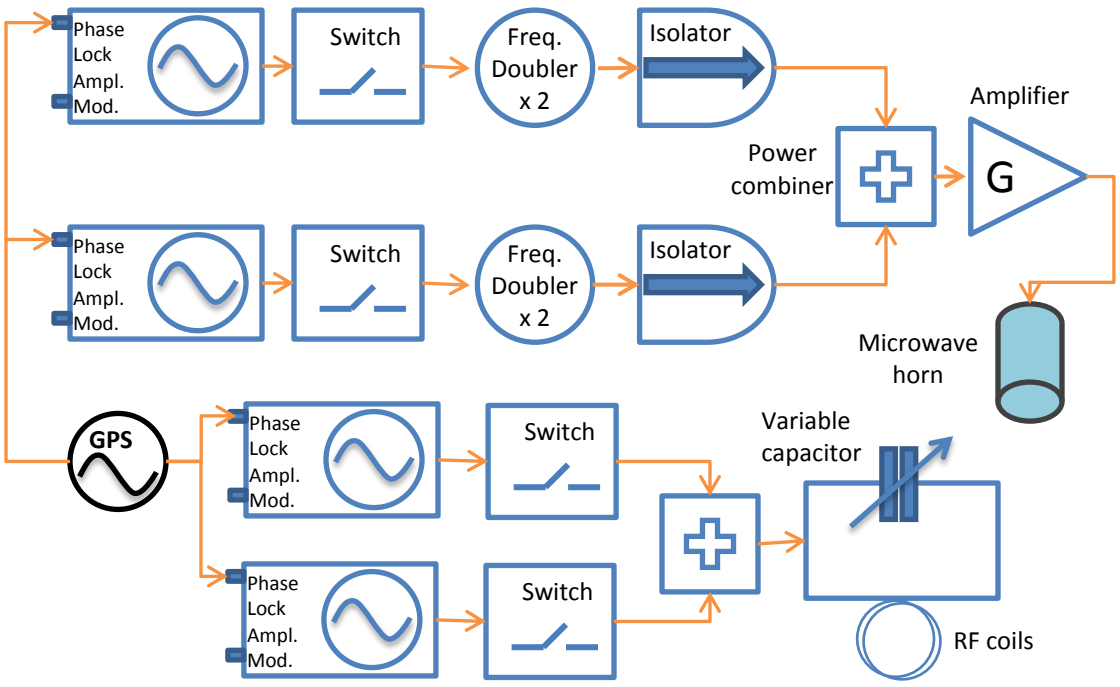

Figure 3.8: Microwave and rf setup.

population N_0 of atoms in $m_f = 0$ state between $f = 1$ and $f = 2$.

The microwave manipulation is a very useful for our investigation. Microwave spectroscopy is used to measure the magnetic field, zero the B-field, and shift the phase of the condensate quantum states. The magnetic field splits energy of Zeeman sub-level of hyperfine structure by $\Delta E_m = m_f p B_z$ where ΔE_m is energy shift, $m_f = -f, -f+1, ...f$ are the Zeeman sub-levels, $p \approx 700$ Hz/mG is the linear Zeeman effect, and B_z is the magnetic field. By measuring the frequency difference between the transition from $|f = 1, m_f = 0\rangle$ to $|f = 2, m_f = 0, 1\rangle$, one can determine the magnetic field B_z. By adjusting the currents in the three bias coils with the feedback from the magnetic field measurement, we can zero the magnetic field to within a few mG.

Another important role of the microwave transition is to shift the phase of the spinor condensate [64]. For a two-level system $|g\rangle = |f = 1, m_f = 0\rangle$ and $|e\rangle = |f =$

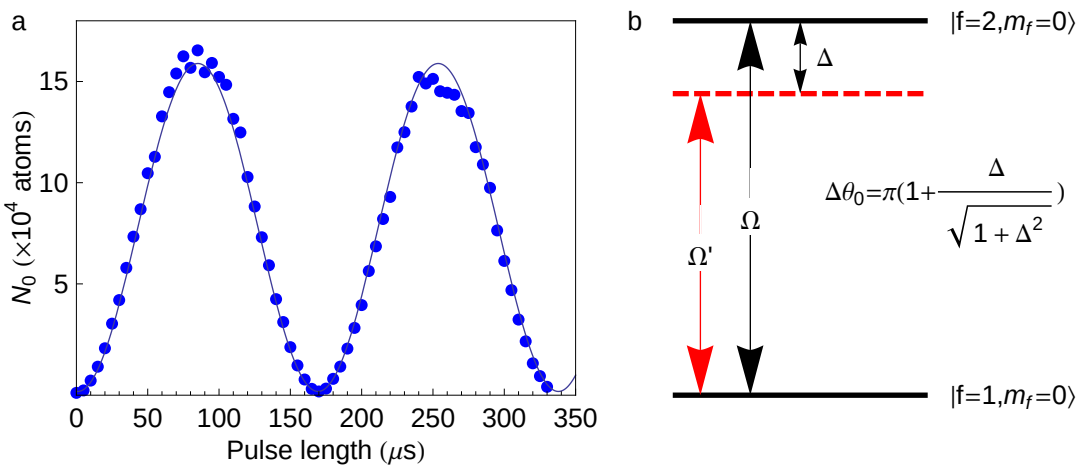

Figure 3.9: Microwave Rabi rate and phase shift. (a) Sample of a resonance microwave Rabi rate $|f=1, m_f=0\rangle$ and $|f=2, m_f=0\rangle$. (b) Microwave phase shift on $|f=1, m_f=0\rangle$ quantum state for a detuning $\Delta = \delta/\Omega$ normalized to resonance Rabi rate.

$2, m_f = 0\rangle$ [137], the wave function can be written as $|\psi(t)\rangle = c_g(t)|g\rangle + c_e(t)|e\rangle$. The time evolution in the presence of the microwave field is

$$\begin{aligned} c_e(t) &= i\frac{\Omega}{\Omega'}\sin\frac{\Omega' t}{2}e^{i\delta t/2} \\ c_g(t) &= \left(\cos\frac{\Omega' t}{2} - i\frac{\delta}{\Omega'}\sin\frac{\Omega' t}{2}\right)e^{i\delta t/2} \end{aligned}$$

where the effective Rabi rate $\Omega' = \sqrt{\Omega^2 + \delta^2}$, Ω is the Rabi rate, and δ is the detuning. An off-resonance microwave transition with an effective 2π pulse length, $T' = \frac{2\pi}{\Omega'}$, induces a phase shift of the $|f=1, m_f=0\rangle$ relative to the $|f=1, m_f=\pm 1\rangle$ state as the atoms completely transfer from $|f=1, m_f=0\rangle$ to near $|f=2, m_f=0\rangle$ and back to $|f=1, m_f=0\rangle$. The phase of the $m_f=0$ component is shifted by an amount $\Delta\theta_0 = 2\pi$ if the detuning is zero. For a detuning of $\Delta = \frac{\delta}{\Omega}$, the phase of $m_f=0$ atoms is shifted by an amount $\Delta\theta_0 = \pi(1+\Delta/\sqrt{1+\Delta^2})$. This results in a quadrature phase shift of $\Delta\theta = -\Delta\theta_0$ [56]. The diagram for the off-resonant microwave phase shift is shown in Figure 3.9 b.

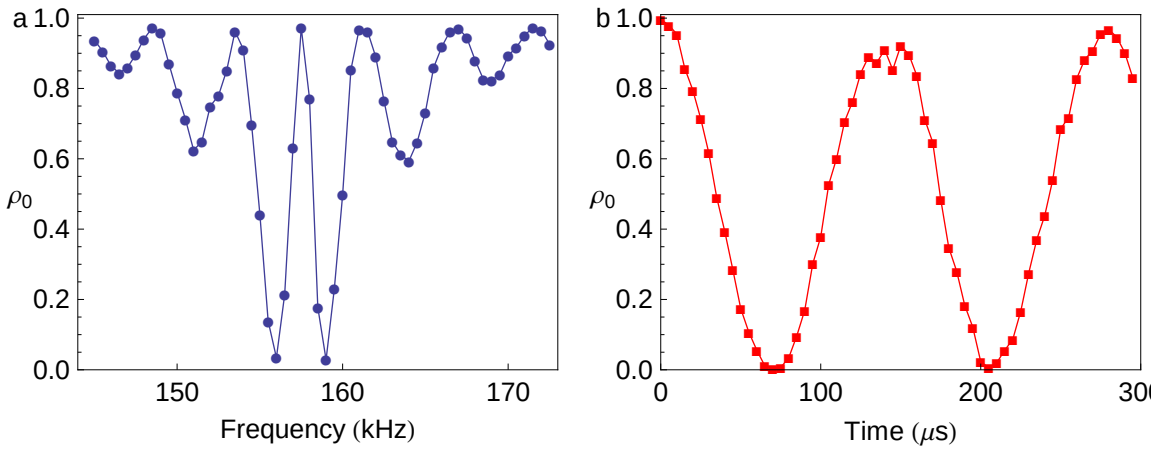

Figure 3.10: rf spectrum and rf Rabi. (a) rf spectrum, (b) rf Rabi rate between $|f = 1, m_f = 0, \pm 1\rangle$

3.2.2 RF system

The RF transition transfers atoms between Zeeman sub-levels of given hyperfine states. For the hyperfine state $f = 1$, RF transitions transfer atoms between the 3-level system of $|f = 1, m_f = 0, \pm 1\rangle$. Similar to microwave spectroscopy, RF spectroscopy can be used to measure the magnetic field. A sample of the RF spectrum used to determine the magnetic field is shown in Figure 3.10 (a). In the sample, the resonance frequency (center peak) is at 158.5 kHz which corresponds to $B = 158.5/p = 226$ mG, here p is a linear Zeeman effect.

The RF transition is also used to prepare a coherent spin state with a fractional population $\rho_0 = N_0/N$ for initial state preparation by varying the pulse length as shown in Figure 3.10 b.

3.2.3 Magnetic Field

Spinor condensates can also be controlled through the use of a magnetic field. The magnetic field can control the phase transition [46, 47, 48] and modulate the spinor energy of condensate. The magnetic field, as discussed previously, is generated by the bias magnetic coils. The magnitude of the magnetic field is determined by the voltage of power supply across the coils that is controlled by the analog outputs of the

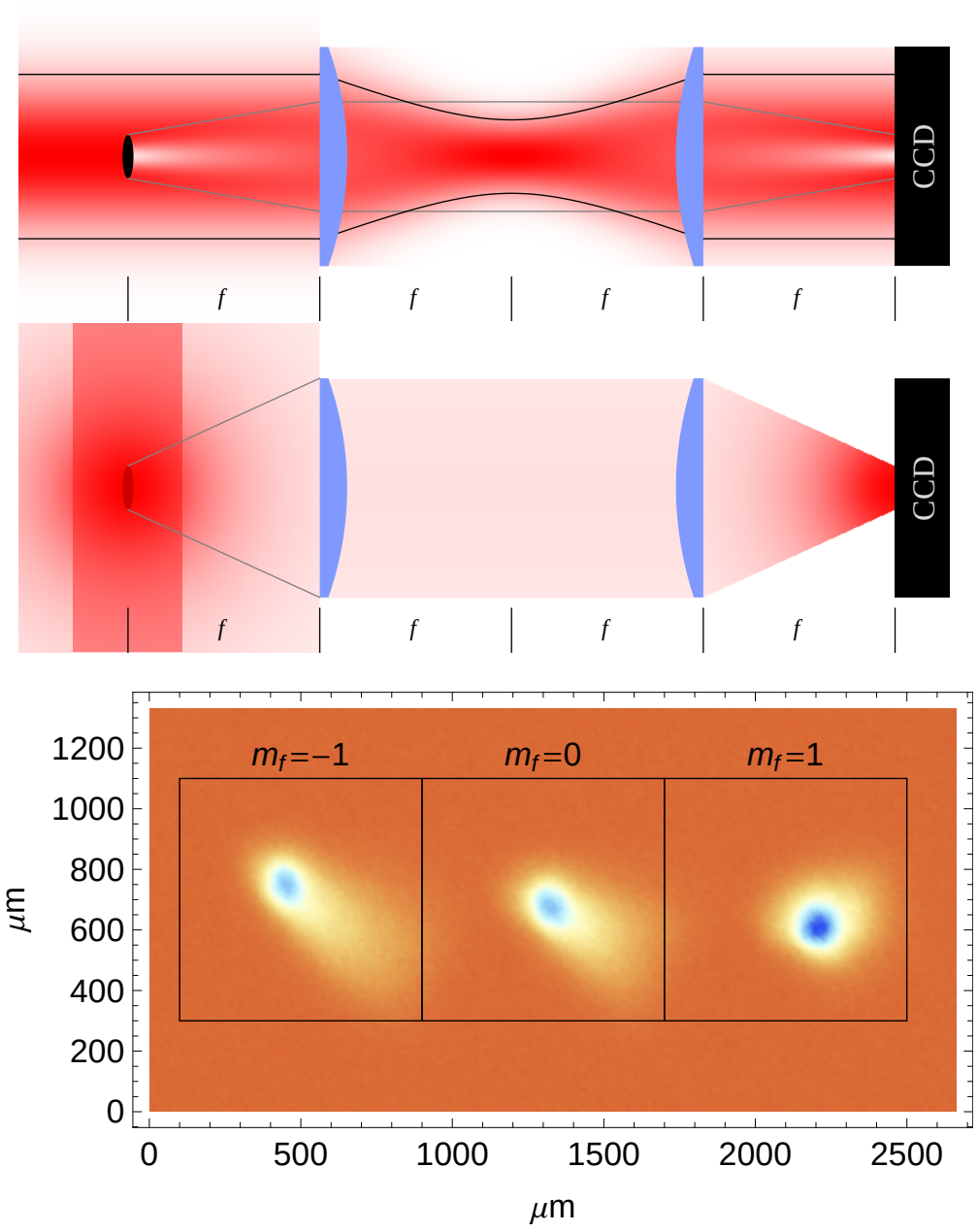

Figure 3.11: Imaging configurations. Absorption imaging configuration (top) and fluorescence imaging configuration (middle). Figures are reproduced from Chris Hamley's work [64]. Image of BEC after 22 ms time of flight (bottom). Three clouds show the density plot of BEC components which are separated by Stern-Gerlach gradient.

National Instruments (NI) cards. This enables us to modulate the voltage across the coils to generate different wave forms scenarios for the magnetic fields, from sinusoidal,

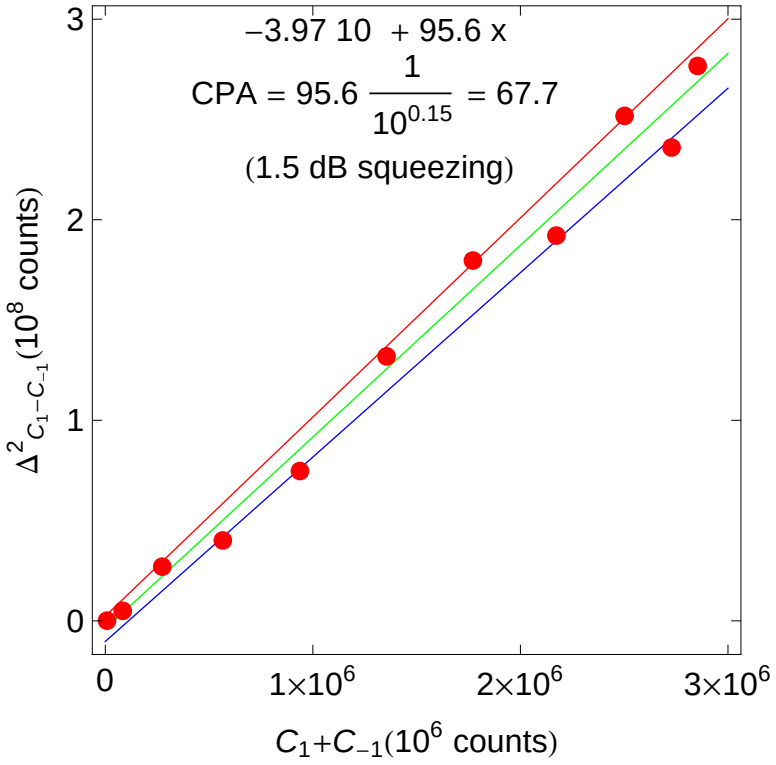

Figure 3.12: RF calibration. The plot of transferred atoms counts $C_1 + C_{-1}$ and the magnetization variance counts $\Delta^2_{C_1-C_{-1}}$ is fitted to a linear function. In the unit of atoms $\Delta^2_{N_1-N_{-1}} = N_1 + N_{-1}$, thus the slope of the fit (95.6) is the conversion of counts per atom (CPA). Correcting for the squeezing factor (0.15), CPA$= 95.6/10^{0.15} = 67.7$ counts/atom.

linear ramping, to square pulses.

3.3 Data Acquisition

We acquire data by imaging the condensate and counting the number of atoms. There are two primary techniques used in imaging, fluorescence and absorption. In fluorescence imaging, atoms are illuminated with laser beams from three retro-reflection and orthogonal directions, and images are taking by collecting the scattered light the from atoms. In absorption imaging, a probe beam is passed through the condensate of atoms, and CCD camera acquires the image of the probe beam with the shadow of the condensate. The diagrams of both imaging configurations and a sample of

fluorescence image are shown in Figure 3.11. The CCD camera collects photons and converts the number of photons into the number of electrons. By performing an RF calibration, we can determine the number of atoms from the number of electron counts given by the CCD images [62, 129].

RF transition is used to calibrate the electron counts into atom counts. Starting from an initial state of $m_f = 0$, rotated with an RF transition, the Poissonian quantum projection noise of magnetization is equal to the square root of total atom transfer from $m_f = 0$ to $m_f = \pm 1$, $\Delta_{N_1 - N_{-1}} = \sqrt{N_1 + N_{-1}}$ [62]. The electron count per atoms conversion can be obtain from the fit of the total transfer to $m_f = \pm 1$ atom counts $C_1 + C_{-1}$ and magnetization variance count $\Delta^2_{C_1 - C_{-1}}$. A sample of the RF calibration is shown in Figure 3.12.

3.4 Control System

Two computers, a Labview computer and an Andor computer, are used to control experimental procedure and acquire data. We use the Labview program to control the experiment and the Andor BASIS program to acquire data images. The Labview program controls experiment through multiple PCI cards in a PCI chassis and USB-RS232 ports. The diagram of the control system and list of devices are shown in Figure 3.13. The computer controls the microwave and RF system through GPIB, acquires image from a COHU camera through a frame grabber PCI-1407, controls 24 analog voltage outputs and 16 digital voltage outputs through NI cards PCI-6733 and PCI-6534, and control the lens mover and the SmartArb pulse generator through RS232 ports.

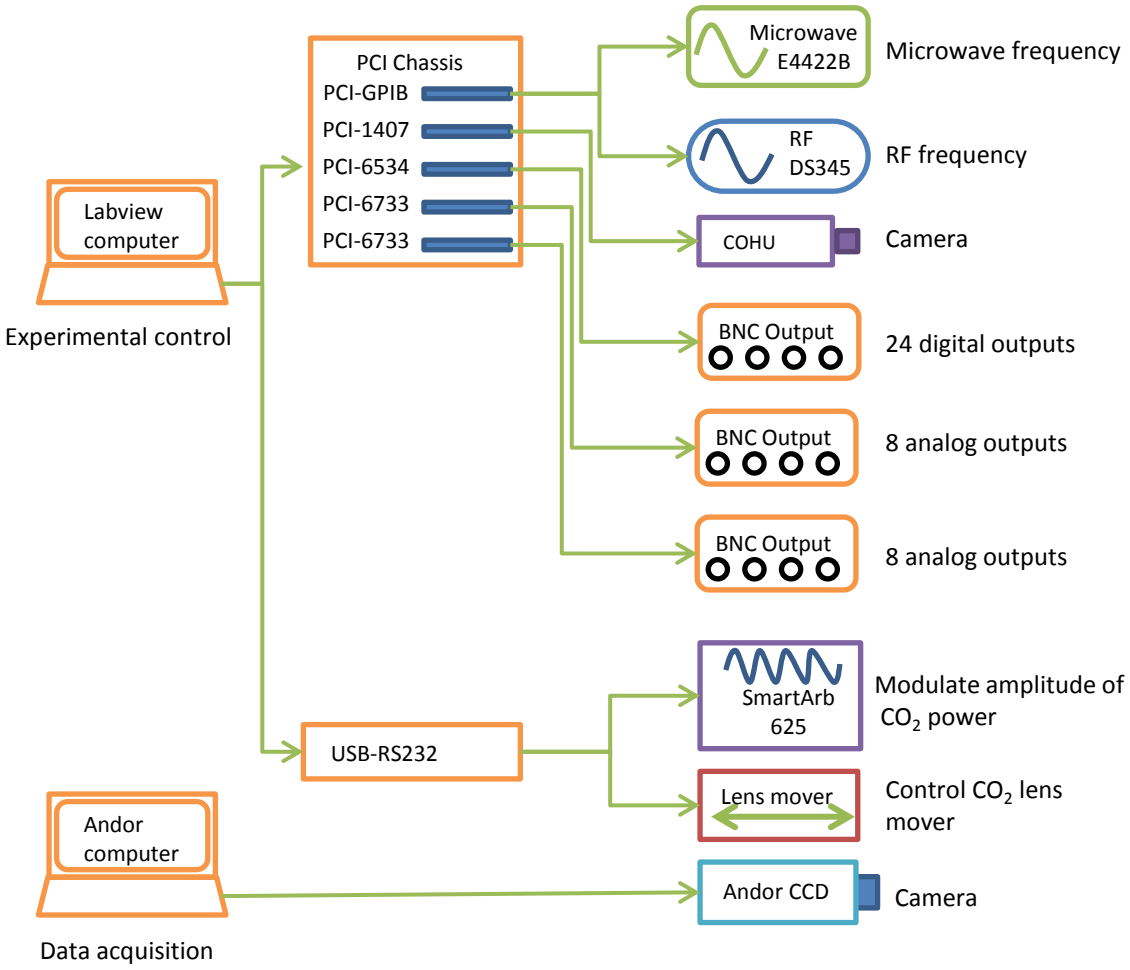

Figure 3.13: Experimental control system.

CHAPTER 4

STABILIZATION THEORY

In spinor BEC, when the quadratic Zeeman effect $q = q_Z B^2 < 2|c|$, there exists an unstable equilibrium hyperbolic fixed point at the top pole of spin-nematic $S_\perp Q_\perp x$ sphere, and the non-equilibrium quantum spin dynamics are an analog of an inverted pendulum. The unstable equilibrium dynamics provide a great playground for the studying quantum stabilization in a many-body system.

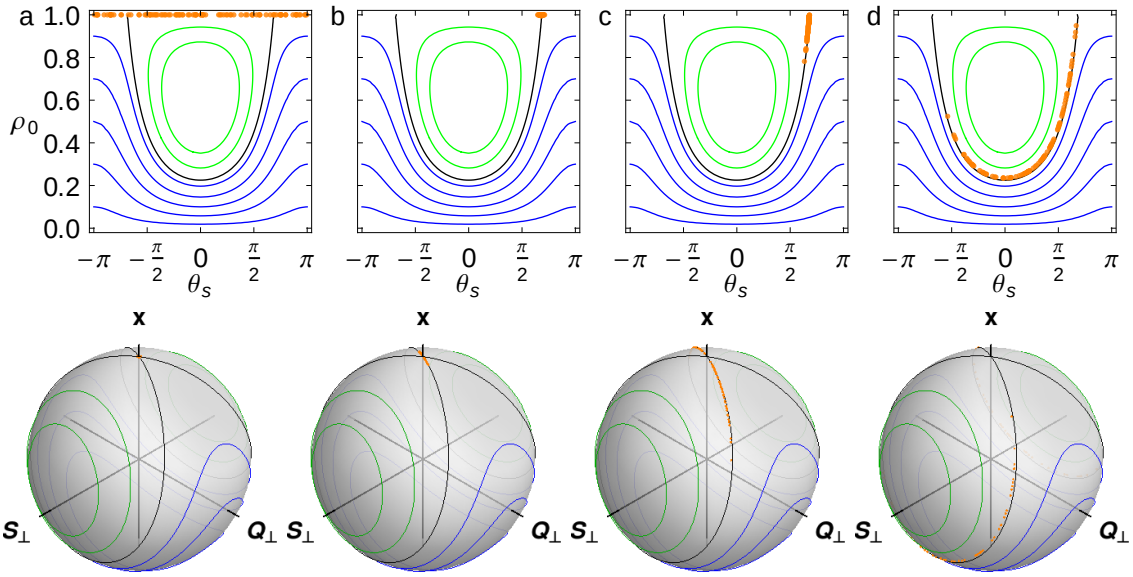

Figure 4.1: Spinor phase and spin-nematic sphere. Dynamical evolution at 0 ms (a), 50 ms (b), 100 ms (c), and 150 ms (d) in spinor phase (top) and spin-nematic phase (bottom) for 40,000 atoms. The condensate (orange) is initiated at hyperbolic fixed point with uncertainty at the SQL level; the noise then squeezes below the SQL, and evolve along separatrix.

4.1 Spinor Dynamics Picture

What happens when $q < 2|c|$? To answer this question, we first look at the spin-nematic sphere $S_\perp Q_\perp x$, as shown in Figure 4.1 (bottom). The emergence of separatrix

(zero energy contour) introduces different scenarios for the quantum spin dynamics. The dynamics along the negative (green) and positive (blue) energy contours are the orbiting and the phase winding coherent oscillations about the stable elliptical fixed point. In comparison to the double well condensate, the phase winding is an analog of plasma oscillations and the orbiting is the self-trapping oscillations [123, 124]. The unstable equilibrium dynamics occur at the unstable hyperbolic fixed point at the top pole of the sphere. For a condensate initiated at the hyperbolic fixed point, freely evolution leads to squeezing and spinor population dynamics. In the spin-nematic phase, the quantum uncertainty along the divergent separatrix grows above the SQL and reduces below the SQL in the transverse direction. The continued development of noise along the divergent separatrix leads to the evolution away from the hyperbolic fixed point. In the spinor phase space $\theta_s\rho_0$, the spinor phase is initial undefined, and the ρ_0 distribution is non-Gaussian with the mean value $\rho_0 \approx 1$ [61]. During the squeezing period, the spinor phase approaches a definite value $\cos\theta_s = -\frac{q}{c} - \frac{1}{2}$. After the squeezing period, the quantum spin mixing of the condensate occurs along the separatrix to value of $\rho_0 < 1$. Stabilizing these unstable equilibrium dynamics are our goal.

4.1.1 Classical Pendulum Analogy

The spinor energy of Eqn 2.19 can be written in the form of a non-rigid pendulum [51, 109, 61]

$$\mathcal{H}_a = \frac{|c|}{4}\left[x^2 - 1 - (x^2 - 1)\cos\theta_s\right] + \frac{q}{2}(1 - x) \tag{4.1}$$

This Hamiltonian is similar to the Bose-Hubbard model [125, 123] for the Bose-Josephson junction [138, 37]. The Hamiltonian of a classical pendulum is described by

$$E = \frac{l^2}{2}(\frac{d\phi}{dt})^2 + gl(1 - cos(\phi)) \tag{4.2}$$

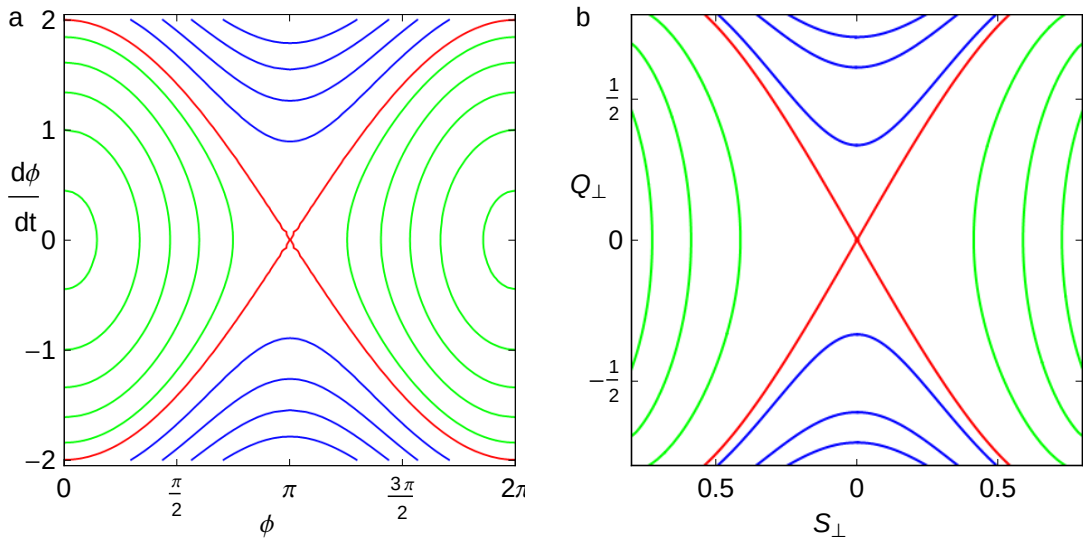

Figure 4.2: Spin-nematic and phase space trajectory. The phase space trajectory (a) of the pendulum with the hyperbolic fixed point at $(\pi, 0)$, the separatrix (red) separates the librational (green) from rotational (blue) motion. Spin nematic $(S_\perp, Q_\perp)$ space of spinor condensate (b) with the hyperbolic fixed point at (0,0), separatrix (red), negative energy contour (green), and positive energy contour (blue).

The phase trajectories $(\phi, \frac{d\phi}{dt})$, of the pendulum are shown in Figure 4.2 (a) by plotting contours of Eqn 4.2. There exist 2 types of equilibrium fixed points, stable elliptic fixed points at $(0, 0)$ and $(2\pi, 0)$ and an unstable hyperbolic fixed point at $(\pi, 0)$. They are periodic every 2π. The separatrices intersect at a hyperbolic fixed point separating the librational oscillation and the rotational motion of the pendulum.

The spin-nematic phase space $S_\perp Q_\perp$ with the hyperbolic fixed point (Figure 4.2 a) of a spinor condensate has a similar structure to the phase trajectories of a classical pendulum at its hyperbolic fixed point $(0, \pi)$. The point $(0, \pi)$ in the phase trajectories corresponds to the inverted pendulum position.

4.2 Stabilization Concept

It has been known that unstable systems can be dynamically stabilized by applying a periodic force [139]. The inverted pendulum stabilized by vertically vibrating the pivot point, known as Kapitzas pendulum, is a classic example of this non-intuitive

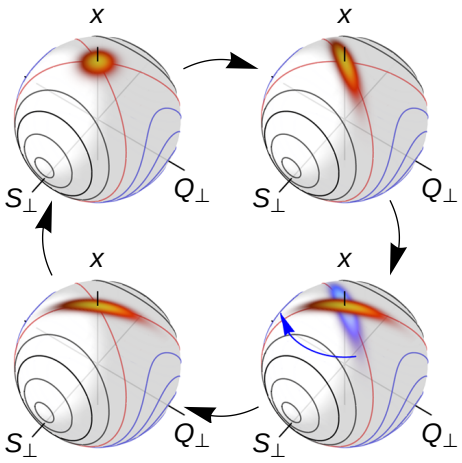

Figure 4.3: Stabilization concept. The condensate is initialized at the pole of the spin-nematic sphere with Heisenberg-limited uncertainties in $S_\perp$ and $Q_\perp$ (upper left). Initial evolution produces squeezing along the diverging manifold of the separatrix (upper right). The quantum state is quickly rotated (blue arrow) to the converging manifold of the separatrix using a microwave field pulse (lower right). Subsequent the evolution of the rotated state (lower left) unsqueezes the condensate, returning it close to the original state (upper left). Reproduced from [82]

phenomenon [71, 140]. In the spinor condensate, the non-equilibrium dynamics are stabilized by periodically rotating its quadrature phase shift. The stabilization concept is shown in Figure 4.3. The condensate is initialized at the pole of the spin-nematic sphere with Heisenberg-limited uncertainties $1/\sqrt{N}$ in $S_\perp$ and $Q_\perp$. Initial evolution produces squeezing along the diverging manifold of the separatrix, and subsequently leads to the non-equilibrium dynamics. To stabilize the system, we need to prevent the non-equilibrium dynamics from occurring. The quantum state is quickly rotated (blue arrow) to the converging manifold of the separatrix using a microwave field pulse. Subsequent evolution of the rotated state unsqueezes the condensate and returns it close to the original state. Repeating these rotations periodically can keep the condensate in the squeezing-unsqueezing loop and stabilize its dynamics about the hyperbolic fixed point [82].

4.3 Stabilization Theory

In the stabilization regime, the dynamics occur near the top of the spin-nematic sphere. This is the low depletion limit where $\hat{N}_0 \approx \hat{N}$. In order to linearize the equations of motion, we expand the operators about the expectation values of this initial state, $\hat{\mathcal{A}} = \langle \mathcal{A} \rangle + \delta\hat{A}$. The only nonzero expectation values are

$$\begin{aligned} \langle \hat{\mathcal{Q}}_{0+} \rangle &= -2N \\ \langle \hat{\mathcal{Q}}_{0-} \rangle &= 2N. \end{aligned}$$

These expectation values also indicate quantum limited uncertainty of $\sqrt{N}$ in $\hat{\mathcal{S}}_x$, $\hat{\mathcal{S}}_y$, $\hat{\mathcal{Q}}_{xz}$, and $\hat{\mathcal{Q}}_{yz}$ since these operators are the commutators of $\hat{\mathcal{S}}_x$ with $\hat{\mathcal{Q}}_{yz}$ and $\hat{\mathcal{S}}_y$ with $\hat{\mathcal{Q}}_{xz}$ respectively. Keeping the terms linear in $\delta\hat{A}$, and eliminating the higher order terms of $\delta\hat{A}$ and the products of $\delta\hat{A} \cdot \delta\hat{B}$, the dynamic equations of motion Eqn 2.22 become

$$\begin{aligned} \delta\dot{\hat{\mathcal{S}}}_x &= -\frac{q}{\hbar}\delta\hat{\mathcal{Q}}_{yz} \\ \delta\dot{\hat{\mathcal{S}}}_y &= \frac{q}{\hbar}\delta\hat{\mathcal{Q}}_{xz} \\ \delta\dot{\hat{\mathcal{Q}}}_{yz} &= \frac{4N\lambda}{\hbar}\delta\hat{\mathcal{S}}_x + \frac{q}{\hbar}\delta\hat{\mathcal{S}}_x \\ \delta\dot{\hat{\mathcal{Q}}}_{xz} &= -\frac{4N\lambda}{\hbar}\delta\hat{\mathcal{S}}_y - \frac{q}{\hbar}\delta\hat{\mathcal{S}}_y \end{aligned} \tag{4.3}$$

These equations describe the quantum dynamics in the neighborhood of the pole at which squeezing happens. In order to determine the stability condition, we make a mean-field approximation by replacing the operator $\delta\hat{\mathcal{A}}$ with its expectation value δA. Since $\langle \hat{\mathcal{A}} \rangle = 0$ for all the dynamical operators, we will drop the δ notation of the expansion. Since the dynamics in $\{\hat{\mathcal{S}}_x,\ \hat{\mathcal{Q}}_{yz},\ \hat{\mathcal{Q}}_{0+}\}$ and $\{\hat{\mathcal{S}}_y,\ \hat{\mathcal{Q}}_{xz},\ \hat{\mathcal{Q}}_{0-}\}$ are degenerate, we can reduce the problem into a single space by using

$$\mathcal{S}_\perp^2 = \mathcal{S}_x^2 + \mathcal{S}_y^2 \qquad \mathcal{Q}_\perp^2 = \mathcal{Q}_{yz}^2 + \mathcal{Q}_{xz}^2$$

Since $\mathcal{S}_\perp^2$ and $\mathcal{Q}_\perp^2$ synchronize to the Larmor precession, we can define

$$\begin{aligned} \mathcal{S}_x &= \mathcal{S}_\perp \cos(\frac{\theta_m}{2})_{t=0} \qquad & \mathcal{Q}_{yz} &= -\mathcal{Q}_\perp \cos(\frac{\theta_m}{2})_{t=0} \\ \mathcal{S}_y &= -\mathcal{S}_\perp \sin(\frac{\theta_m}{2})_{t=0} \qquad & \mathcal{Q}_{xz} &= -\mathcal{Q}_\perp \sin(\frac{\theta_m}{2})_{t=0} \end{aligned}$$

The system of equations Eqn4.3 simplifies into [82]

$$\begin{aligned} \dot{\mathcal{S}}_\perp &= \tilde{q}\mathcal{Q}_\perp \\ \dot{\mathcal{Q}}_\perp &= -\left(2\tilde{c}+\tilde{q}\right)\mathcal{S}_\perp \end{aligned}$$

with spinor dynamical rate $c = 2N\lambda$, where $\tilde{c} = c/\hbar$ and $\tilde{q} = q/\hbar$ are angular frequencies.

4.3.1 Stabilization Condition

The dynamic equations can be written in a matrix form

$$\begin{pmatrix} \dot{\mathcal{S}}_\perp \\ \dot{\mathcal{Q}}_\perp \end{pmatrix} = \begin{pmatrix} 0 & \tilde{q} \\ -\left(2\tilde{c}+\tilde{q}\right) & 0 \end{pmatrix} \begin{pmatrix} \mathcal{S}_\perp \\ \mathcal{Q}_\perp \end{pmatrix}$$

Defining the above matrix as $\mathbf{m}$, the time evolution is given by its exponentiation. The quadrature phase shift used for stabilization is given by the operator $\exp\left(-\imath\Delta\theta\hat{\mathcal{Q}}_{zz}\right)$, which is a plane rotation in $\{\mathcal{S}_\perp, \mathcal{Q}_\perp\}$ by an angle $\Delta\theta$. The full dynamics from one pulse to another, including the dynamics from $\mathbf{m}$ and the quadrature phase shift, are given by

$$\mathbf{M} = \mathbf{R}[\Delta\theta] \cdot \exp[\tau\mathbf{m}]$$

where τ is the period between pulses, $\mathbf{R}$ is a 2-dimensional rotation matrix, and $\Delta\theta$ is the amount of the quadrature phase shift.

Using the same stability analysis technique employ in optical resonator theory, we verify that the dynamics of $\mathcal{S}_\perp$ and $\mathcal{Q}_\perp$ stay bounded if the trace $|\mathrm{Tr}[\mathbf{M}]| < 2$.

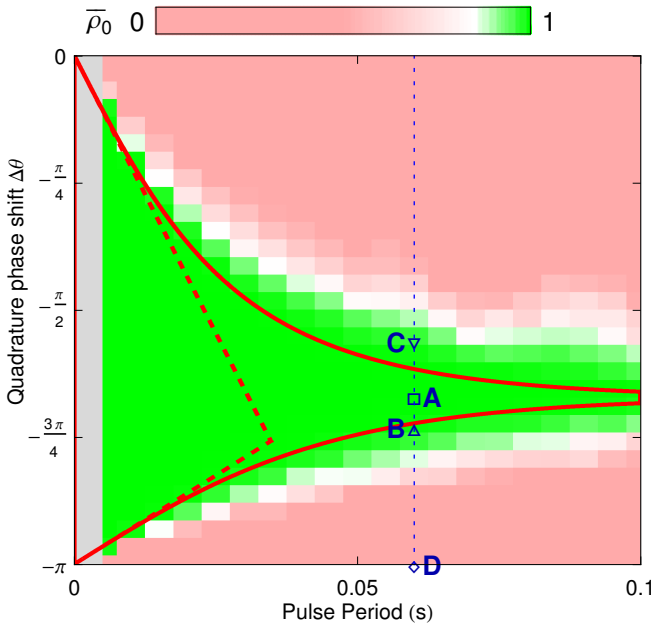

Figure 4.4: Simulation and analytical fit of stability diagram. To map the stability region, the mean ρ_0 is measured at the time of the maximum spin mixing for the unstabilized condensate. The solid curves are the envelope of the calculated stability region using linear stability analysis while the dashed curves use a time-averaged Hamiltonian approach. The red curves use the measured values $B = 210$ mG, $c = -5.5 \times 2\pi$ Hz.

Evaluating this condition gives the inequality [82],

$$2\left|\cos\Delta\theta\cosh\Gamma\tau + \frac{\tilde{c}+\tilde{q}}{\Gamma}\sin\Delta\theta\sinh\Gamma\tau\right| < 2 \tag{4.4}$$

with $\Gamma = \sqrt{\tilde{q}(2|\tilde{c}| - \tilde{q})}$. This inequality is used to mark the boundaries of the analytic stability region, which is compared to simulations in Figure 4.4.

The stabilization can also be analyzed by using a magnetic field pulses with length τ and amplitude $\tilde{q}_P$ repeated with period T with the interim field having amplitude $\tilde{q}_0$.

$$\mathbf{M} = \exp[(T-\tau)\mathbf{m}(\tilde{q}_0)] \cdot \exp[\tau\mathbf{m}(\tilde{q}_P)]$$

In this form, the stabilization condition is given by

$$|2\cosh\Gamma_0(T-\tau)\cosh\Gamma_P\tau - 2\frac{\tilde{q}_0\tilde{q}_P + \tilde{c}(\tilde{q}_0+\tilde{q}_P)}{\Gamma_0\Gamma_P}\sinh\Gamma_0(T-\tau)\sinh\Gamma_P\tau| < 2 \tag{4.5}$$

with $\Gamma_{0/P} = \sqrt{-q_{0/P}(2c + q_{0/P})}/\hbar$.

4.3.2 Effective quadratic Zeeman analysis

For a ferromagnetic spinor BEC, the spinor dynamical rate $c < 0$. When the quadratic Zeeman $q > 2|c|$ or $q < 0$, the population does not evolve. The quadrature rotation $\Delta\theta$ is the angle rotation about the x or $-\mathcal{Q}_{zz}$ axis. In fact, the operator $\hat{\mathcal{Q}}_{zz}$ is the rotation operator in the spin-nematic $\mathcal{S}_\perp \mathcal{Q}_\perp$ space.

$$|\psi(t)\rangle_{\Delta\theta} = e^{-i(-\hat{\mathcal{Q}}_{zz})\Delta\theta/2}|\psi(t)\rangle$$

The Hamiltonian of the system is $\mathcal{H} = \lambda\hat{\mathcal{S}}^2 + p\hat{\mathcal{S}}_z + \frac{q}{2}\hat{\mathcal{Q}}_{zz}$. The term responsible for the quadrature rotation is $\frac{q}{2}\hat{\mathcal{Q}}_{zz}$. The evolution due to the quadratic Zeeman energy alone is

$$|\psi(t)\rangle_{\Delta\theta} = e^{iq\hat{\mathcal{Q}}_{zz}t/2\hbar}|\psi(t)\rangle$$

Therefore, the quadrature rotation due to the quadratic Zeeman energy is $\Delta\theta = q\tau/\hbar$. This can also be seen from the dynamical matrix $\mathbf{M}$. The microwave pulse generates an instantaneous quadrature rotation of $\Delta\theta$. Therefore, over one period of the periodic microwave pulse sequence we can calculate an effective quadratic Zeeman, $q_{\text{eff}} = q + \hbar\Delta\theta/\tau$. The spin-nematic phase space is cyclic with a period of π. So an instantaneous phase shift of $\Delta\theta$ is equivalent to a phase shift of $\Delta\theta - \pi$, which is a negative contribution to q_{eff}. Therefor q_{eff} is double valued everywhere. For both $q_{\text{eff}} > 2|c|$ and $q_{\text{eff}} < 0$ there is no longer a hyperbolic fixed point centered on the $m_f = 0$ state [82]. Wherever these conditions are met for both of the q_{eff} values, the system is in the robust stable region. This region is bounded by the dashed lines in the stability diagram 4.4.

CHAPTER 5

STABILIZATION EXPERIMENT

In this chapter, we will describe our stabilization experiment in a Bose-Einstein condensate and discuss the experimental results. The stabilization concept relies on rotating the phase of quantum states. In the context of this study, we will present two different stabilization methods using the microwave pulse and the magnetic field pulses.

What are our observables? The distribution of stabilized quantum states localizes about the hyperbolic fixed point on the top pole of the spin-nematic sphere. This location corresponds to the spinor population $\rho_0 = 1$; hence, the value ρ_0 determines whether the system is stable. Moreover, the uncertainty of the stabilized distribution is bounded; we can use the transverse magnetization noise $\Delta S_\perp$ as an alternative parameter to verify the dynamic stabilization.

5.1 Stabilization with Microwave Pulses First Attempt

The technique of using microwaves to rotate the phase of quantum states has been proven to be a robust method in our spin-nematic squeezing experiment [56]. Once again, the technique is applied in our stabilization experiment.

5.1.1 Experimental Method

The stabilization concept was described in Figure 4.3. The condensate is initialized at the hyperbolic fixed point $x = 1, S_\perp = Q_\perp = 0$. The condensate has Heisenberg-limited uncertainties in $S_\perp$ and $Q_\perp$. Initial free evolution of the condensate produces spin-nematic squeezing along the diverging manifold of the separatrix and leads to the

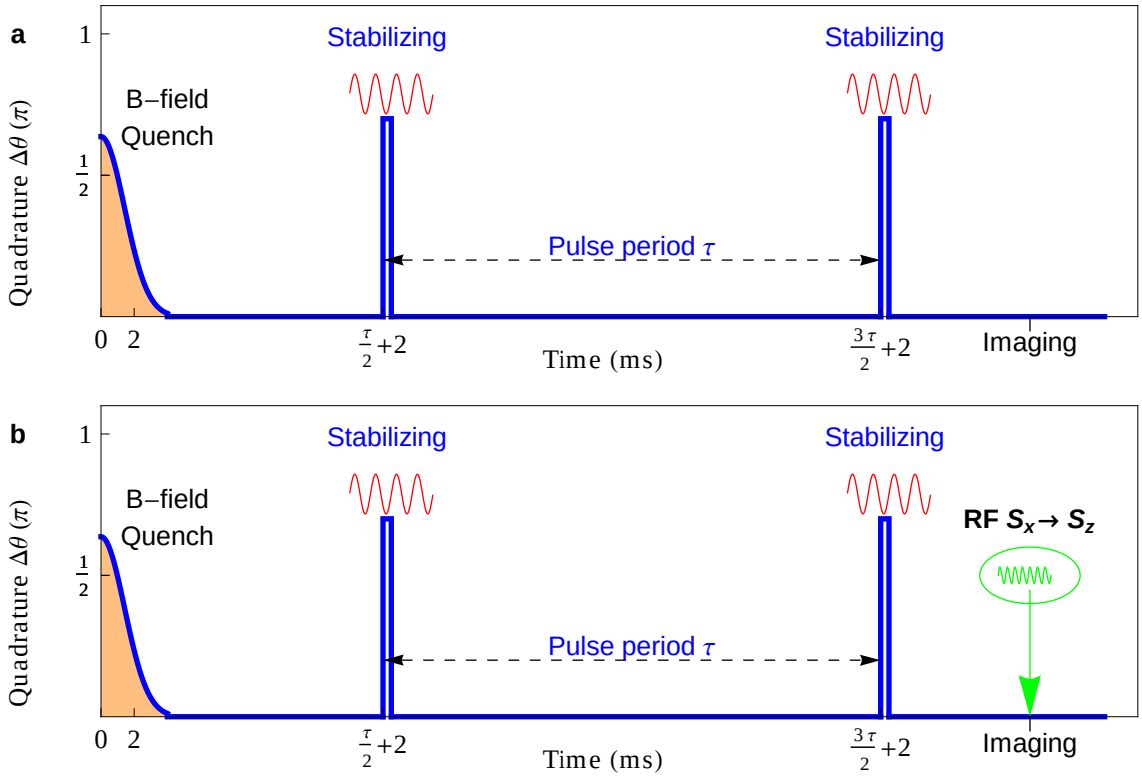

Figure 5.1: Microwave pulse stabilization experimental sequences. To initiate the dynamics, the magnetic field is quenched from 2 G to 200 mG. Each microwave pulse is separate by a period τ. (a) The imaging setup measures the spinor population, and (b) measures the transverse magnetization by applying an RF field to rotate $S_x \rightarrow S_z$.

non-equilibrium spin mixing dynamics. To maintain the condensate in the equilibrium position, the quantum state of the condensate is quickly rotated to the converging manifold of the separatrix using a microwave field pulse. The subsequent free evolution unsqueezes the condensate, returns it close to the original state, and squeeze along the diverging manifold of the separatrix again. Periodic microwave pulses of period τ are applied to rotate the quadrature phase by an amount $\Delta\theta$ to keep the condensate in a squeezing-unsqueezing loop, and stabilize the spinor dynamics about the hyperbolic fixed point [82].

The experiment is performed with a condensate of $N = 3 \times 10^4$ atoms initiated in the $|f = 1, m_f = 0\rangle$ state at a high magnetic field 2 G. To initiate the dynamics, the

magnetic field is quenched below the quantum critical point to 220 mG. A sequence of microwave pulses of period τ is applied to stabilize the system. Finally, the spin populations of the condensate are measured. This is executed by releasing the trap and allowing the atoms to freely expand in a Stern-Gerlach magnetic field gradient to separate the m_f spin components. To measure the transverse magnetization $S_\perp$, an RF $\pi/2$ pulse is applied to rotate $S_\perp \rightarrow S_z$ before imaging. The experimental sequence is shown in Figure 5.1.

5.1.1.1 Microwave phase shift

The microwave pulse transfer atoms between $|f = 1, m_f = 0\rangle$ and $|f = 2, m_f = 0\rangle$ and back. A microwave pulse with detuning δ results in a phase shift $\Delta\theta_0 = \pi(1 + \frac{\Delta}{\sqrt{1+\Delta^2}})$ in $|m_f = 0\rangle$. Here, $\Delta = \delta/\Omega$ is the normalized detuning to resonance Rabi rate of the two level system. The quadrature phase shift in the spin-nematic space is $\Delta\theta = -\Delta\theta_0$. The detail microwave setup is described in Section 3.2.1.

5.1.2 Spinor Population

The population ρ_0 is one of the observables for stabilization. The value of the stabilized population ρ_0 will stay close to 1 if the condensate remains localized on the top pole of the $S_\perp Q_\perp x$ sphere (Figure 4.3). To verify the stabilization dynamics, we measure the evolution of population dynamics ρ_0. The spinor dynamics of stabilized condensates for different microwave pulse periods are demonstrated in Figure 5.2. For unstabilized system (microwave pulses are off) Figure 5.2 a, the squeezing mechanics pauses the spinor dynamics for about 100 ms, followed by a large amplitude oscillation in the ρ_0 spinor population. When the microwave pulses are turned on, the spinor dynamics are stabilized. The results are shown for microwave pulses τ ranging from $30 - 60$ ms. During first 500 ms of evolution, the stabilization is almost perfect for $\tau \leq 40$ ms. For longer pulse periods, the system is still stabilized after a certain time, then eventually evolves away from stabilization.

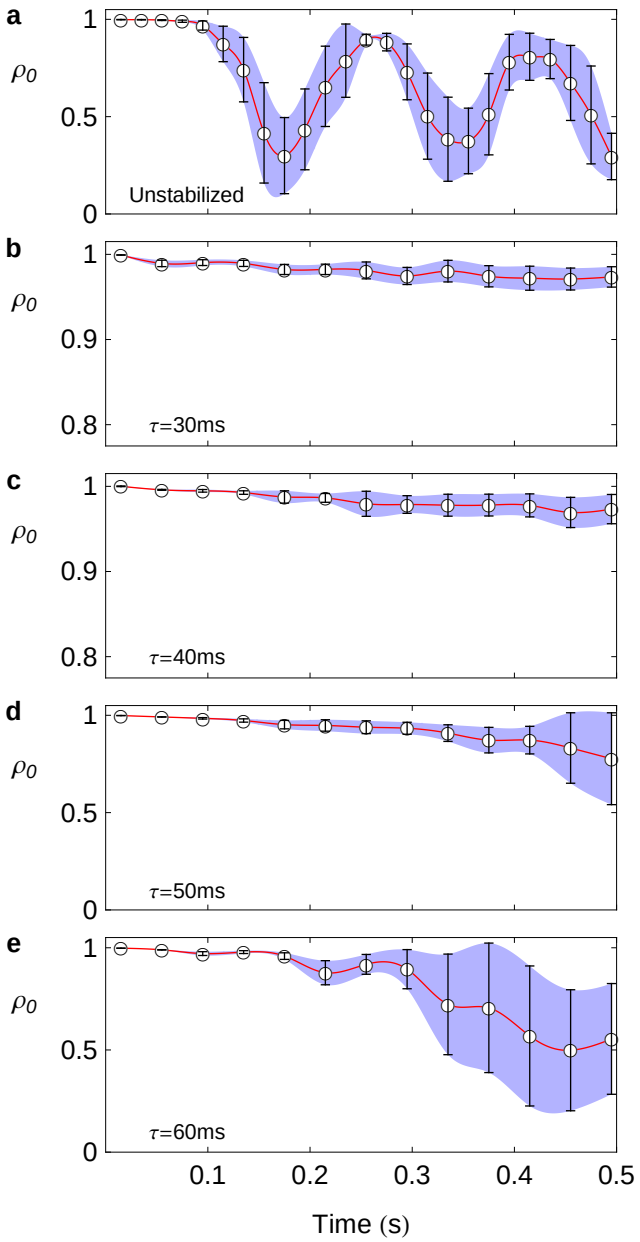

Figure 5.2: Experimental demonstration of dynamic stabilization of spin dynamics. (a) Free (unstabilized) evolution of the spin population, ρ_0, due to quantum spin mixing. (b)-(e) Stabilization of the spin dynamics to the $\rho_0 = 1$ unstable equilibrium using periodic rotations of the spin-nematic quadrature phase with the periods indicated. In each case, microwave pulses are used to rotate the quadrature phase through an amount $\Delta\theta = -\frac{3}{4}\pi$ rad. The open circles correspond to the mean measured value and error bars indicate the measured standard deviation. The red line and blue shaded region are smoothed interpolations to guide the eye. Note the reduced vertical scale in (b) and (c).

The spinor dynamics can be stabilized for a timescale comparable to the $1/e$ lifetime of the condensate as shown in Figure 5.3. Because of the effect from periodic microwave pulses, the lifetime of the condensate is reduced to 500 ms from 1.2 s without microwave pulses. We later discovered that the high power microwave pulse is not perfect and leaves some atoms in $F = 2$ which leads to atom loss and a reduced trap lifetime.

The effect of microwave pulse periods on stabilization can be extracted from the effective quadratic Zeeman $q_{\text{eff}} = q + \hbar\Delta\theta/\tau$ and the stability mapping analysis. For a fixed quadrature angle rotation $\Delta\theta$, the short period pulses τ tend to create effective quadratic Zeeman in the region $q > 2|c|$ and $q < 0$, a robust stabilized region. For longer pulse periods, the system can still be stabilized but for a very narrow range of values of quadrature phase shifts (Figure 5.5). Hence, stabilization is more robust for short pulse periods than for long pulse periods.

5.1.3 Transverse Magnetization

Another observable of stabilization is the transverse magnetization noise $\Delta S_\perp$ which is bounded for stabilized dynamics. During one microwave pulse cycle, the fluctuation of transverse magnetization $S_\perp$ increases and decreases because the condensate undergoes a squeezing-unsqueezing loop in the spin-nematic space $S_\perp Q_\perp$. To measure $S_\perp$, a $\frac{\pi}{2}$ RF pulse is applied to rotate $S_\perp$ into S_z before the trap is off. The $\frac{\pi}{2}$ RF pulse completely transfers atoms in $|f = 1, m_f = 0\rangle$ into $|f = 1, m_f = \pm 1\rangle$.

The fluctuation dynamics of $S_\perp$ is demonstrated in Figure 5.4. For an unstabilized system (microwave pulses off), the fluctuation grows exponentially. The fluctuation reaches the first local maximum about $t = 190$ ms, corresponding the moment of maximum spin mixing (Figure 5.2a). The fluctuation of transverse magnetization then undergoes oscillating (simulation in Figure 5.4 right). For a stabilized condensate, the fluctuation increases until the first microwave pulse comes in and unsqueezes

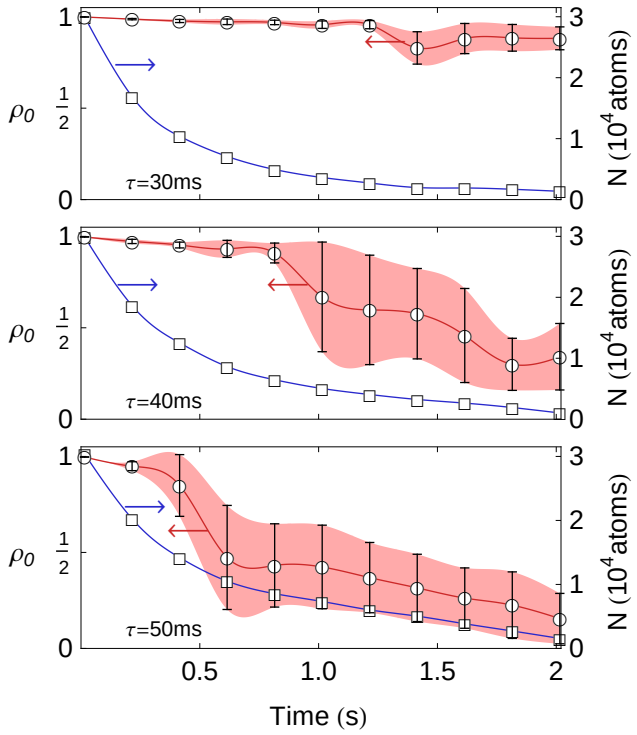

Figure 5.3: Long time stabilization dynamics of the BEC condensate. The fractional population, ρ_0, (red, left) is compared to the total population of the condensate (blue, right). The evolution of the condensate is stabilized for periods much longer than the condensate lifetime of ~ 500 ms.

the condensate. The fluctuation decreases as a result, then increases again until the second microwave pulse, and so on. The experimental results (Figure 5.4 left) show the expected periodic evolution of the fluctuation with a significant reduction of fluctuation compared to unstabilized fluctuation. However the experimental fluctuations are higher than the prediction from simulation. Probably the atom loss induced by microwave pulses and some early quantum spin mixing play a role for this discrepancy.

5.1.4 Stability Diagram

Previously, we stabilized the system with a fixed quadrature phase shift $\Delta\theta$ (experimental angle between manifolds of separatrices). In fact, the condensate can be stabilized with the different quadrature phase shifts and pulse periods $(\Delta\theta, \tau)$. To

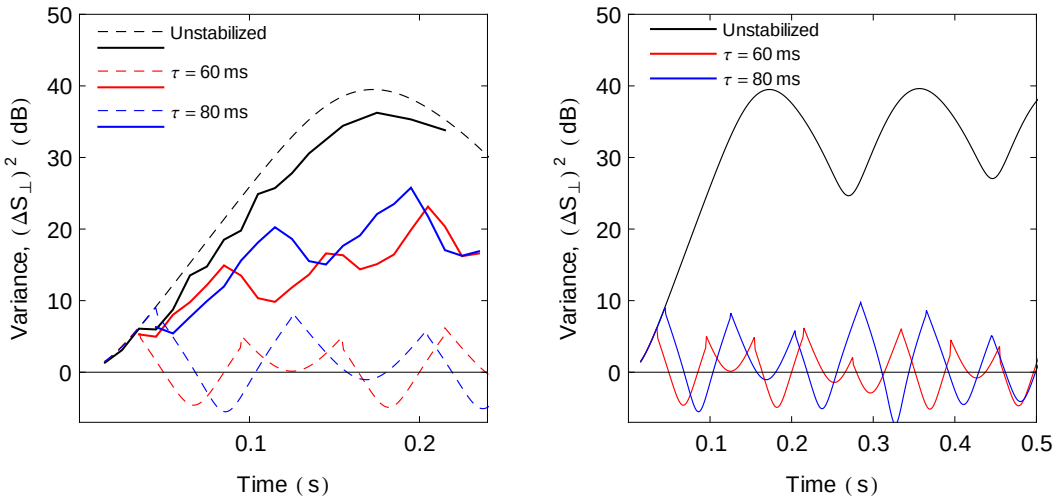

Figure 5.4: Variance transverse magnetization. (left) The fluctuations of the transverse magnetization, $S_\perp$, are measured (solid lines) for both free evolution of the condensate and for the dynamically stabilized dynamics for two different pulse periods. The results are compared to theoretical calculations. The 0 dB line corresponds to the $N^{-1/2}$ standard quantum limit. (right) The simulations of the transverse magnetization noise show the stabilized dynamics and the unstabilize dynamics up to 0.5 s.

study the stability region of the condensate in $(\Delta\theta, \tau)$ diagram, the microwave pulse periods of $[5, 100]$ ms and a quadrature phase shift in $[-\pi, 0]$ are applied to stabilize the condensate. For each combination of $(\Delta\theta, \tau)$, the ρ_0 spinor population is measured after 195 ms of evolution where the maximum spin-mixing occurs (Fig 5.2a). The ρ_0 population determines the stabilization of the system (close to one for stabilized, otherwise unstabilized).

The average of three experimental runs (Figure 5.5) shows the stability diagram of the condensate. For the short period pulses, the condensate is stabilized with a wide range of quadrature angles. For longer period pulses, the stabilized range of quadrature angles get narrower and approach the value close to the angle between manifolds of separatrices $\Delta\theta = \arccos(-1 - \frac{q}{c})$.

The experimental results are fitted to the analytical prediction shown in solid lines. The stability region stays inside the boundary of $\mathrm{Tr}[\mathbf{M}] < 2$ (Eqn 4.4). Fitting

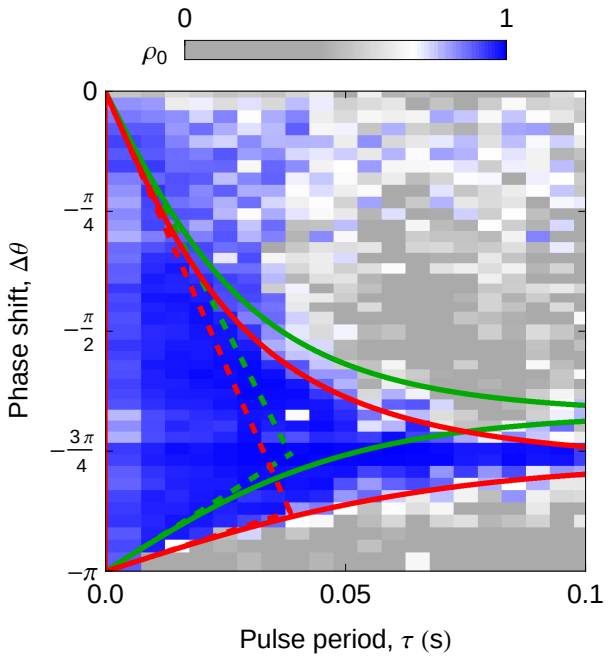

Figure 5.5: Stability diagram. To map the stability region, the mean ρ_0 is measured at the time of the maximum spin mixing for the unstabilized condensate. The solid curves are the envelope of the calculated stability region using linear stability analysis, while the dashed curves use a time-averaged Hamiltonian approach. The green curves use the measured values $B = 210$ mG, $c = -6.5 \times 2\pi$ Hz, and the red curves use $B_{\text{eff}} = 150$ mG, $c = -6.5 \times 2\pi$ Hz.

parameters, the spinor dynamical rate $c = -6.5 \times 2\pi$ Hz is determined by the measurement of coherent oscillation and the magnetic field $B = 220(10)$ mG is measured by an RF spectroscopy. The experimental stability region agrees well with the theoretical envelope; however, there is an offset in the quadrature phase shift for a long period pulse. This discrepancy is larger than the uncertainty in measurements of c and q can account.

5.2 Stabilization with Microwave Pulses Second Attempt

The first attempt using microwave stabilization gives promising results. The spinor population dynamics could be stabilized; however, the dynamics of transverse magnetization noise $\Delta S_\perp$ did not agree very well with the theory. It turns out that the

microwave pulse is not perfect when operating at high power. At high power, the microwave pulse leaves some atoms in $F = 2$ state, which leads to atom loss. This atom loss adds noise to the fluctuation of transverse magnetization $S_\perp$ such that $\Delta S_\perp$ does not goes below the standard quantum limit (SQL) and as low as theoretical prediction (Figure 5.4). Using lower microwave pulses yields a better result in stabilization and reduces the atom loss problem.

5.2.1 Experimental Method

The experimental method is similar to the first attempts. For the microwave pulse, the first attempt uses the high power of microwave with a Rabi rate of ~ 50 μs. The second attempt reduces the power of the microwave pulse by 7 dB which yields a Rabi rate of ~ 170 μs. In this experiment, we use a condensate of 4.5×10^4 atoms initiated in the $|f = 1, m_f =\rangle$ state.

5.2.2 Spinor Population

Similarly, we study the evolution of ρ_0 population to verify the stabilization. The results of stabilization population are shown in Figure 5.6 a [82]. To stabilize the system, the microwave pulses with a fixed period of 60 ms for different quadrature phase shifts are applied to the condensate. Depending on the quadrature phase shift, the spinor population can be perfectly stabilized (A), marginally unstable (B), and unstable (C). Each data point is repeated for 10-15 times. In the case of free evolution (red unstabilized), the population ρ_0 starts at value of 1 and oscillates as quantum spin mixing occurs. In case of perfect stabilization (A), the fractional population ρ_0 almost remain constant around 1. As the system become unstable (B and C) ρ_0 decays away from 1.

To verify that microwave pulse stabilization still maintains the quantum behavior of the system, we perform two other measurements. In the first measurement (Figure 5.7 a), we applied a quadrature phase shift $\Delta\theta = -\pi$ with a period of 60 ms to the

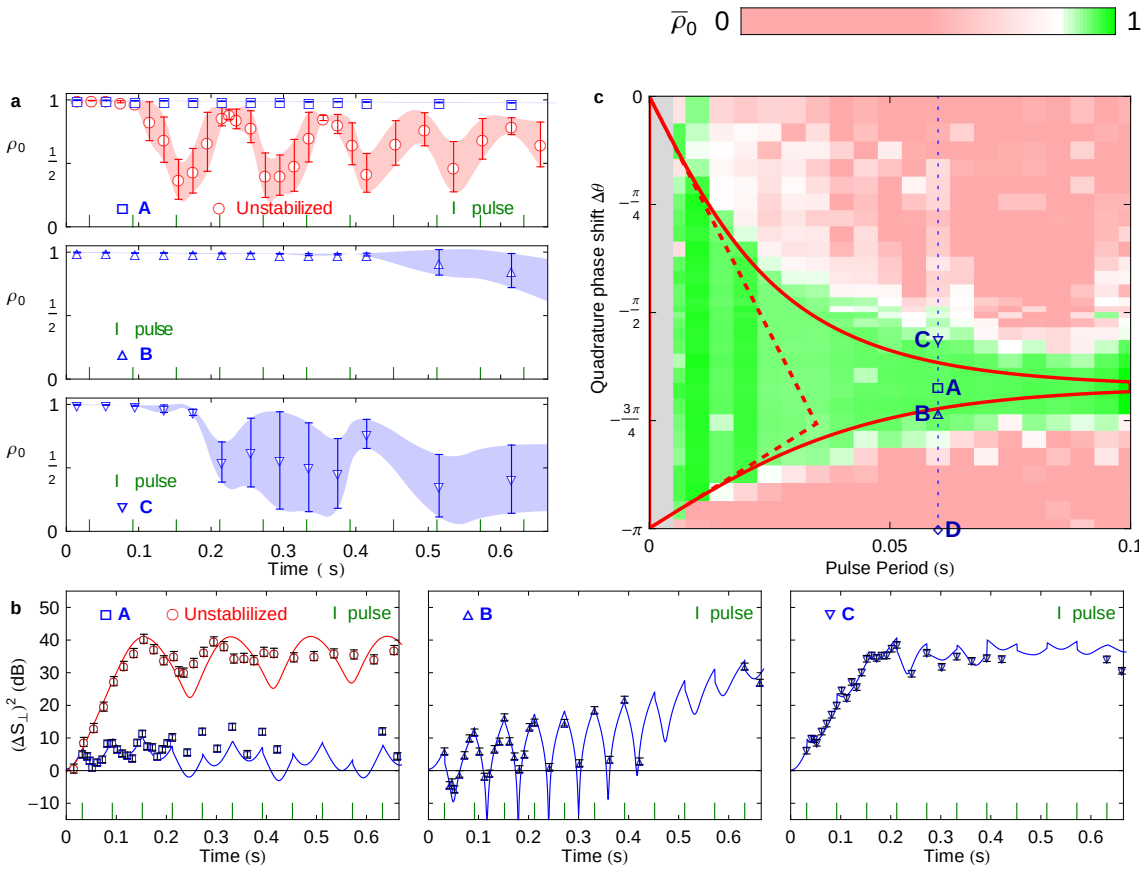

Figure 5.6: Stabilized dynamics and stability mapping. (a) Ideal stabilized population ρ_0 dynamics A(blue square) versus unstabilized (red circle), dynamics near the stability edge where the dynamics eventually destabilize B (blue up triangle), and dynamics outside the stability region C(blue down triangle). The letters A, B, and C correspond to period and quadrature phase shifts $(\tau, \Delta\theta)$ on stability mapping. Pulse timings are shown as green ticks. The shaded region is derived from the standard deviation to guide the eye. (b) Variance of the transverse magnetization $(\Delta S_\perp)^2$ for A versus unstabilized (red circle), B, and C. Theory curve from simulation (solid line) for A $\Delta\theta = -0.65\pi$, B $\Delta\theta = -0.724\pi$, and C $\Delta\theta = -0.56\pi$. (c) Map of the experimental stability region (green) shown with the analytic solution (red solid line) for ρ_0 population after 185 ms of evolution. Also shown is the 'robust' region where the mean effective q is stable (red dashed line). Point D(blue diamond) is at the identity phase shift.

system. The result shows the condensate performs a normal quantum spin mixing. This verifies that microwave pulse does not significantly perturb the quantum characteristic of the system except by rotating the quadrature phase shift. In the second measurement (Figure 5.7 b), we stabilize the system for 572 ms, and then let it freely

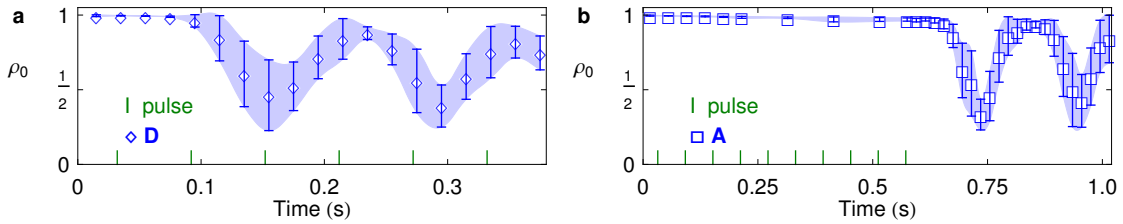

Figure 5.7: Stabilization Coherent. (a) Stabilization under π pulse. (b) Stabilization for 572 ms followed by free evolution. Green ticks show the time where the microwave pulses are on.

evolve. The results show the condensate stabilized as expected when the microwave pulses are on. When the pulses are off, the condensate perform a normal spin mixing. These measurements verify that microwave pulse stabilization still maintains the quantum features of the spinor condensate.

5.2.3 Transverse Magnetization

Solving the microwave pulse problem not only eliminates the atom loss but also gives us an opportunity to access the low noise region (below the SQL) of transverse magnetization. We perform the measurement of $\Delta S_\perp$ for a perfect stabilization (A) compared to unstabilized dynamics (red circle), marginally unstable dynamics (B), and unstable dynamics (C) as shown in Figure 5.6 b [82]. In the case of perfect stabilized (A), the noise $\Delta S_\perp$ grows as the condensate squeezes until the microwave pulse rotates the quadrature phase shift $\Delta\theta$ to unsqueeze the condensate, and the noise decays to the SQL. The process is repeated in each microwave pulse cycle. In the case of marginally unstable dynamics (B), the noise undergoes the squeezing-unsqueezing loops for a while and eventually grows to the limit of 40 dB. For a first few cycles, the noise actually goes below SQL (-5.7 dB). In the case of unstable dynamics (C), the noise exponentially grows similar to the unstabilized case (red circle). The results are fitted to a quantum simulation, and they show good agreement with theory.

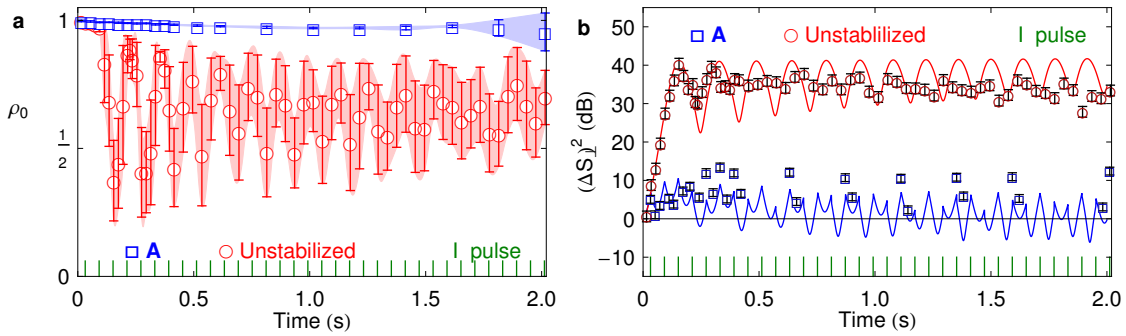

Figure 5.8: Long timescale stabilization by microwave pulses. (a) The stabilization dynamic population ρ_0, plot legend refers to corresponding location in diagram 5.6 c. The shaded regions are derived from the standard deviation to guide the eye. (b) The uncertainty of transverse magnetization $\Delta S_\perp$. Theory curve from simulation (solid line) with spinor dynamical rate $c = -2\pi \times 7.2$ Hz and magnetic field $B = 220$ mG. Green ticks show the time where the microwave pulses are on.

Note that during stabilization dynamics, the condensate always squeezes. However, the measurements of the fluctuations do not fall below the SQL because the principle axes (convergent separatrix) of the squeezing ellipse are never oriented along the measurement axis $S_\perp$ (shown in Figure 4.3).

5.2.4 Long Timescale Stabilization Dynamic

Since the stabilization method is very robust, we tried to stabilize the condensate until we run out of atoms in the BEC. Figure 5.8 shows the condensate stabilized for up to 2 s. A typical trap life time is about 1.4-1.6 s. In Figure 5.8 a, the spinor population $\rho_0 = 1$ for almost 2 s; during this time, the unstabilized condensate undergoes 14 oscillation cycles. Figure 5.8 (b) shows transverse magnetization noise $\Delta S_\perp$ (blue square A) oscillating around SQL up to 2 s. For an unstabilized condensate (red circle) $\Delta S_\perp$ exponential grows up to 40 dB, oscillates around this level for a few cycles and reaches a steady level of 35 dB.

5.2.5 Stability Diagram

The stabilization dynamics depend on the amount of quadrature phase shift $\Delta\theta$ and the pulse period τ. To examine the stability condition, the population ρ_0 is measured at the maximum spin mixing moment (after 185 ms of evolution). The values of ρ_0 determine the stability diagram of the condensate. The results are shown in Figure 5.6 c [82]. Each point on the stability map is the average of 3 runs. For short periods, the condensate can be stabilized with a wide range of quadrature phase shifts. For longer pulse periods, the condensate is stable if the amount of quadrature phase shift is close to the angle between the convergent and divergent separatrix. The results are fitted to the analytical solution from the Eqn 4.4 for the magnetic field of $B = 220$ mG and the spinor dynamical rate $c = -7.2 \times 2\pi$ Hz. With the atom loss problem solved, the result shows very good agreement with theory. The experiment seems to cover a little wider area than the theory because after 185 ms of evolution, population ρ_0 near the edge of stability does not have enough time to decay.

5.3 Stabilization with Magnetic Field Pulses

As an alternative method to using microwave rotations, we have effected quadrature phase rotations with a magnetic field pulse. The magnetic field shifts quadrature phase shift by [51]

$$\Delta\theta = -q_Z B^2 \Delta t \tag{5.1}$$

where $\Delta\theta$ is the quadrature phase shift, $q_Z = 71.6\text{Hz/G}^2$ is the quadratic Zeeman constant, and Δt is the magnetic field pulse length.

5.3.1 Experimental Method

In general, the stabilization concept for a magnetic field pulse is similar to a microwave pulse. Instead of using the microwave pulses, we apply magnetic field pulses. The stabilization concept is described in Figure 5.9. The magnetic field pulses of period

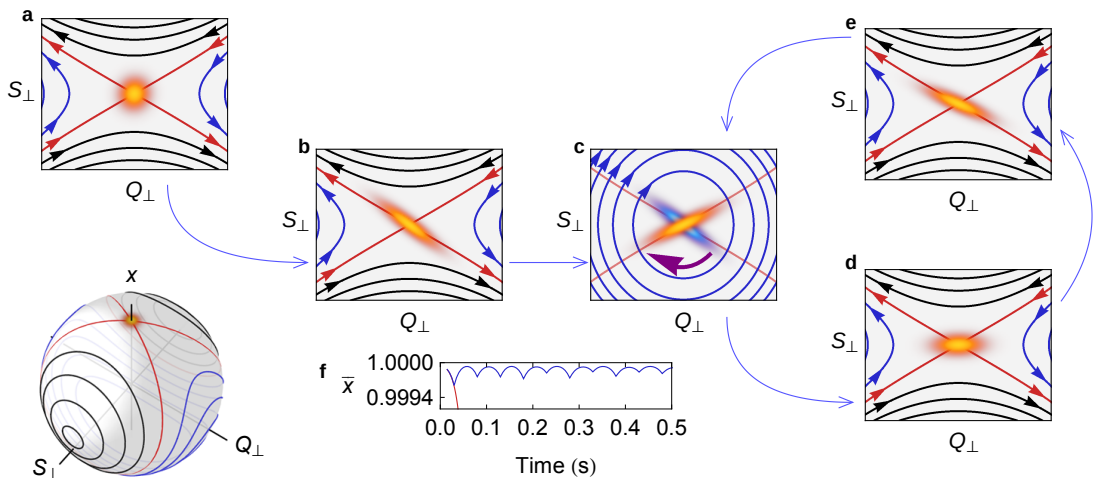

Figure 5.9: Illustration of the dynamic stabilization method. (a) The condensate is initialized at the pole of the spin-nematic Bloch sphere, $x = 1, S_\perp = Q_\perp = 0$. The condensate has Heisenberg-limited uncertainties in $S_\perp$ and $Q_\perp$. (b) Initial free evolution of the condensate produces spin-nematic squeezing along the diverging manifold of the separatrix. (c) The quantum state of the condensate is quickly rotated to the converging manifold of the separatrix using a magnetic field pulse (low field separatrix shown in red). (d) Subsequent free evolution unsqueezes the condensate, returning it close to the original state. (e) Continued free evolution again generates spin-nematic squeezing. (f) Long term stabilization is achieved by repeating the (c,d,e) sequence (blue line) whereas the unstabilized condensate rapidly evolves away (red line).

τ rotates the condensate quadrature angle $\Delta\theta$ away from its divergent separatrix to maintain the condensate in the squeezing-unsqueezing loop.

An experiment is performed in a condensate of $N = 4.5 \times 10^4$ atoms initiated in the $|f = 1, m_f = 0\rangle$ state at high magnetic field of 2 G. To trigger the dynamics, the magnetic field is quenched below the quantum critical point to 220 mG. A sequence of magnetic field pulses of period τ is applied to stabilize the system. Finally, the spin populations of the condensate are measured. This is executed by releasing the trap and allowing the atoms to freely expand in a Stern-Gerlach magnetic field gradient to separate the m_f spin components. To measure the transverse magnetization $S_\perp$, an RF $\pi/2$ pulse is applied to rotate $S_\perp \rightarrow S_z$ before imaging. The experimental

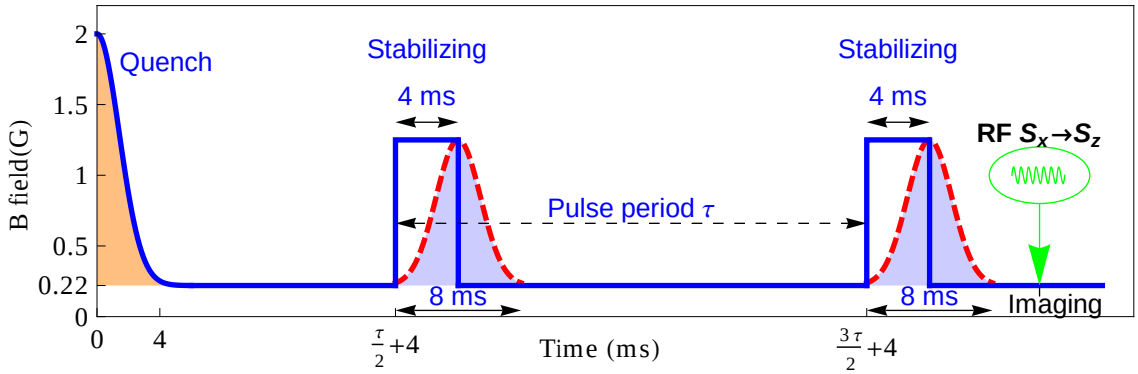

Figure 5.10: Magnetic field pulse stabilization experimental sequences. To initiate the dynamics, the magnetic field is quenched from 2 G to 220 mG. Each magnetic field pulse is separate by a period τ. The imaging setup capture the spinor population or the transverse magnetization by applied an RF to rotate $S_x \rightarrow S_z$.

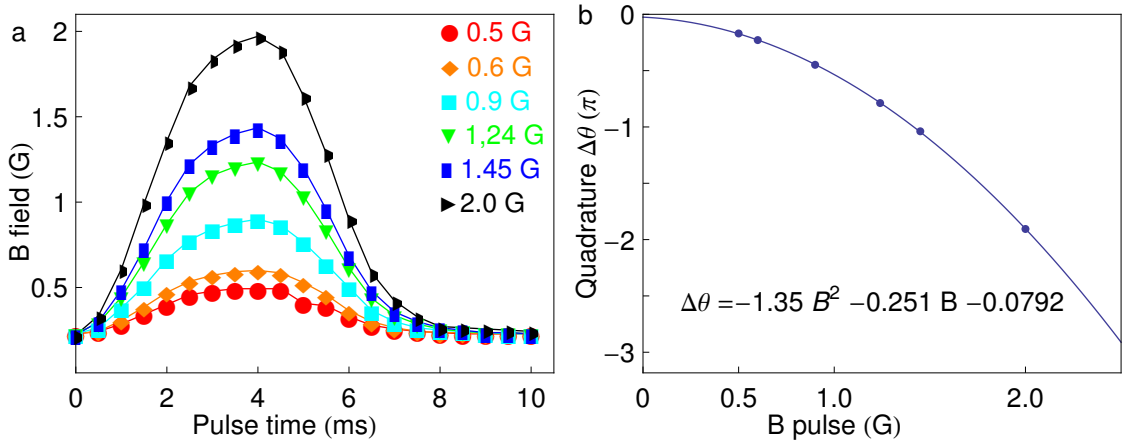

Figure 5.11: Magnetic field profile of 4 ms pulse length. (a) The pulse profile for different magnetic field strength. (b) The quadrature phase shift by the magnetic field fitted to a quadratic function.

sequence is shown in Figure 5.10.

5.3.1.1 Magnetic field phase shift

Because a magnetic field pulse needs a finite time to rise and decay, we tried to perform the experiment with the shortest pulse length as possible. During a short pulse length, we assume the dynamics are negligible, and the magnetic field pulse only rotates the quadrature phase shift. The experiments are performed with a magnetic

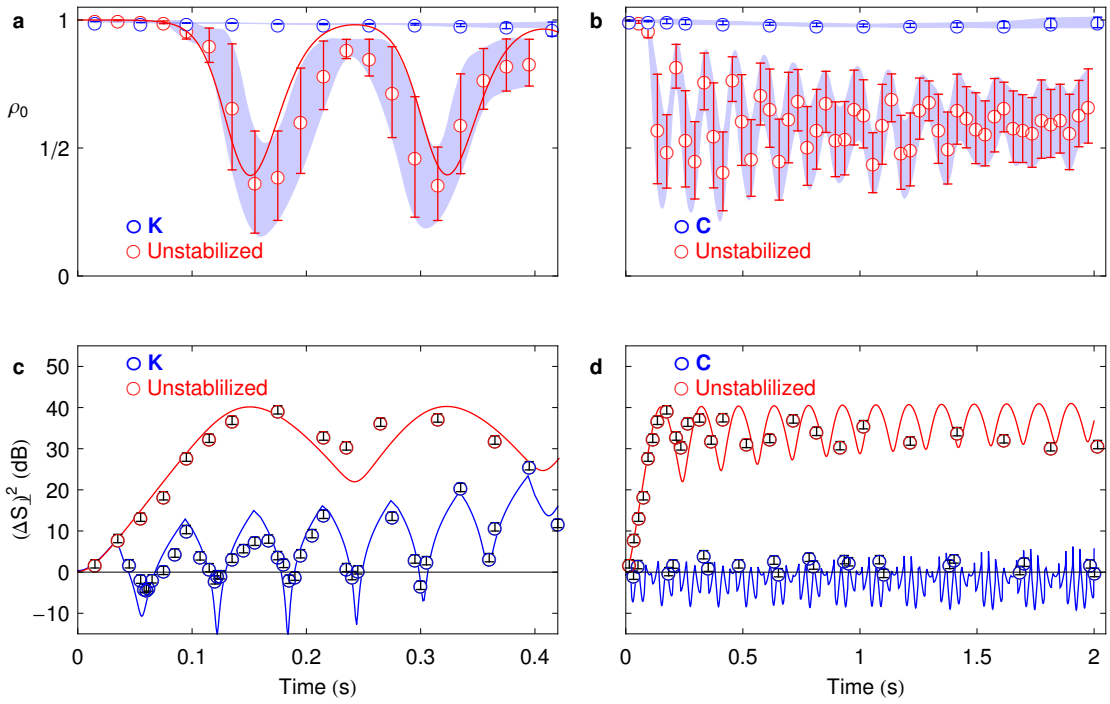

Figure 5.12: Stabilized dynamics vs. unstabilized dynamics (normal spin mixing). (a) and (c) The short timescale, and (b) and (d) long timescale of spinor dynamics and the uncertainty in quadrature $\Delta S_\perp$. The legends ∘ C and ∘ K refer to locations on the stability map in Fig 5.15. Data are fitted to simulations (solid line). Legend o K with magnetic pulse $B_{pulse} = 1.315$ G fitted with $B_{pulse} = 1.26$ G, and legend o C with magnetic pulse $B_{pulse} = 1.29$ G fitted to $B_{pulse} = 1.29$ G. All are fitted with spinor dynamical rate c = -8 $\times 2\pi$ Hz, and background magnetic field B = 0.22 G.

pulse length of 4 ms. The magnetic pulse profiles are shown in Figure 5.11 a. The quadrature phase shift is calculated by numerically integrating $\Delta\theta = -\int q_Z B^2 dt$ for a given pulse as shown in Figure 5.11 b. The conversion from magnetic field to quadrature phase shift is given by fitting the experimental data to a quadratic function, $\Delta\theta = -1.35B^2 - 0.251B - 0.0792$.

5.3.2 Stabilization Dynamic

The stabilization dynamics can be discussed in terms of ρ_0 and $\Delta S_\perp$ evolutions. The experimental magnetic stabilization is shown in Figure 5.12. To show the stabilization effect, we compare the stabilized dynamics with the free evolutions (unstabilized). We

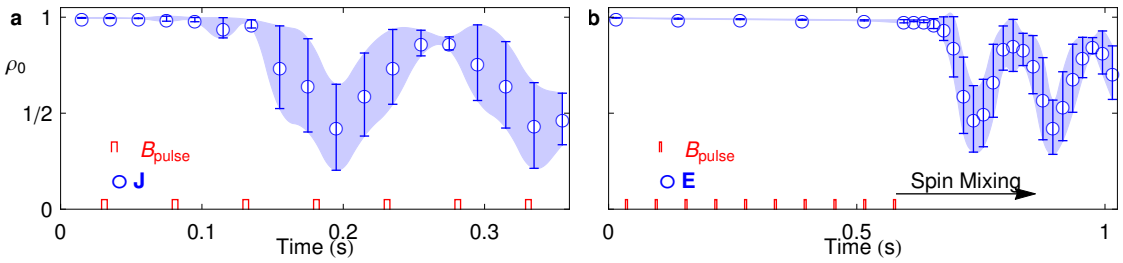

Figure 5.13: (a) Stabilization under π pulse, (b) 580 ms of stabilization then free evolution, (c) dynamics of min/max quadrature variance, and (d) quadrature variance (at 60 ms) vs. magnetic field pulse (at 34 ms). All are fitted with c = -8 $\times 2\pi$ Hz (solid line)

demonstrate the ability to stabilize dynamics in a short timescale (K) and in a long timescale (C).

The stabilized population ρ_0 (a, b) stays constantly at value of 1, and we can stabilize the dynamics up to 2 s. The free evolutions (unstabilized) go through many of the large amplitude oscillations as the result of quantum spin mixing.

Figure 5.12 (c, d) shows the measurement of the evolution of the transverse spin fluctuations. With no stabilization, the fluctuations $\Delta S_\perp$ grow exponentially and eventually oscillates. When the condensate is stabilized, the simulations (solid line) show that the fluctuation $S_\perp$ increases and decreases during the squeezing-unsqueezing loop as a result of the stabilization. In short timescale up to 0.4 s, the data show the expected periodic evolution of the fluctuations and a significant reduction of the fluctuations compared with the unstabilized condensate, and the noise even goes below the standard quantum limit (SQL) noise. The $\Delta S_\perp$ data stay at the SQL level up to 2 s which agree with the theory. However, the overall level of the measured fluctuations are higher than predicted, and minimum $\Delta S_\perp$ is around -4 dB higher comparing to -10 dB from experiment.

In Figure 5.14, we show the results of the stabilization and evolution of transverse

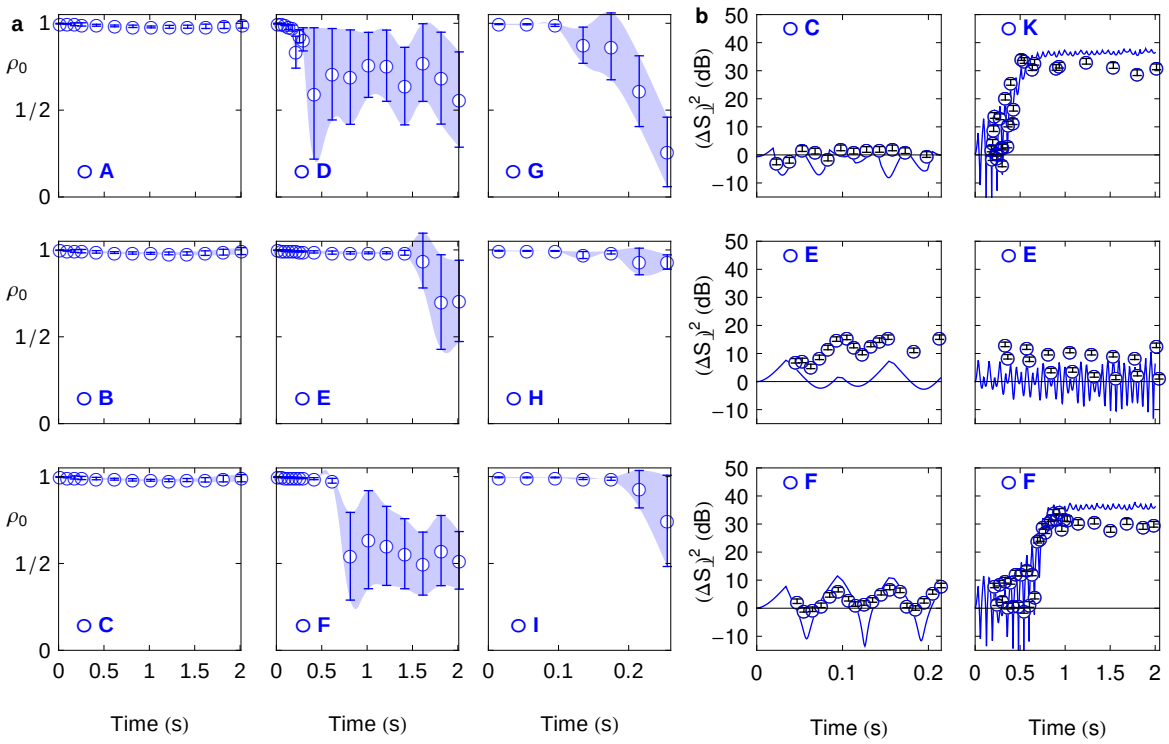

Figure 5.14: Stabilization by magnetic field pulses. The legend ∘ letters in each plot refer to locations on the stability map in Figure 5.15. (a) The stabilization dynamic population ρ_0, plot legend refers to corresponding location in stability diagram Figure 5.15. The shaded region are derived from standard deviation to guide the eyes. (b) The uncertainty of transverse magnetization $\Delta S_\perp$. Legend o C with magnetic pulse $B_{pulse} = 1.29$ G fitted to $B_{pulse} = 1.29$ G, legend o E with magnetic pulse $B_{pulse} = 1.24$ G fitted with $B_{pulse} = 1.22$ G, legend o F with magnetic pulse $B_{pulse} = 1.29$ G fitted with $B_{pulse} = 1.255$ G. All are fitted to spinor dynamical rate c = -8 $\times 2\pi$ Hz, and background magnetic field B = 0.22 G.

spin fluctuations for pulse periods ranging from 30–90 ms for different quadrature rotation angles. For a short pulse periods ($\tau \sim 30$ ms), the condensate can be stabilized with a wide range of quadrature rotations. For the longer pulse periods τ, the stable range of quadrature rotations is narrower. We show that the quantum spin dynamics can be stabilized, and $\Delta S_\perp$ stays at the SQL level for a time scale comparable and even longer than the $1/e$ lifetime of the condensate. The lifetime of the stabilized condensate is ∼1.3–1.6 s while the lifetime of the unstabilized condensate is 1.8 s.

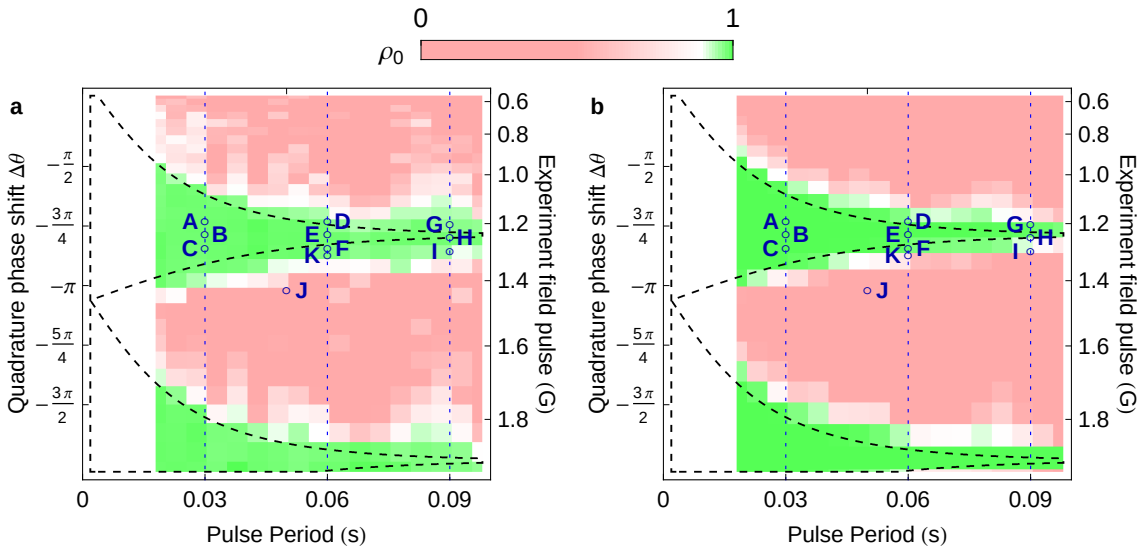

Figure 5.15: Stability mapping for ρ_0 population after 165 ms of evolution. Figure a shows experimental stability region (green) fitted to the analytic solution (dashed line). Figure b shows simulation of the stability region (green) fitted to the analytic solution. Data are fitted to the spinor dynamical rate $c = -8.0 \times 2\pi$ Hz and B = 0.22 G. Quadrature phase shifts $\Delta\theta = -\int_0^{\Delta T} qB_{pulse}^2 dt$.

5.3.2.1 Preservation of Quantum Coherent

We have performed two additional checks 5.13 (a, b) to verify that the magnetic field stabilization maintains the coherent dynamics of the system. In the first, we have studied the evolution of the condensate under periodic pulses with $\Delta\theta = -\pi$ (the periodicity of the phase space) and verified that the condensate undergoes normal spin mixing (a). In the second, we have turned the stabilization pulses off after 580 ms and verified that the system again undergoes normal spin mixing (b).

5.3.3 Determining the Stability Region

We now turn to an investigation of the stability diagram for the condensate. Although it is conceptually simplest to understand the stabilization in terms of periodic evolutions along manifolds of the separatrix of the phase space; the condensate can be stabilized with a range of phase shifts and periods $(\Delta\theta, \tau)$. The range of stability

is measured for the quadrature phase rotations $\Delta\theta \in [-\pi, 0]$ and pulse period τ from 20 ms to 100 ms. For each combination of $(\Delta\theta, \tau)$, the spinor population is measured after 165 ms of evolution, where the unstabilized condensate shows the maximum spin mixing (see Figure 5.12 a). The results of measurement are shown in Figure 5.15, where each measurement point is the average of three experimental runs. By scanning through quadrature phase shift (magnetic field pulse), we are able to observe multiple stability regions. For shorter period pulses, the condensate is stabilized with a wide range of quadrature phase shifts. For long period microwave pulses, the range of quadrature phase shift capable of stabilizing the dynamics shrinks and reaches an asymptotic value close to the angle between the separatrices, $\Delta\theta = \cos^{-1}(-1 - \frac{q}{c})$. The results are compared with a theoretical stability analysis shown in dashed lines ($|\mathrm{Tr}[\mathbf{M}]| < 2$ in Eqn 4.5) and the simulation in Figure 5.15 b. The dashed lines show the stability envelope using the spinor dynamical rate $c = -2\pi \times 8.0$ Hz and the magnetic field $B = 220(10)$ mG that determines the quadratic Zeeman effect $q = 2\pi \times 71.6 \times B^2$ Hz/G^2. The measured stability region is in a good qualitative agreement with the theoretical envelope.

CHAPTER 6

PARAMETRIC EXCITATION

In this chapter, we demonstrate the experimental parametric excitation in a spin-1 Bose-Einstein condensate quantum many-body system and present a theoretical description from semi-classical and quantum perspectives. The quadratic Zeeman energy distinguishes the dynamics of spin-1 from spin-1/2 systems. In spin-1/2 system, the quadratic Zeeman energy shifts are the same; the spin precession is solely due to the linear Zeeman effect. In a spin-1 system, the quadratic Zeeman shift is different for $m_f = 0$ and $m_f = \pm 1$; the spin vector not only precesses due to the linear Zeeman energy but also its magnitude oscillates due to the quadratic Zeeman energy, the same as a spin-1 nucleus in NMR [141]. We will first describe the system using a semi-classical model of the spin-nematic phase space which is in line with the standard classical understanding of parametric excitation. Then, we will present a quantum interpretation of the same dynamics where the excitation drives transitions between the many-body Fock states of the quantum system. This dual picture of this system demonstrates a correspondence between the quantum and the classical parametrically excited oscillator. Moreover, the mean-field dynamics of the spin-1 system exhibits dynamics similar to the Bose-Hubbard double-well condensate. In the double-well system, Shapiro-like effects have been suggested by modulating the tunneling constant of a Bose Josephson Junction [123]. By modulating the quadratic Zeeman energy, we are able to observe similar dynamics with the integer divisor frequencies of Shapiro-like resonances.

6.1 High Magnetic Field Coherent Dynamics

The experiment is carried out in a small condensate within the single mode approximation, and the Hamiltonian is given by [84, 56]

$$\mathcal{H} = \lambda \hat{S}^2 + p\hat{S}_z + \frac{q}{2}\hat{Q}_{zz} \tag{6.1}$$

where $\hat{S}^2 = \hat{S}_x^2 + \hat{S}_y^2 + \hat{S}_z^2$ is the total spin operator with $\hat{S}_z$ its projection along B, $\hat{Q}_{zz}$ is the quadrupole moment of the spin-1 or quadrupole tensor, $\lambda \propto a_2 - a_0$ is the spin interaction strength integrated over the condensate, $p = p_Z B$ is the linear Zeeman energy, and $q = q_Z B^2$ is the quadratic Zeeman energy. The linear and quadratic Zeeman constants are $p_Z \approx 700$ Hz/mG and $q_Z \approx 71.6$ Hz/G^2.

We study the dynamics at a magnetic field regime well above quantum critical $q > 2|c|$. The spin-nematic phase space for $q/|c| \sim 10$ is shown in Figure 6.1 a. The experimental coherent oscillations for different initial ρ_0 are shown in Figure 6.1 b. The oscillation amplitudes and frequencies explicitly depend on the initial ρ_0. The period is approximately about 7 ms and increases from $2(q + c)$ to $2(q - c)$ as ρ_0 goes from 1 to 0. The maximum oscillating amplitude $\Delta\rho_0 = 2\%$ for $\rho_0 = 0.5$, and $\Delta\rho_0 = 0$ for $\rho_0 \to 0$ or 1.

6.2 Parametric Excitation Concept

The experiment is performed with a condensate of $N = 4 \times 10^4$ atoms initiated in the $|f = 1, m_f = 0\rangle$ state with a high magnetic field $B = 2$ G. We lower the magnetic field down to 1 G ($q/|c| \sim 10$) for the parametric excitation. The population ρ_0 or transverse magnetization $S_\perp$ are measured after a certain time. The experimental sequence is shown in Figure 6.2. Parametric excitation is performed by modulating the quadratic Zeeman term in the Hamiltonian

$$q(t) = q_0 + q_m \sin(2\pi f_m t - \phi_0) H[t - \phi_0/2\pi f_m] \tag{6.2}$$

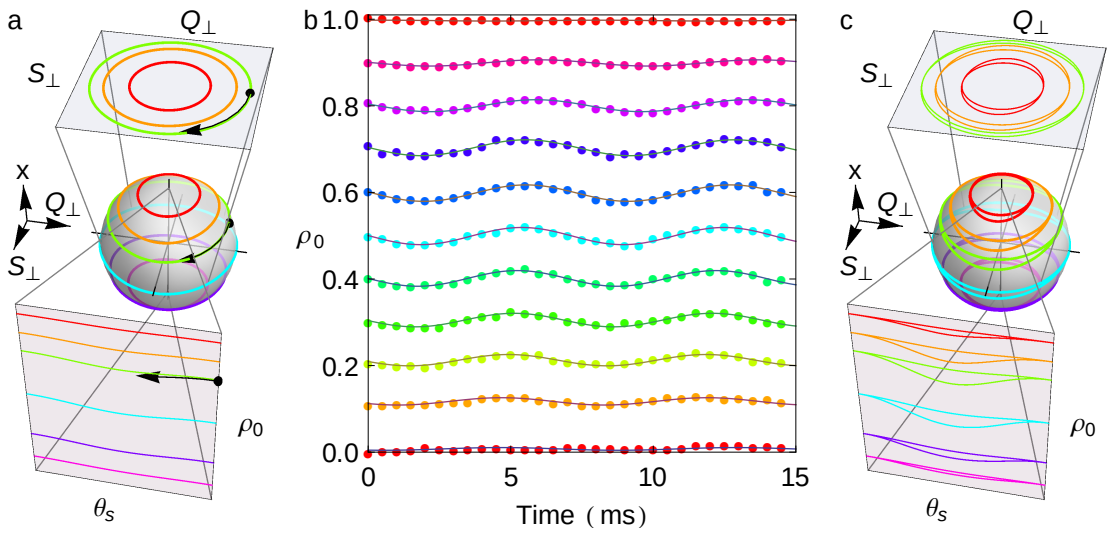

Figure 6.1: Illustration of phase space and coherent oscillation. (a) The phase space at $B_0 = 1$ (G), the sphere represents $S_\perp Q_\perp x$ space. The spin-nematic space is shown at the top, and the spinor phase space is shown at the bottom. The black arrow presents the trail of dynamics along energy contour for an initial ρ_0. (b) Coherent oscillation at B = 1 (G) for an given initial population ρ_0 prepared by RF pulse. Coherent oscillation data (colored dots) are compare to simulation (line) for spinor dynamical rate $c = -7.2 \times 2\pi$ Hz. (c) The phase space of the modulated Zeeman energy, the contours are vibrating as a result of parametric excitation.

where $q_0 = q_Z B_0^2$, $q_m = q_Z B_m^2$, B_m is the modulation magnetic field, f_m is the modulation frequency, and $H[t - \phi_0/2\pi f_m]$ is the Heaviside step function with the initial modulation phase ϕ_0. Since the magnetic field takes about 2 ms to reach the desired value, for a typical $f_m \sim 140$ Hz (the period is 7 ms), the actual modulation magnetic field is lower than the set value and estimated to be 0.85 B_m. Also, the hysteresis and imperfectness of the magnetic field pulse can alter the amplitude of the magnetic field by about 25 mG. The modulation of $q(t)$ modulates the spinor energy contours as shown in Figure 6.1 c. As the condensate evolves along the vibrating energy contours, it can cross energy contours depending on the modulation frequency and the initial modulation phase.

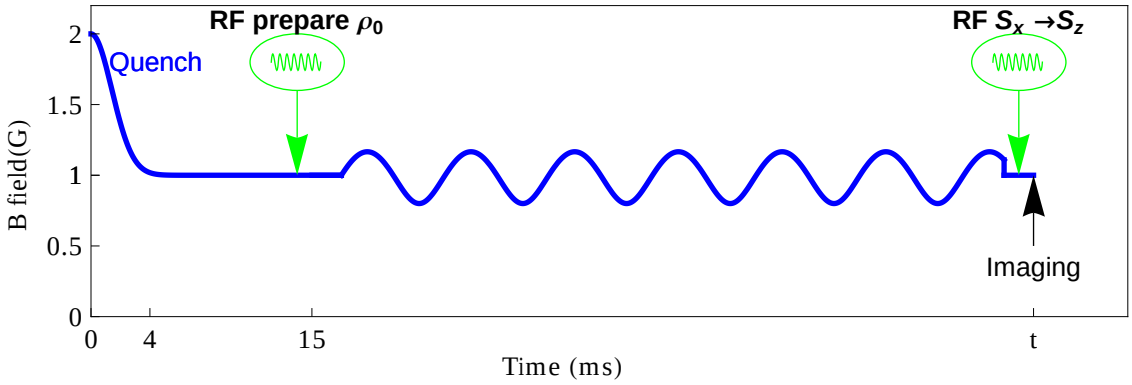

Figure 6.2: Parametric excitation experimental sequences. To initiate the dynamics, the magnetic field is quenched from 2 G to 1 G, and then the magnetic field is modulated sinusoidally. The imaging setup capture the spinor population ρ_0 or the transverse magnetization by applying an RF pulse to rotate $S_x \rightarrow S_z$.

What are our observables? When the condensate crosses between energy contours, the population ρ_0 changes as a result. The effect of parametric excitation can be determined by measuring the population ρ_0.

6.3 Observation of Parametric Excitation

We first demonstrate the effect of parametric excitation on the coherent oscillation previously shown in Figure 6.1 b. We prepare an initial ρ_0 by an RF pulse with an initial phase $\phi_0 = \pi$, and scan $f_m \in [100,\ 180]$ Hz. The population ρ_0 is measured 40 ms after an RF pulse. The plot of ρ_0 vs. f_m is shown in 6.3 a. The hue colors of initial values of $\rho_0 \in [0, 1]$ are the same scale as the coherent oscillation Figure 6.1 c. The population ρ_0 increases or decreases depending on f_m; moreover, the amount of change is larger than the coherent oscillation. This indicates parametric excitation of the spinor population. The experimental data are compared to the simulation shown in solid lines. The square markers indicate the approximate positions of the resonant frequencies. The resonance frequency increases as ρ_0 goes from $1 \rightarrow 0$. The data show a good agreement to the simulation.

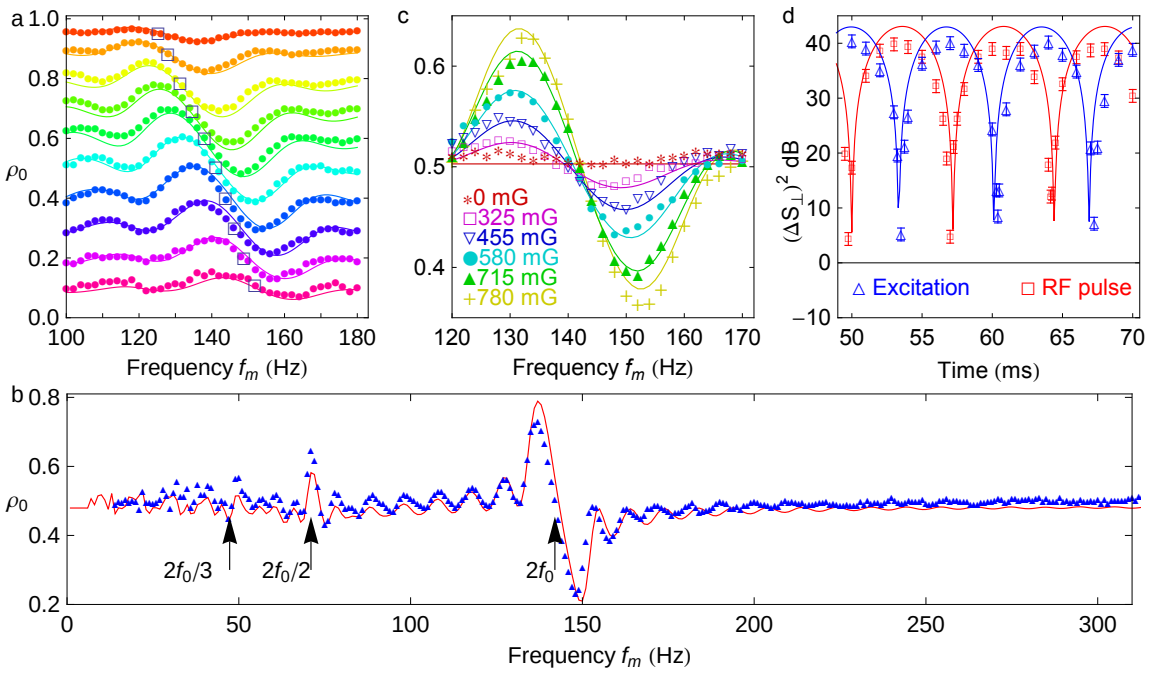

Figure 6.3: Coherent oscillation and parametric excitation. (a) Population ρ_0 after 40 ms of parametric excitation for different initial ρ_0. Quadratic Zeeman is modulated with an initial phase of $\phi_0 = \pi$ after RF pulse, for $B_0 = 1$ G, $B_m = 0.715$ G. (b) Resonance frequency spectrum for initial $\rho_0 = 0.5$ after 100 ms of parametric excitation with an initial phase $\phi_0 = \pi$, $B_0 = 1$ G, and $B_m = 0.715$ G. (c) Population ρ_0 after 40 ms of parametric excitation for initial $\rho_0 = 0.5$ for different modulation amplitudes B_m with an initial phase $\phi_0 = \pi$ and $B_0 = 1$ G. (d) Red square shows the evolution of $(\Delta S_\perp)^2$ for initial $\rho_0 = 0.5$ prepared by RF pulse. Blue up triangle shows evolution of $(\Delta S_\perp)^2$ for initial $\rho_0 = 0.5$ prepared by 40 ms of parametric excitation (bring ρ_0 from 0.59 to 0.5) with $B_0 = 1$ G and $B_m = 0.744$ G.

The excitation frequency spectrum is one of the signatures of parametric excitation. To study the excitation spectrum, we prepare the initial state $\rho_0 = 0.5$ by an RF pulse with an initial phase $\phi_0 = \pi$, and vary $f_m \in [14,\ 314]$ Hz. The population ρ_0 is measured 100 ms after an initial RF pulse. The excitation spectrum is shown in Figure 6.3 b. The data are compared to simulations. The strongest peak on the spectrum corresponds to twice the natural frequency peak $2f_0/1 = 142$ Hz. Two other smaller peaks near $2f_0/2$ and $2f_0/3$ also stand out. Other resonant frequencies are too small to be detected for these excitation parameters.

Even though the modulation amplitude q_m ($\propto B_m^2$) does not give rise to parametric

excitation, increasing q_m can excite spinor population up or down faster. We prepare an initial $\rho_0 = 0.5$ with an initial phase $\phi_0 = \pi$, and vary $f_m \in [120,\ 170]$ Hz. The population ρ_0 is measured at 40 ms after an initial RF pulse for different q_m (B_m). For the same modulation frequency, a larger modulation amplitude changes the population amplitude faster as shown in Figure 6.3 (c). The experimental data are compared to the simulations. Since the magnetic field takes about 2 ms to reach the setting value, for a typical $f_m \sim 140$ Hz (the period of 7 ms), the actual modulation magnetic field is lower than the set value and estimated to be 0.85 B_m. The simulation uses the modulation magnetic field of 0.85 B_m to compare to the data.

Since parametric modulation excites the condensate across energy contours, the coherent spinor dynamics should still be preserved. To verify this, we apply 40 ms of modulation to excite the initial population $\rho_0 = 0.59 \rightarrow 0.5$. To observe the coherent dynamics, we can either measure the ρ_0 dynamics (as seen in Figure 6.1 b) or the transverse magnetization $S_\perp$. In the spin-nematic sphere $S_\perp Q_\perp x$, the measurement of ρ_0 corresponds to the projection of oscillation onto the x axis which yields a smaller signal than projecting onto $S_\perp$. The distribution of quantum states in $S_\perp Q_\perp$, precessing about x due to quadratic Zeeman, produces a coherent oscillation of magnetization noise $\Delta S_\perp$ as shown in Figure 6.3 d. Comparing to the normal coherent oscillation of initial $\rho_0 = 0.5$ prepared by an RF pulse, the oscillation amplitude and period are similar and indicate both methods bringing the condensate to a similar energy contour. The difference in the phase is due to the hysteresis of magnetic field modulation during parametric excitation (15 mG up compared to no modulation).

6.4 Excitation $f_m\phi_0$ Phase Space for ρ_0

The parametric excitation explicitly depends on the modulation frequency f_m and the initial phase ϕ_0. Understanding the effect of $f_m\phi_0$ on the parametric excitation is necessary to control the quantum states of condensate. To study this effect,

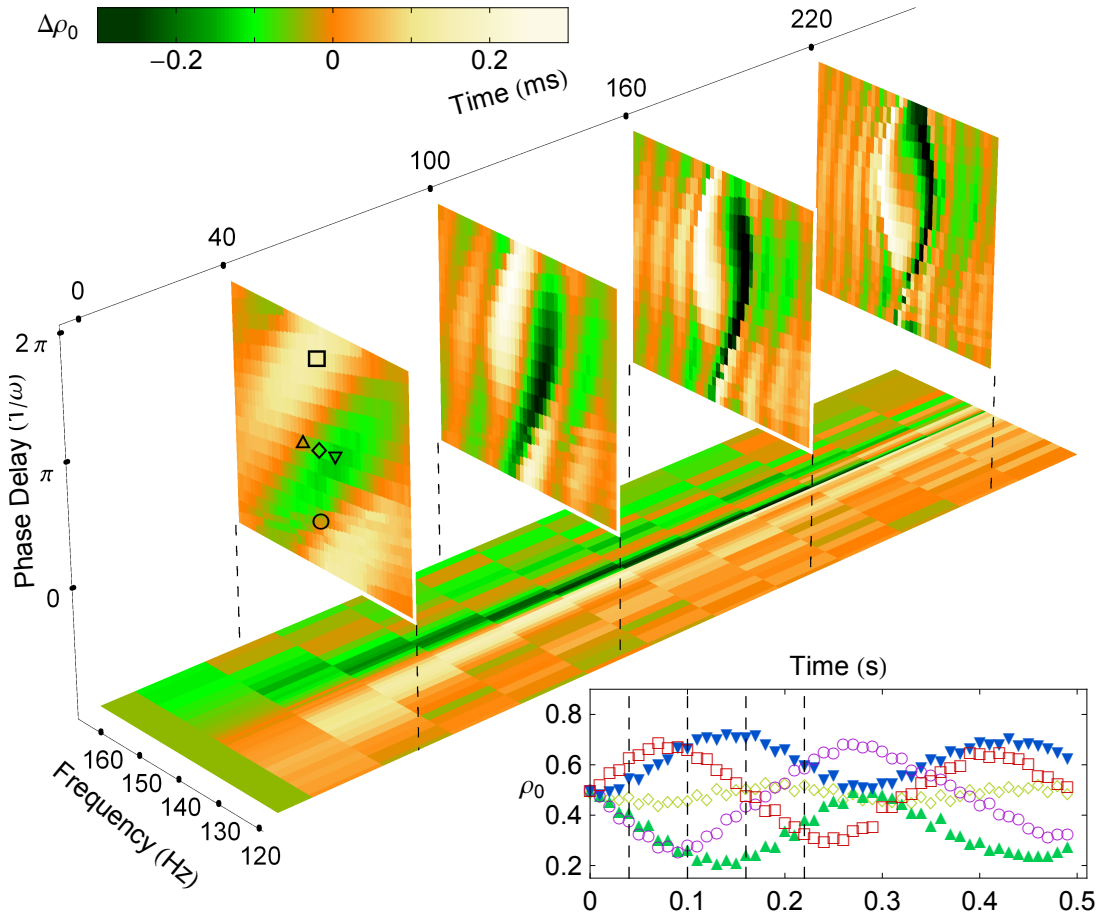

Figure 6.4: Excitation $f_m\phi_0$ phase space for ρ_0. An initial population $\rho_0 \sim 0.5$ prepared with an RF pulse. Magnetic field is modulated by $q = q_0 + q_m \sin(2\pi f_m t - \phi_0)$, for $B_0 = 1$ G, $B_m = 0.715$ G. The four parallel slices show the map of ρ_0 after 40 ms, 100 ms, 160 ms, and 220 ms of parametric excitation. The horizontal slice shows the dynamics of ρ_0 for the initial phase $\phi_0 = 0$. The inset shows the dynamics of ρ_0 for different points on the $f_m\phi_0$ map. The labels of the plot correspond to the markers on the map.

we prepare an initial population $\rho_0(0) = 0.5$ by an RF pulse, vary the modulation frequency in $f_m \in [120, 165]$ (Hz), and vary the initial phase $\phi_0 \in [0, 2\pi]$. The population $\Delta\rho_0 = \rho_0 - \rho_0(0)$ is measured after each period of excitation 40 ms, 100 ms, 160 ms, and 220 ms as shown in Figure 6.4 (four parallel slides). The white (black) regions represent the positive (negative) change in population $\Delta\rho_0$. These two regions evolve and spiral to form a yin-yang like shape. At the center of the yin-yang $(f_m, \phi_0) = (2f_0, \pi)$ where $2f_0 \approx 143$ Hz, the dynamic $\Delta\rho_0$ unchanges and the phase

space is anti-symmetric about it. The inset Figure 6.4 shows the dynamics of different points about $(2f_0, \pi)$, after short modulation $(\omega_m - 2\omega_0)t < \pi$, ρ_0 decreases for $\phi_0 < \pi$ or $f_m < 2f_0$ and increases for $\phi_0 > \pi$ or $f_m > 2f_0$. The dynamics of parametric excitation exhibits an oscillation with phase and amplitude depending on excitation parameters. The markers of the plot correspond to the locations on the modulation frequency phase map. In the case $f_m = 143$ Hz and the phase $\phi = \pi$, the dynamics almost stays constant (square marker).

In addition, we show the details of the population dynamics for the initial phase $\phi_0 = 0$ (Figure 6.4 horizontal projection). The two distinguishable domains separated by a resonant frequency of parametric excitation. The population dynamics exhibit an oscillation during the excitation process. Near the resonant frequency, both the oscillating period and amplitude are getting larger.

6.5 Mean Field and Quantum Interpretation of Parametric Excitation

6.5.1 Coherent Dynamics Oscillation

We first discuss the excitation using the semi-classical mean field approximation. At first glance, the excitation occurs when the quadratic Zeeman energy is modulated at the integers divisor of twice natural coherent oscillation in the $\theta\rho_0$ quadrature phase space, here the quadrature angle $\theta = \theta_s/2$. The dynamics of the system are governed by a set of differential equations of the fractional population and the phase from Eqn 2.18 [109, 51].

$$\begin{aligned} \dot{\rho}_0 &= \frac{2c}{\hbar}\rho_0\sqrt{(1-\rho_0)^2 - m^2}\sin 2\theta \\ \dot{\theta} &= -\frac{q}{\hbar} + \frac{c}{\hbar}(1-2\rho_0) + \frac{c}{\hbar}\frac{(1-\rho_0)(1-2\rho_0) - m^2}{\sqrt{(1-\rho_0)^2 - m^2}}\cos 2\theta \end{aligned} \tag{6.3}$$

The spinor energy of the system is given by

$$\mathcal{E} = c\rho_0\{(1-\rho_0) + \sqrt{(1-\rho_0)^2 - m^2}\cos 2\theta\} + q(1-\rho_0)$$

The spinor dynamics has an oscillation period [109] in the form

$$T = 2\frac{\sqrt{2}\hbar}{\sqrt{-qc}}\frac{K(\sqrt{\frac{x_2-x_1}{x_3-x_1}})}{\sqrt{x_3-x_1}} \tag{6.4}$$

where $K(k)$ is the elliptic integral of the first kind, and x_i are the roots of the differential equation of the fractional population $\dot{\rho}_0 = 0$ of

$$(\dot{\rho}_0)^2 = \frac{4}{\hbar^2}([\mathcal{E} - q(1-\rho_0)][(2c\rho_0 + q)(1-\rho_0) - \mathcal{E}] - (c\rho_0 m)^2)$$

For a condensate prepared in $m_f = 0$ with magnetization conserved $m = 0$, the roots x_i are

$$x_i \in \{\frac{2c - q + \sqrt{4c^2 - 8c\mathcal{E} + 4cq + q^2}}{4c},\ \frac{q-\mathcal{E}}{q},\ \frac{2c - q - \sqrt{4c^2 - 8c\mathcal{E} + 4cq + q^2}}{4c}\}$$

The term of spinor energy, $\mathcal{E}$ is treated as a constant for a given initial averaged population $\bar{\rho}_0$ with average quadrature phase $\theta = \pi/2$ along a given energy contour $\mathcal{E} \approx q(1-\rho_0)$

The quadratic Zeeman regime $q/|c| \sim 10$ permits simplification in the mathematical description of the system. The oscillation amplitude of $\Delta\rho_0$ is given by $\Delta\rho_0 = x_2 - x_1$ [109], and has its maximum approximately $\Delta\rho_0 = 5\%$ for $\bar{\rho}_0 = 0.5$, so to the first order approximation, the population ρ_0 is constant. To approximate the period, we first calculate

$$\frac{\sqrt{-qc}}{\sqrt{2}\hbar}\sqrt{x_3 - x_1} = \frac{\sqrt{q}\left(q^2 + 4qc(2\rho_0 - 1) + 4c^2\right)^{1/4}}{2\hbar} \approx \frac{\sqrt{q^2 + 2qcx}(1 + \frac{c^2(1-x^2)}{(q+2cx)^2})}{2\hbar}$$

here $x = 2\rho_0 - 1$. The elliptical integral part of the period is

$$K(\frac{x_2 - x_1}{x_3 - x_1}) \approx K(0.01) \approx \frac{\pi}{2} \tag{6.5}$$

Substituting back into the period equation, we have the frequency of the oscillation in the quadrature phase $\theta\rho_0$

$$\begin{aligned} f_0 &= \frac{1}{T} = \frac{\sqrt{q^2 + 2qc(2\rho_0 - 1)}}{4\hbar}(1 + \frac{c^2(1-x^2)}{(q+2cx)^2})\frac{2}{\pi} \approx \frac{\sqrt{q^2 + 2qcx}}{h} \\ &\approx q + cx \end{aligned} \tag{6.6}$$

In general, we often discuss energy in terms of frequency. For simplicity, the Plank's constant will be $h \to 1$ throughout this discussion.

From the parametric excitation point of view, the modulation excites the dynamics when the modulation frequency is an integer divisor of twice the natural frequency of the system, $f = \frac{2f_0}{n}$ where $n \in \mathbb{N}$. In our system, the coherent oscillation occurs at magnetic field $B = 1$ G and spinor dynamical rate $c = -7.2(5)$ Hz; therefore, the natural frequency

$$f_0 = 71.6 \times 1^2 - 7.2x \in [64.4,\ 78.8] \text{ Hz} \quad \forall \rho_0 \in [0,\ 1] \tag{6.7}$$

The resonant frequency for $n = 1$ is,

$$f = \frac{2f_0}{1} \in [128.8,\ 157.6] \text{ Hz } \forall \rho_0 \in [0,\ 1] \tag{6.8}$$

Eqn 6.8 explains the relationship between the excitation frequency and the initial population ρ_0 observed in Figure 6.3 a. The data show the resonant frequency increases from 126 Hz to 152 Hz as $\rho_0 \in [0.96,\ 0.1]$.

6.5.2 Parametric Excitation Theory

In the high field regime $q/|c| \sim 10$, the coherent oscillation frequency is obtained from Eqn 6.6 as $\dot{\theta} \approx -2\pi(q + cx)$. This simplifies the dynamical equations Eqn 6.3 into

$$\begin{aligned} \dot{\rho}_0 &= 2c\rho_0(1-\rho_0)\sin 2\theta \\ \dot{\theta} &= -2\pi(q + c(2\rho_0 - 1)) \end{aligned} \tag{6.9}$$

Parametric excitation is applied by modulating the quadratic Zeeman energy

$$q = q_0 + q_m \sin(2\pi f_m t - \phi_0) H[t - \phi_0/2\pi f_m]$$

The Heaviside function implies that the modulation is only on after $t = \phi_0/2\pi f_m$ and the modulation sinusoidal function always starts from zero. In reality, we prepare an initial ρ_0 by an RF pulse which yields an initial quadrature phase $\theta_0 = \pi/2$,

then we let the system freely evolves for $t = \phi_0/2\pi f_m$ which changes the quadrature phase by $\Delta\theta = \phi_0$, then turn on the modulation q. In other words, we can write $q = q_0 + q_m \sin(2\pi f_m t)$ and merge the initial modulation phase $\phi_q = \phi_0/2$ into the quadrature angle θ. Integrating the phase of Eqn 6.9 with an initial phase $\theta(0) = \theta_0 - \phi_0/2$ we thus have

$$\theta = \int \dot{\theta} d\theta = \theta_0 - \phi_0/2 - \omega_0 t + \frac{2\pi q_m}{\omega_m}\cos(\omega_m t) - \frac{2\pi q_m}{\omega_m} \tag{6.10}$$

here $\omega_m = 2\pi f_m$, $\omega_0 = 2\pi(q_0 + c(2\rho_0 - 1))$. Substituting the phase into the population dynamics Eqn 6.9, we obtain

$$\begin{aligned}
\dot{\rho}_0 &= 2c\rho_0(1-\rho_0)\sin\left(2\theta_0 - \phi_0 - \frac{4\pi q_m}{\omega_m} - 2\omega_0 t + \frac{4\pi q_m}{\omega_m}\cos(\omega_m t)\right) \\
&= 2c\rho_0(1-\rho_0)\left(\sin(2\theta_0 - \phi_0 - \frac{4\pi q_m}{\omega_m} - 2\omega_0 t)\cos(\frac{4\pi q_m}{\omega_m}\sin(\omega_m t + \pi/2))\right. \\
&\quad \left. + \cos(2\theta_0 - \phi_0 - \frac{4\pi q_m}{\omega_m} - 2\omega_0 t)\sin(\frac{4\pi q_m}{\omega_m}\sin(\omega_m t + \pi/2))\right) \\
&= 2c\rho_0(1-\rho_0) \\
&\quad \times \sum_n J_n(\frac{4\pi q_m}{\omega_m})\sin((n\omega_m - 2\omega_0)t + 2\theta_0 - \phi_0 - \frac{4\pi q_m}{\omega_m} + n\pi/2)
\end{aligned} \tag{6.11}$$

where we have used the Jacobi-Anger expansions

$$\cos(z\sin\alpha) = \sum_{n=-\infty}^{\infty} J_n(z)\cos(n\alpha) \qquad \sin(z\sin\alpha) = \sum_{n=-\infty}^{\infty} J_n(z)\sin(n\alpha)$$

Analyzing Eqn 6.11 explains a lot of properties of parametric excitation phenomenon. When $\omega_m \neq 2\omega_0/n$ the time-average of $\dot{\rho}_0$ is zero. When $\omega_m = 2\omega_0/n$, the time average $\dot{\rho}_{0,n} = 2c\rho_0(1-\rho_0)J_n(\frac{4\pi q_m}{\omega_m})\sin(2\theta_0 - \phi_0 - \frac{4\pi q_m}{\omega_m} + n\pi/2)$ is non-zero. This explains the integer divisor of twice the natural frequency signature of the parametric excitation spectrum as seen Figure 6.3 b. The Bessel function $J_n(4\pi q_m/\omega_m)$ indicates that larger modulation amplitude q_m results in larger excitation amplitude $\Delta\rho_0$ as seen in Figure 6.3 c.

Considering the case $\omega_m = 2\omega_0$, the higher order term n of $J_n(\frac{4\pi q_m}{\omega_m})$ is negligible,

and we are left with

$$\begin{aligned}\dot{\rho}_0 &= 2c\rho_0(1-\rho_0)J_{-1}(\frac{4\pi q_m}{2\omega_0})\sin(-4\omega_0 t+2\theta_0-\phi_0-\frac{4\pi q_m}{2\omega_0}-\pi/2)\\ &\quad +2c\rho_0(1-\rho_0)J_0(\frac{4\pi q_m}{2\omega_0})\sin(-2\omega_0 t+2\theta_0-\phi_0-\frac{4\pi q_m}{2\omega_0})\\ &\quad +2c\rho_0(1-\rho_0)J_1(\frac{4\pi q_m}{2\omega_0})\sin(2\theta_0-\phi_0-\frac{4\pi q_m}{2\omega_0}+\pi/2)\end{aligned}$$

Integrating the derivative $\dot{\rho}_0$,

$$\begin{aligned}\rho_0 &= 2c\rho_0(1-\rho_0)J_{-1}(\frac{4\pi q_m}{2\omega_0})\frac{1}{4\omega_0}\cos(-4\omega_0 t+2\theta_0-\phi_0-\frac{4\pi q_m}{2\omega_0}-\pi/2)\\ &\quad +2c\rho_0(1-\rho_0)J_0(\frac{4\pi q_m}{2\omega_0})\frac{1}{2\omega_0}\cos(-2\omega_0 t+2\theta_0-\phi_0-\frac{4\pi q_m}{2\omega_0})\\ &\quad +2c\rho_0(1-\rho_0)J_1(\frac{4\pi q_m}{2\omega_0})\sin(2\theta_0-\phi_0-\frac{4\pi q_m}{2\omega_0}+\pi/2)t+\rho_0(0)\end{aligned}$$

The population $\rho_0(t) \approx \rho_0(0)$ if $\phi_0 \approx 1.37\pi$ and $\omega_m = 2\omega_0$. Compared to data in Figure 6.4, $\rho_0(t) \approx \rho_0(0)$ if $\phi_0 \approx \pi$ and $\omega_m = 2\omega_0$. The discrepancy in the initial modulation phase between data and theory is 0.37π. This phase discrepancy is equivalent to 1.3 ms of delay between the magnetic field pulse relative to an initial RF pulse. From the experiment, we know that the first magnetic field pulse is delayed about 0.5 ms. Probably the magnetic hysteresis causes the overall delay of 1.3 ms during parametric excitation. In fact, the magnetic hysteresis of parametric excitation increases the overall field by 15 mG compared to when there is no modulation.

6.5.3 Fock States

An alternative way to view the parametric excitation is as the transitions between the eigenstates of the many-body Hamiltonian. The energy corresponding to the oscillation frequency matches no single atom transition. Rather it approximately matches the energy difference between two atoms in the $m_f = 0$ state and two atoms one each in the $m_f = \pm 1$ states. These energy separations can be calculated by

diagonalizing the tridiagonal matrix given by

$$\begin{aligned}\mathcal{H}_{k,k'} &= \{2\lambda k(2(N-2k)-1)+2qk\}\delta_{k,k'} \\ &+ 2\lambda\{(k'+1)\sqrt{(N-2k')(N-2k'-1)}\delta_{k,k'+1} \\ &+ k'\sqrt{(N-2k'+1)(N-2k'+2)}\delta_{k,k'-1}\} \end{aligned} \tag{6.12}$$

where k is the number of pairs of $m_f = \pm 1$ atoms in the enumeration of the Fock basis. The Fock basis, $|N, M, k\rangle$, is also enumerated with N the total number of atoms and M the magnetization, both of which are conserved by the Hamiltonian leaving all dynamics in k. This variation of the drive frequency is due to the many body interaction given by the $\lambda\hat{S}^2$ term of the Hamiltonian which contribute the off diagonal terms in Eqn 6.12. This interaction results in a slight mixing of the Fock states, even in the high field limit. Without this interaction, there would be no transitions since the magnetic interaction, both linear and quadratic Zeeman, is diagonal in the Fock basis.

For the high field regime considered here ($q/|c| \ 10$), we can treat λ as a perturbation, and $\mathcal{H}^{(0)}_{k,k'} = 2qk$. The perturbation eigenenergy of the Fock state is

$$\begin{aligned} E^{(0)}_k &= 2qk \\ E^{(1)}_k &= \langle k|\mathcal{H}'|k\rangle = 2\lambda k\left(2(N-2k)-1\right) \end{aligned}$$

The eigenenergy of the system is thus

$$E_k = E^{(0)}_k + E^{(1)}_k + \mathcal{O}^{(2)}$$

The resonant frequency between Fock states is the energy difference between each Fock state.

$$\begin{aligned} f &= \frac{\partial E_k}{\partial k} = 2q + 2\lambda(2N - 8k - 1) \\ &\approx 2q + 2c(2\rho_0 - 1) = 2(q + cx) \end{aligned}$$

To the first order expansion, the resonant frequency between Fock states are the same as the resonance frequency, $2f_0/1$, obtained from the mean field approach. In this picture the integer divisor frequencies of the spectrum, $2f_0/n$, would correspond to a many photon driving of the transition [142].

CHAPTER 7

PARAMETRIC EXCITATION AND RECTIFIER PHASE CONTROL

In the previous chapter, we demonstrated the coherent dynamics in the high magnetic field regime and the parametric excitation. In this chapter, we will investigate the quantum control technique using parametric excitation and the rectifier phase control.

7.1 Parametric at the Pole

Similar to a classical pendulum, if the initial oscillation amplitude is zero, the system remains unperturbed by the parametric excitation. For a condensate initiated at the top pole of the spin-nematic sphere $S_\perp Q_\perp x$ (Figure 6.1), the oscillation amplitude is zero. The oscillation amplitude should remain zero under parametric excitation. However, the distribution of the initial states at the pole has a quantum uncertainty $1/\sqrt{N}$ in $S_\perp$ and $Q_\perp$ which results in a distribution of initial states at $\rho_0 \approx 1$. This non-zero noise distribution of ρ_0 generates a distribution of nonzero oscillation amplitudes. When the parametric excitation is applied long enough, it can excite the condensate away from the spin-nematic pole.

An experiment is performed with condensate of $N = 4\times10^4$ atoms initiated in the $|f = 1, m_f = 0\rangle$ state at the high magnetic field $B = 2$ G. We apply a quench to bring the magnetic field down to 1 G ($q/|c| \sim 10$) then apply the parametric excitation. The population ρ_0 or transverse magnetization noise ΔS_x are measured after a certain period.

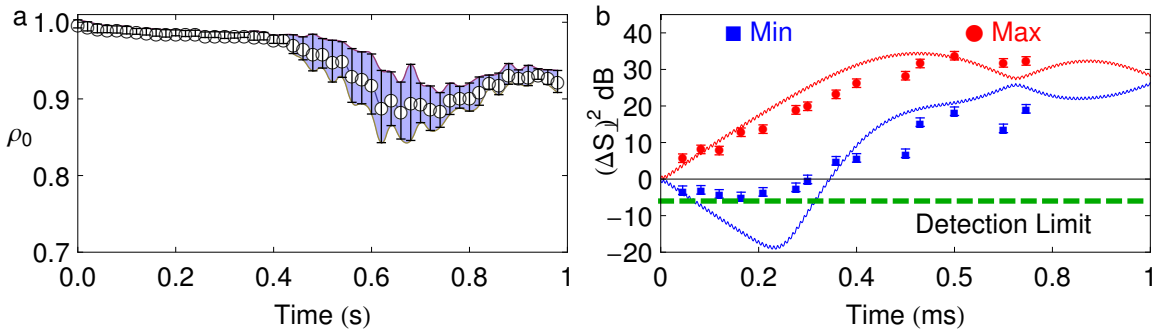

Figure 7.1: Parametric excitation at the pole. The dynamics evolution of ρ_0 (a) and $(\Delta S_\perp)^2$ (b) for parametric excitation with initial $\rho_0 = 1$. Magnetic field is modulated by $q = q_0 + q_m \sin(2\pi f_m t - \phi_0)$, for $B_0 = 1$ G, $B_m = 0.785$ G, and $f_m = 134 \sim 134.5$ (Hz).

7.1.1 Spinor Population Dynamics

Applying parametric excitation with modulation $f_m = 134 \sim 134.5$ (Hz), we measure the population ρ_0 during 1 s of excitation. If there is no noise in the initial distribution of ρ_0, there will be no excitation. Therefore, the dynamics of parametric excitation at the pole is noise driven excitation. Unlike the normal parametric excitation that happens right after the modulation is applied, the noise driven excitation experiences an initial pause of 400 ms before evolving away from the pole (Figure 7.1 a). This is similar to the initial pause of the quantum spin mixing where squeezing occurs [56, 50]. It turns out that squeezing also occurs in the noise driven excitation. During these first 400 ms, the uncertainty of the transverse magnetization $\Delta S_\perp$ squeezes in one quadrature axis and grows along the transverse axis, and then eventually evolves away from the poles. The population dynamics of the noise driven excitation is similar to quantum spin mixing; they both generate a large uncertainty in population ρ_0 [61]. This experiment demonstrates the ability to excite the condensate from the pole $\rho_0 = 1$; together with the parametric excitation for $\rho_0 < 1$ demonstration, it is possible to use parametric excitation to control condensate in the full range $\rho_0 \in [0, 1]$.

7.1.2 Squeezing

As briefly mentioned earlier, the noise driven excitation generates squeezing in the spin-nematic $S_\perp Q_\perp$ space. The distribution of condensate at the stable elliptical fixed point in spin-nematic space has initial uncertainty of $1/\sqrt{N}$ (0 dB) [56] at the SQL. During the parametric excitation, the squeezing develop along a given path determined by the modulation settings. In simple language, you can think of the initial distribution as a circle, and the squeezing process transforms the circle into an ellipse. On one axis, the ellipse diameter is getting smaller than initial circle diameter, and on the other axis the diameter is larger. Once the noise builds up enough, it will drive the spinor population out of the pole, and the transverse magnetization uncertainty grows above the SQL. This is similar to the quantum spin mixing where the initial fluctuation is the key ingredient to trigger the dynamics [143, 56].

In the $q/|c| \sim 10$ regime, the distribution in $S_\perp Q_\perp$ rotates as a result of a coherent oscillation with $f_0 = \sqrt{q^2 + 2cqx}$. Due to the symmetry in the spin-nematic phase space (a rotation of the ellipse about its center is π-periodic), the dynamics are periodic every π instead of 2π. The uncertainty $\Delta S_\perp$, the projection of the distribution on the $S_\perp$ axis, thus oscillates with the same frequency - a typical oscillation period is about 7 ms. For this reason, we do not need to do the quadrature phase rotation in order measuring squeezing. We can measure $\Delta S_\perp$ every 1 ms in order to construct the quantum state distribution in $S_\perp Q_\perp$. The overall distribution of the quantum states is obtained by measuring $\Delta S_\perp$ at different times during a period $1/2f_0$ after applying parametric excitation. The uncertainty $\Delta S_\perp$ depends on the orientation of the condensate distribution with the $S_\perp$ axis. The maximum and minimum squeezing are extracted from the value of $\Delta S_\perp$ during one period of time $1/2f_0$.

In the experiment, we apply a modulation frequency of $f_m = 134.5$ Hz to the condensate. During the first 300 ms, the minimum uncertainty $\Delta S_\perp$ goes below the SQL, and close to our detection limit as shown in Figure 7.1 b. The maximum

uncertainty grows exponentially above the SQL after that. The experimental data is fitted to simulation. After 300 ms, the minimum and maximum uncertainty grows to 20∼30 dB which is about 100∼1,000 times larger than the SQL.

For a spin-1 system with $q < 2|c|$, the condensate squeezes naturally along the divergent separatrix [56]. However, for $q > 2|c|$, there is no separatrix in the spin-nematic phase space. The squeezing is the result of modulating the quadratic Zeeman term in the spinor energy. This experiment demonstrates a quantum control method to artificially generate the squeezing in a spin-1 system.

7.2 Parametric Excitation Controlling ρ_0

We learned from the parametric excitation that the spinor quantum states or population ρ_0 responds differently depending on the modulation frequency and the initial modulation phase. We have demonstrated the parametric excitation of ρ_0 about some fixed values, for example, $\rho_0 = 0.5$. In this section, we will extend our model to control ρ_0 from 1 to 0. From the previous section on noise driven excitation, we have shown that it is possible to parametrically excite the population out of the pole $\rho_0 = 1$. However, it would take so long for the dynamics to happen, about 400 ms. At this time scale, the atom loss becomes significant, and we might loss atoms before ρ_0 reaches our desired value. Therefore, we will start with an initial $\rho_0 \approx 1$, for instance, $\rho_0 = 0.96$.

7.2.1 Experimental Concept

The natural oscillation frequency of the system is $f_0 = \sqrt{q_0^2 + 2q_0cx} \approx q_0 + cx$. The first order resonance frequency $f_1 = 2f_0/1 = 2q_0 + 2cx$. Some of the experimental tests show that population ρ_0 (or $x = 2\rho_0 - 1$) follows a sinusoidal curve as it is driven down by parametric excitation. Moreover, the modulation frequency explicitly depends on the value of ρ_0. Therefore, the modulation frequency is not fixed; instead, the modulation frequency follow the sinusoidal function, $f_m(t) = 2q_0 + 2c\cos 2\pi f_F t$, as ρ_0

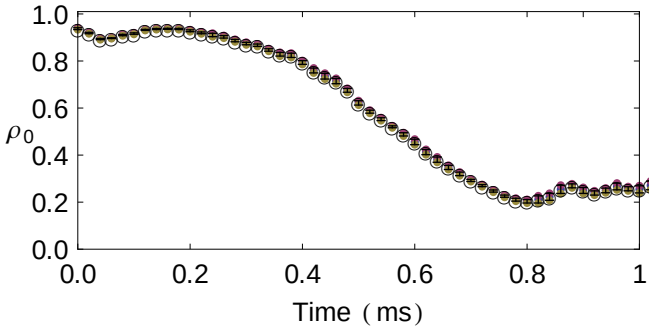

Figure 7.2: Parametric excitation control ρ_0. (a) Control ρ_0 by applied parametric excitation $q = q_0 + q_m \sin(2\pi f_m(t)t - \phi_0)$ for magnetic field $B_0 = 1$ G, and $B_m = 0.785$ G. The modulation frequency $f_m(t) = 2q_Z B_0^2 + 2c\cos 2\pi f_F t$ and $f_F = 0.25$ Hz

changes. The modulation frequency will sinusoidally increase from $2q_0+2c \rightarrow 2q_0-2c$ after a half period of time $t = 1/2f_F$, and the population ρ_0 will goes down from $1 \rightarrow 0$. Here, f_F is the frequency of the modulation frequency. The quadratic Zeeman energy is modulated by

$$q = q_Z B^2 = q_0 + q_m \sin\left(2\pi f_m(t)t - \phi_0\right) H[t - \phi_0/2\pi f_m] \tag{7.1}$$

The experiment follows the same procedure of the previous parametric excitation experiments. We prepare the initial $\rho = 0.96$ by an RF pulse, then apply the parametric excitation by modulating the quadratic Zeeman. We try to transfer atoms from $\rho_0 = 0.96$ to $\rho_0 = 0$ as close as possible.

7.2.2 Population Dynamics

This control is the search of two parameters, the frequency of the modulation frequency f_F and the initial modulation phase ϕ_0. These two parameters depend explicitly on the trap life time and the magnetic field; therefore, the optimal values of f_F and ϕ_0 vary depending on the conditions of the experiment. To search for the optimal f_F and ϕ_0, we measure the population ρ_0 after a period of excitation (for example 800 ms). The combination of (f_F, ϕ_0) yield the lowest value of ρ_0 will be chosen. In Figure 7.2 we show the result using $f_F = 0.25$ (Hz) and $\phi_0 = 0.86\pi$. The modulation

can excite atoms from $\rho_0 = 0.96 \rightarrow 0.2$ after 800 ms. The excitation time scale of 800 ms is comparable to the trap lifetime of 1.8 s. To make the parametric excitation control more practical, we need to make to its dynamics happen faster. The simulation shows that we should be able to bring $\rho_0 \rightarrow 0.05$; however, the experimental result shows the limit of $\rho_0 = 0.2$. We have tried different ramp curves (hyperbolic tangent and exponential) for the modulation frequency function $f_m(t)$; however, the cosine curve $f_m(t)$ gives the best result. It is possible that the atom loss (trap life time is 1.8 s) and the magnetic field hysteresis due to the magnetic field modulation significantly change the natural coherent frequency of the system during 800 ms of modulation. This makes the system does not behave as well as the simulation predicts. Despite some of the limitations, the experimental data does demonstrate an ability to prepare and control the population ρ_0 within a wide range of values.

7.3 Rectifier Phase Control

The spinor coherent dynamics has been discussed previously in section 6.1. In the high magnetic field regime $q/|c| \sim 10$, the coherent oscillation on spinor phase $\theta_s\rho_0$ space has a small oscillation amplitude in ρ_0 [109],

$$\Delta\rho_0 = -c(1-x^2)/2(q+2cx) \tag{7.2}$$

The conceptual $\theta_s\rho_0$ spinor phase space is shown in Figure 7.3 a. For a given initial population ρ_0 with an initial spinor phase $\theta_s = \pi$, there is an unique energy contour associated with it. There is a small depth on each energy contour which translates into the oscillation of the population ρ_0. We can think of the spinor dynamics ρ_0 as an ac oscillation on top of a dc offset. By applying the phase shift $\Delta\theta_s$, we can move the condensate from one energy contour to another, and we effectively change the dc offset of ρ_0. The rectifier phase control relies on the spinor phase shift $\Delta\theta_s$ to transfer condensate across energy contour and change the dc offset of the coherent oscillation.

7.3.1 Rectifier Phase Concept

A microwave phase pulse shifts the spinor phase of the condensate in spinor phase $\theta_s\rho_0$, effectively moving the condensate to a new energy contour. In theory, it is possible to use any spinor phase shift $\Delta\theta_s$ to control the condensate across the energy contours. However, using the phase shift $\Delta\theta_s = -\pi$ simplifies the control procedure. As seen in Figure 7.3 a, the spinor phase difference between the highest and lowest positions on a given energy contour is π. First of all, we choose a fixed microwave π phase shift which corresponds to a microwave pulse of detuning $\delta = -\Omega/\sqrt{3}$ where Ω is the Rabi rate of the microwave transition from $|F = 1, m_f = 0\rangle \rightarrow |F = 2, m_f = 0\rangle$. Secondly, the π pulse transfers atoms from the lowest (highest) point of one contour

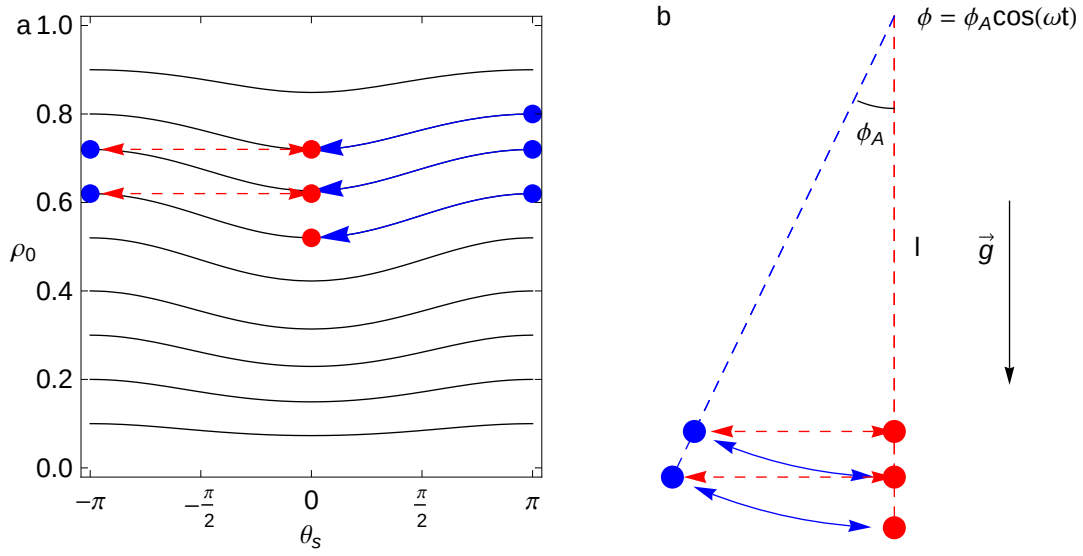

Figure 7.3: Rectifier concept. (a) The condensate (blue dots) evolves along the energy contours during the coherent oscillations (blue trails). Microwave pulse is applied to shift the spinor phase by an amount $\Delta\theta_s = -\pi$ (red dashed lines) to move condensate from lowest (highest) positions of the current energy contours to highest (lowest) positions of the new energy contours. (b) The classical pendulum analog of rectifier phase control, $\phi = \phi_A \cos(\omega t)$. The π microwave phase shift is equivalent to a change of the rod length from l (length $l/\cos\phi_A$) to $l/\cos\phi_A$ (length l), changing the pendulum angle from the zero (angle $-\phi_A$) to the angle $-\phi_A$ (angle zero), and resetting the velocity to zero ($\sqrt{2gl(1-\cos\phi_A)/\cos\phi_A}$).

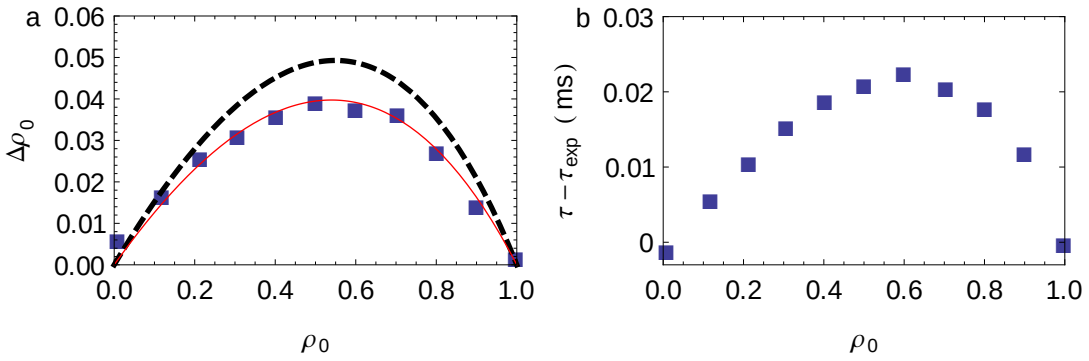

Figure 7.4: Coherent oscillation amplitude. The amplitude of coherent oscillation depends on the initial value of ρ_0. (a) The experimental data (squares) are compared to the analytical form $\Delta\rho_0 = -c(1-x^2)/2(q+2cx)$ for $c = -7.2 \times 2\pi$ Hz and $q = q_Z \times B_0^2 = 71.6 \times 2\pi$ Hz (black dashed line), and fitted with $c = -5.7 \times 2\pi$ Hz and fixed $q = 71.6 \times 2\pi$ Hz (red solid line). (b) The discrepancy of theory and experimental pulse separation.

to the highest (lowest) of another contour; hence, the phase shift maximizes the change of the dc offset of the population ρ_0. Thirdly, it takes exactly a half of the coherent oscillation period $\tau = 1/2f$ for the condensate to evolve from the highest (lowest) location to the lowest (highest) location; therefore, we know exactly the time separations τ between pulses. Here, $f = 2q + 2c(2\rho_0 - 1)$ is the frequency of the coherent oscillation, q and c are quadratic Zeeman energy and spinor dynamical rate.

Applying the microwave pulses at the right time is crucial, and we will consider the following simple case for some insight. Let us say that after an ith microwave pulse, we have a population $\rho_{0,i}$ with the spinor phase π. The time $\tau_{0,i}$ for condensate evolving from highest (lowest) location to lowest (highest) location can be calculated from $\rho_{0,i}$, and the population difference between the highest to the lowest location on the energy contour $\Delta\rho_0$ is given by

$$f_i = 2(q + cx_i) \qquad \tau_i = \frac{1}{4(q+cx_i)} \qquad \Delta\rho_{0,i} = \frac{-c(1-x_i^2)}{2(q+2cx_i)}$$

Here $x_i = 2\rho_{0,i} - 1$. After the condensate evolves for a period of $\tau_{0,i}$, the π phase shift pulse is applied at the population $\rho_{0,i} - \Delta\rho_{0,i}$. The new population is $\rho_{0,i+1} = \rho_{0,i} - \Delta\rho_{0,i}$, and the new spinor phase is π (same as $-\pi$ since the dynamics are 2π

periodic). Similarly, we have the new values of

$$f_{i+1} = 2(q + cx_{i+1}) \qquad \tau_{i+1} = \frac{1}{4(q + cx_{i+1})} \qquad \Delta\rho_{0,i+1} = \frac{-c(1 - x_{i+1}^2)}{2(q + 2cx_{i+1})}$$

Repeating this procedure, we can predict accurately the separation periods τ between each π microwave pulse and the population ρ_0 in order to control the condensate crossing the energy contours.

In Figure 7.4 a, we show the data of coherent oscillation amplitude $\Delta\rho_0$ for different initial population ρ_0. The data are compared to the analytical solution in Eqn 7.2. Using the experimental parameters of the spinor dynamical rate $c = -7.2 \times 2\pi$ Hz (measured a couple months ago) and the quadratic Zeeman energy $q = q_z B_0^2 = 71.6 \times 2\pi$ Hz, the data agree quantitatively with the analytical solution with a small discrepancy, possibly due to the uncertainty in the measurement of c and q. The data fit best with $c = -5.7 \times 2\pi$ Hz and $q = 71.6 \times 2\pi$ Hz. Recently, our measurement of the spinor dynamical rate using coherent oscillation yields $c = 5 - 6$ Hz. In the experiment, we applied the sequence of pulses separated by the theoretical determined periods of $\tau = 1/2(2q + 2cx)$. Comparing to the experimental separation periods τ_{exp} calculated from the data (from Figure 7.4 a), the discrepancy at maximum is 0.025 ms or 0.7% at $\rho_0 = 0.5$. For this reason, we should be able to generate a sequence of microwave pulses separated by the analytical formula of $\tau = 1/4(q + cx)$ for the rectifier control.

The classical pendulum analog of the rectifier control is shown in Figure 7.3 b. Depending on whether we want to move the oscillation orbit up or down, we will apply the rectifier phase shift at the different positions during the oscillation.

7.3.1.1 Experimental Method

An experiment was performed in a condensate of $N = 4 \times 10^4$ atoms initiated in the $|f = 1, m_f = 0\rangle$ state at high magnetic field of 2 G. To trigger the dynamics, the magnetic field is quenched to 1 G. A sequence of π microwave pulses is applied to shift

the spinor phase of the quantum states (see Sec. 3.2.1). Finally, the spin populations of the condensate are measured. This is executed by releasing the trap and allowing the atoms to freely expand in a Stern-Gerlach magnetic field gradient to separate the m_f spin components.

7.3.2 Rectifier Phase Population Control

Since the microwave pulse has a fixed π phase shift, the rectifier phase control is simplified into one parameter search τ, the separation period between pulses. For this reason, the rectifier control is very robust. We will demonstrate different ρ_0 controlling scenarios. Each data point is only repeated 4 times because of the low noise characteristics of the coherent oscillation.

In the first experiment, we demonstrate the ability to transfer initial population $\rho_0 = 0.96 \rightarrow 0$. In Figure 7.6 a, the initial $\rho_0 = 0.96$ is driven to $\rho_0 = 0.03$ using a sequence of π phase shift microwave pulses. Each pulse is separated by $\tau = 1/2f$, which transfers the condensate from the lowest locations of current energy contours to the highest locations of new contours. The result demonstrates that the rectifier control is capable of controlling ρ_0 and the quantum states of the system at almost a

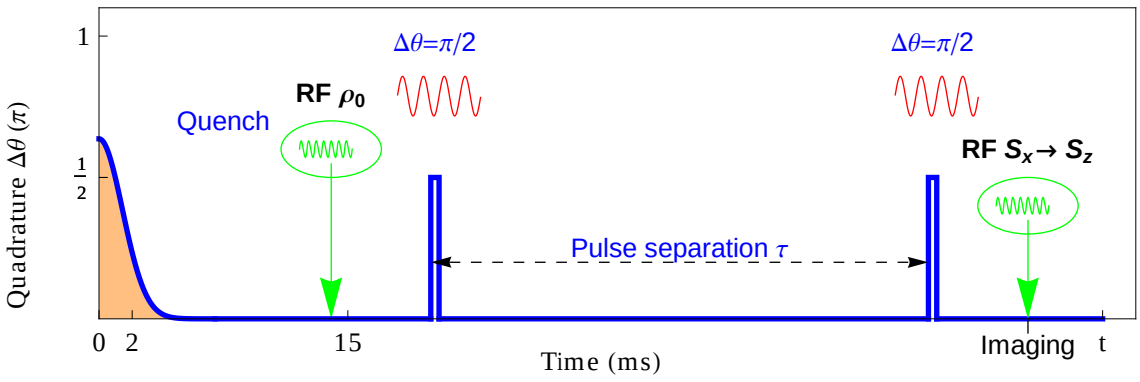

Figure 7.5: Rectifier experimental sequence. To initiate the dynamics, the magnetic field is quenched from 2 G to 1 G. Each π microwave pulse is separated by a period τ. The imaging setup captures the spinor population or the transverse magnetization by applied an RF to rotate $S_x \rightarrow S_z$.

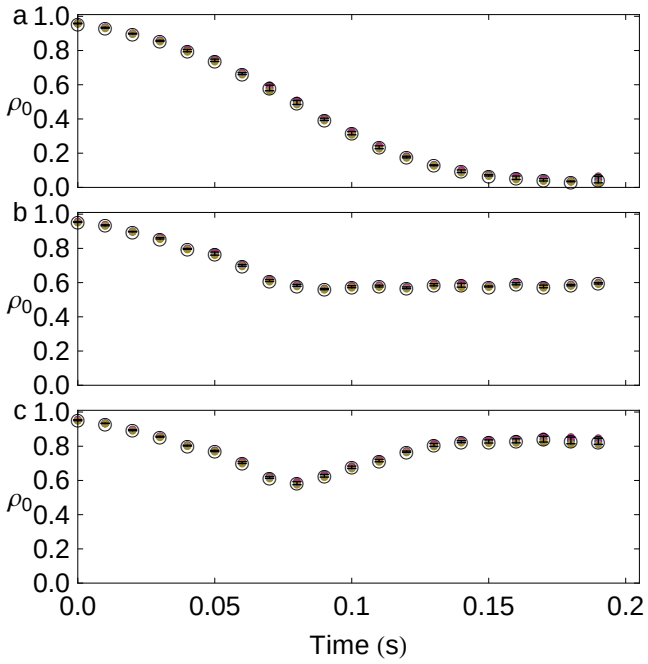

Figure 7.6: Rectifier control. (a) Rectifier phase controls population $\rho_0 : 1 \rightarrow 0$.

full range.

We can also transfer ρ_0 to a desired value. In Figure 7.6 b, we demonstrate an experiment to transfer $\rho_0 = 0.96 \rightarrow 0.6$ by a sequence of microwave pulses. The pulses are turned off after $\rho_0 = 0.6$. The data shows the population reaches 0.6 as desired, and the ρ_0 exhibits a very small amplitude (less than 0.02) coherent oscillation later.

Applying the rectifier control, we can move the condensate both ways to higher or lower energy contours (Figure 7.3 a). To demonstrate this idea, we first transfer $\rho_0 \rightarrow 0.6$ using a similar pulse sequence in Figure 7.3 b. Once $\rho_0 = 0.6$, we send a mirror of pulse sequence in Figure 7.6 b to bring the population up again. The result is shown in Figure 7.6 c. Even though, ρ_0 does not come all the way back to 0.96, it still demonstrates the main effect.

Understanding the dynamics of the system enables us to reduce the complexity of the controlling procedure into a single parameter. The rectifier phase control relies on a simple phase shift technique; nevertheless, it has proven to be an effective control

method for many body spin systems.

CHAPTER 8

SPIN RELAXATION IN A THERMAL GAS

We have been focused on the spinor dynamics of Bose-Einstein condensates, but not thermal gases above the BEC critical temperature. At one point, we are curious about the spinor dynamics of the thermal gas and what would be the equilibrium for the spinor population. For the thermal ^{87}Rb atoms above the BEC critical temperature, the theoretical prediction is $\rho_1 : \rho_0 : \rho_{-1} = \frac{1}{3} : \frac{1}{3} : \frac{1}{3}$ [144]. The spinor dynamics of a thermal gas have been studied in the finite temperature of Bose-Einstein condensates [145] and coherent oscillation of antiferromagnetic spin-1 [146]. In this chapter, we will discuss our preliminary results of studying spin relaxation in thermal gas for different magnetic fields and the atom loss rates.

8.1 Basic Theory

The theory of a Bose gas above BEC temperature has been studied in great detail by Yuki Endo and Tetsuru Nikuni [144, 147]. This section follows closely the derivation procedure of spinor dynamics from Endo and Nikuni in order to understand the experimental result of the spin relaxation dynamics later. The Hamiltonian of a Bose gas can be described as [105, 84]

$$\begin{aligned}\hat{\mathcal{H}} &= \sum_{i,j}\int dr\hat{\psi}_i^\dagger(\vec{r},t)\langle i|\hat{\mathcal{H}}_0|j\rangle\hat{\psi}_j(\vec{r},t) \\ &\quad +\frac{g_0}{2}\sum_{i,j}\int dr\hat{\psi}_i^\dagger(\vec{r},t)\hat{\psi}_j^\dagger(\vec{r},t)\hat{\psi}_j(\vec{r},t)\hat{\psi}_i(\vec{r},t) \\ &\quad +\frac{g_2}{2}\sum_{i,j,i',j'}\sum_{\alpha}\int dr\hat{\psi}_i^\dagger(\vec{r},t)\hat{\psi}_{i'}^\dagger(\vec{r},t)S_{ij}^{\alpha}S_{i'j'}^{\alpha}\hat{\psi}_{j'}(\vec{r},t)\hat{\psi}_{i'}(\vec{r},t) \qquad (8.1)\end{aligned}$$

where i, j are the Zeeman levels of the hyperfine state m_f. The Hamiltonian of a single atom is written as [147]

$$\hat{\mathcal{H}}_0 = \left[-\frac{\hbar^2}{2m}\nabla^2 + V(\vec{r})\right]\mathbf{1} + g\mu_B \sum_\alpha B^\alpha(\vec{r},t)\mathbf{S}^\alpha + \sum_{\alpha,\beta} B_q^{\alpha\beta}(\vec{r},t)\mathbf{Q}^{\alpha\beta} \quad (8.2)$$

The first term is the kinetic energy of the atoms and the potential energy of the harmonic trap $V(\vec{r}) = \frac{m}{2}(\omega_x^2 x^2 + \omega_y^2 y^2 + \omega_z^2 z^2)$. The second term is the linear Zeeman effect where B^α is the magnetic field in a spin-α component, and $\mathbf{S}^\alpha(\alpha = x, y, z)$ is the spin matrix. The third term is the quadratic Zeeman effect where $B_q^{\alpha\beta}$ is the magnetic field in quadratic $\alpha\beta$ component, and $\mathbf{Q}^{\alpha\beta} = (1 - \frac{1}{2}\delta_{\alpha\beta})(\mathbf{S}^\alpha\mathbf{S}^\beta + \mathbf{S}^\beta\mathbf{S}^\alpha - \delta_{\alpha\beta})\frac{2}{3}\mathbf{S}^2$ is the quadrupole matrix. The position vector is $\vec{r}$, and the momentum vector is $\vec{p}$, here the bold notation $\mathbf{A}$ is the 3×3 matrix operator. The Wigner quasiprobability distribution [148] in the position-momentum phase space of the wave function is written as

$$\hat{W}_{ij}(\vec{p},\vec{r}) = \int d\vec{r'} e^{i\vec{p}\cdot\vec{r}/\hbar} \langle \hat{\psi}_j^\dagger(\vec{r} + \vec{r'}/2)\hat{\psi}(\vec{r} - \vec{r'}/2)\rangle \quad (8.3)$$

The semi-classical distribution function is

$$W_{ij}(\vec{p},\vec{r},t) = \langle i|\mathbf{W}(\vec{p},\vec{r})|j\rangle = \mathrm{Tr}\hat{\rho}(t)\hat{W}_{ij}(\vec{p},\vec{r}) \quad (8.4)$$

where $\hat{\rho}(t) = \sum_i p_i|i\rangle\langle j|$ is the density operator. The local number density of atoms is given by

$$\mathbf{n}(\vec{r},t) = \int \frac{d\vec{p}}{(2\pi\hbar)^3}\mathbf{W}(\vec{p},\vec{r},t) \quad (8.5)$$

The dynamics of the Wigner distribution can be obtained from the Heisenberg equation of motion

$$\frac{\partial}{\partial t}W_{ij}(\vec{p},\vec{r},t) = \frac{1}{\hbar}\mathrm{Tr}\hat{\rho}(t)\left[\hat{W}_{ij}(\vec{p},\vec{r}), \hat{\mathcal{H}}(t)\right]$$

Which leads to the semi-classical kinetic equation [147]

$$\frac{\partial W_{ij}}{\partial t} + \frac{\vec{p}}{m}\cdot\nabla_r W_{ij} - \frac{1}{2}\{\nabla_r U_{ij}, \nabla_p W_{ij}\} - \frac{i}{\hbar}[W_{ij}, U_{ij}] = I_{ij} \quad (8.6)$$

Here the square brackets $[,]$ are the commutator operator, and curly brackets $\{,\}$ are the anti-commutator operator. The effective potential is defined as

$$\mathbf{U} = \mathbf{V} + g_0 n\mathbf{1} + g_0\mathbf{n} + \sum_\alpha \{g\mu_B B^\alpha \mathbf{S}^\alpha + g_2 M^\alpha \mathbf{S}^\alpha + g_2 \mathbf{S}^\alpha \mathbf{n} \mathbf{S}^\alpha\} + \sum_{\alpha\beta} B_q^{\alpha\beta} \mathbf{Q}^{\alpha\beta}$$

and the magnetization $M^\alpha(\vec{r},t) = \mathrm{Tr}[\mathbf{n}(\vec{r},t)\mathbf{S}^\alpha]$. The collision integral is I_{ij} [147]

$$I_{ij} = \frac{1}{i\hbar}\mathrm{Tr}\hat{\rho}(t_0)\left[\hat{W}_{ij}(\vec{r},\vec{p},t), \hat{\mathcal{H}}'(t)\right] \tag{8.7}$$

where $\hat{\mathcal{H}}'(t) = \hat{\mathcal{H}}(t) - \hat{\mathcal{H}}_{MF}(t)$ is the non-mean-field Hamiltonian term. This term does not have the Zeeman effect. If the term $\hat{W}_{ij}(\vec{r},\vec{p},t)$ does not include the Zeeman effect, the collision integral will be independent of the magnetic field.

The temperature of our Bose gas is in the μK regime, the phase density is low, and the spin collision happens slowly. With this condition, we assume that at any given time, the system is close to equilibrium. To first order, the Wigner distribution

$$W_{ij}^0 = \delta_{ij} f_i(\vec{p},\vec{r},t) = \delta_{ij} e^{-\beta_i(\epsilon_i - \mu_i)} \tag{8.8}$$

where $f_i(\vec{p},\vec{r},t)$ is the equilibrium distribution, $\epsilon_i = p^2/2m + U_{ii}$ is the excitation energy, and μ_i is the chemical potential of the Zeeman sub-levels of the hyperfine state, and $\beta_i = 1/k_B T_i$. Using this approximation and the expression for the non-mean-field Hamiltonian, the collision integral thus becomes [147]

$$\begin{aligned} I_{ii} = {} & \frac{\pi}{\hbar}\sum_{j,i',j'}\sum_{\alpha\beta}\int\frac{d\vec{p}_2}{(2\pi\hbar)^3}\int\frac{d\vec{p}_3}{(2\pi\hbar)^3}\int d\vec{p}_4\,\delta(\vec{p}+\vec{p}_2-\vec{p}_3-\vec{p}_4)\delta(\epsilon_{i\vec{p}}+\epsilon_{j\vec{p}_2}-\epsilon_{i'\vec{p}_3}-\epsilon_{j'\vec{p}_4}) \\ & \times 2g_2^2\left(S^\alpha_{ii'}S^\beta_{i'i}S^\alpha_{jj'}S^\beta_{j'j} + S^\alpha_{ij'}S^\beta_{j'i}S^\alpha_{ji'}S^\beta_{i'i}\right)\left(f_{i'}(\vec{p}_3)f_{j'}(\vec{p}_4) - f_i(\vec{p})f_j(\vec{p}_2)\right) \end{aligned}$$

The number of atoms at the state i can be calculated from the local density Eqn 8.5

$$N_i(t) = \int dr\ n_{ii} = \int d\vec{r}\int\frac{dp}{(2\pi\hbar)^3}W_{ii}(\vec{p},\vec{r}) \tag{8.9}$$

where $n_{ii}(\vec{r},t) = \langle i|\mathbf{n}(\vec{r},t)|j\rangle = \langle\hat{\psi}_j^\dagger(\vec{r},t)\hat{\psi}_i(\vec{r},t)\rangle$. Taking the time derivative of the number of atoms we have

$$\frac{dN_i}{dt} = \int d\vec{r}\int\frac{d\vec{p}}{(2\pi\hbar)^3}\frac{W_{ii}(\vec{p},\vec{r})}{dt} \tag{8.10}$$

Since every term on the left of Eqn 8.6 except for the first term are odd functions, the integral vanishes, therefore [144]

$$\begin{aligned}\frac{dN_i}{dt} &= \int d\vec{r}\int \frac{d\vec{p}}{(2\pi\hbar)^3} I_{ii}(\vec{p},\vec{r},t) \\ &= 2\frac{\gamma_i}{\beta_i}\sum_{ji'j'}\sum_{\alpha\beta}\left(S^{\alpha}_{ii'}S^{\beta}_{i'i}S^{\alpha}_{jj'}S^{\beta}_{jj'} + S^{\alpha}_{ij'}S^{\beta}_{j'j}S^{\alpha}_{ji'}S^{\beta}_{ii'}\right) \\ &\quad \times\left\{\frac{\beta^3_{i'}\beta^3_{j'}}{[(\beta_{i'}+(\beta_{j'})/2]^2}N_{i'}N_{j'} - \frac{\beta^3_i\beta^3_j}{[(\beta_{i'}+(\beta_{j'})/2]^2}N_iN_j\right\} \qquad (8.11)\end{aligned}$$

where $\gamma_i = g_2^2\frac{\beta_i}{\hbar}(\frac{m\bar{\omega}}{2\pi\hbar})^3$ is the spin relaxation rate, and $\bar{\omega} = (\omega_x\omega_y\omega_z)^{1/3}$ is the mean frequency of the trap. In reality, there is also atom loss due to the collision to the background gases. Assuming the atom loss of all the spin components m_f are the same, we rewrite the rate equations for each spin component [144] and add the atom loss into the system as

$$\begin{aligned}\frac{dN_1}{dt} &= 4\gamma_1\left\{\frac{\beta_0}{\beta_1}N_0N_0 - \frac{\beta_1^2\beta_{-1}^3}{[(\beta_1+\beta_{-1})/2]^5}N_1N_{-1}\right\} - \frac{1}{\tau}N_1 \\ \frac{dN_0}{dt} &= 8\gamma_0\left\{-N_0N_0 + \frac{\beta_1^3\beta_{-1}^3}{\beta_0[(\beta_1+\beta_{-1})/2]^5}N_1N_{-1}\right\} - \frac{1}{\tau}N_0 \\ \frac{dN_{-1}}{dt} &= 4\gamma_1\left\{\frac{\beta_0}{\beta_{-1}}N_0N_0 - \frac{\beta_1^3\beta_{-1}^2}{[(\beta_1+\beta_{-1})/2]^5}N_1N_{-1}\right\} - \frac{1}{\tau}N_{-1}\end{aligned}$$

This system of equations governs the spin population dynamics of the system. Even though we can not solve for an exact solution, the equilibrium population can be obtained by solving $\frac{dN_1}{dt} = \frac{dN_0}{dt}\frac{dN_{-1}}{dt} = 0$ which gives the solution $N_1 = N_{-1} = \frac{\sqrt{N_0+8\gamma_0\tau N_0^2}}{\sqrt{8\gamma_0\tau}}$. In the case of no atom loss $\tau\to\infty$, the solution is $N_1 : N_0 : N_{-1} = \frac{1}{3} : \frac{1}{3} : \frac{1}{3}$. Numerical integration can be applied to predict the spin population dynamics of the system. In Figure 8.2, we show the simulation comparison of the spin relaxation with the atom loss included and no atom loss included in the simulation. The simulation shows the discrepancy in equilibrium population of atom loss case and no atom loss case.

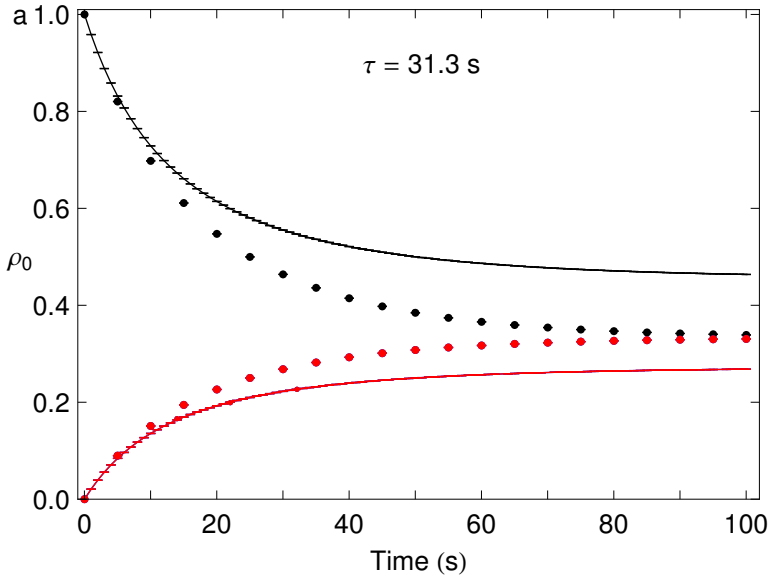

Figure 8.1: Thermal Spin Relaxation Atom Loss vs. No Loss Model. When there is no atom loss (dots), the equilibrium population reaches $\rho_1 : \rho_0 : \rho_{-1} = \frac{1}{3} : \frac{1}{3} : \frac{1}{3}$. When the atom loss (solid line) is included in the model, the equilibrium population for ρ_0 shifts up, and $\rho_{\pm 1}$ shifts down. The population $\rho_0, \rho_1, \rho_{-1}$ are shows in black, blue, red colors.

8.2 Observation of Spin Relaxation

To observe spin relaxation, we prepare all atoms in the $m_f = 0$ state at a high magnetic field of 2 G. The temperature of the atoms is approximately 1.5 μK, above the critical temperature for Bose-Einstein condensation. The magnetic field is then lowered to mG regime for the spinor dynamics to freely evolve. The spinor dynamics occur through the spin exchange of two-body collisions. Finally, the spin populations are measured. This is executed by releasing the trap and allowing the atoms to freely expand in a Stern-Gerlach magnetic field gradient to separate the m_f spin components. For a room temperature gas, the thermal energy is much higher than the Zeeman energy thus the Zeeman sub-levels are degenerate. The spinor relaxation equilibrium thus $\rho_1 : \rho_0 : \rho_{-1} = \frac{1}{3} : \frac{1}{3} : \frac{1}{3}$. For the thermal gas just above BEC critical temperature, the equilibrium spinor population will be different if we take into account of the Zeeman energy from the magnetic field.

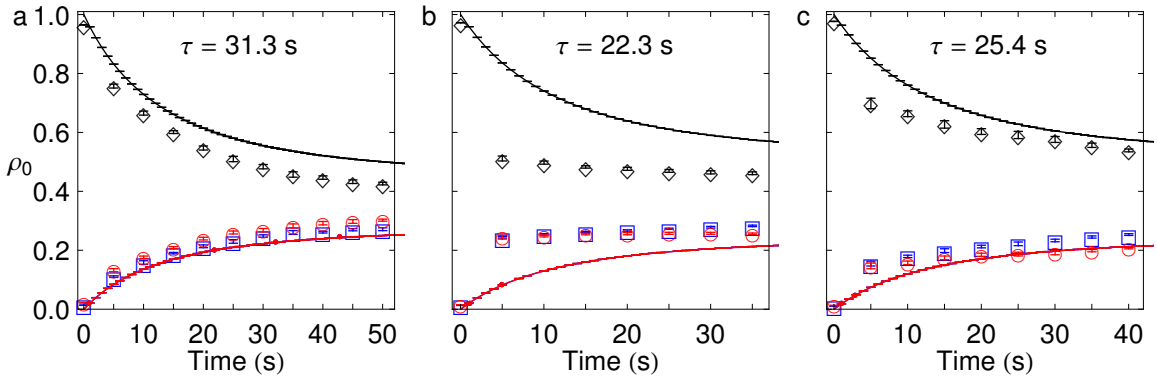

Figure 8.2: Thermal Spin Relaxation. Spin relaxation at (a) 0 mG, (b) 220 mG, (c) and 350 mG. The experimental result of $\rho_0, \rho_1, \rho_{-1}$ (black diamonds, blue squares, red circles) are compared to simulation (same color solid lines).

The thermal spin relaxation for different magnetic fields is shown in Figure 8.2 for (a) 0 mG, (b) 220 mG, (c) and 350 mG. In the case of 0 mG, the equilibrium population $\rho_1 : \rho_0 : \rho_{-1} = \frac{3}{10} : \frac{4}{10} : \frac{3}{10}$. This equilibrium is probably due to the atom loss as discussed previously. The data shows encouraging agreement with the simulation.

The spin relaxation equilibrium changes as we change the magnetic field. However, it is too early to conclude the change in equilibrium population is due to the magnetic field. For a magnetic field of 220 mG and 350 mG the trap lifetimes are 22.3 and 25.4 s; these trap lifetimes significantly change the theoretical equilibrium population $\rho_0 \to 0.6$. For a magnetic field of 350 mG, the data match well to the theory; however, it is not the case for a magnetic field of 220 mG. Note that the theory does not include the effect of the Zeeman energy. The theoretical curves are differently solely due to the trap life time. When the magnetic field is zero, there is no Zeeman energy shift. When the magnetic field is greater than 10 mG, the linear Zeeman energy is comparable to the kinetic energy $k_B T$. However, spin relaxation occurs through spin collisions $2|0\rangle \rightleftharpoons |1\rangle + |-1\rangle$ which cancels linear Zeeman effect. We probably need to include the quadratic Zeeman energy in the Wigner distribution function in Eqn 8.8 in order

describe the thermal spin relaxation. We will revisit this theory in future studies of spin relaxation.

Also, the relaxation rate is varying for different magnetic fields. Around 220 mG, the spin relaxes quickly after 5 s. For a magnetic field of 0 mG and 350 mG, it takes more than 40 s for the spin to reach equilibrium. For the Bose-Einstein condensate, the effect of the magnetic field on the dynamical rate was observed in spin mixing [50, 22, 109]. Whether the magnetic field plays any role in the relaxation rate, it is an interesting question. More data would be necessary in order to have a better understanding of thermal spin relaxation and to have conclusive results.

8.2.1 Technical Problems

Unfortunately, our experiment broke in the middle of the studies. In order to create a pure $m_f = 0$ condensate with the desired number of atoms (1.5×10^5), the gradient coils of 500 A are on for 10 s to clear out unnecessary spin components every experimental run of 30 s. Repeating this procedure (turn on/off high current coils) for a long time probably damages the Insulated-gate bipolar transistor (IGBT) and the control circuit of gradient coils. During my time as a graduate student, the IGBT system has failed at least 3 times.

The IGBT is not the only story. The expansion rate of thermal atoms is unlike a Bose-Einstein condensate; their size expands very large during the time-of-flight (TOF) imaging. Our imaging system was originally designed for imaging the Bose-Einstein condensate which is a very small cloud of atoms. The imaging system barely captures the image of large thermal clouds of atoms. Solving the imaging problem requires a change of the magnification of the imaging system (currently the magnification is 5×) so that the whole thermal cloud can be captured on the camera CCD.

Also, there are three different spin components of $m_f = 0, \pm 1$ which are separated

by Stern-Gerlach gradient coil during imaging. These three clouds of spin components almost overlap on the image. The cloud of atoms expands as fast as the separation rate by the Stern-Gerlach coils. It takes at least 22 ms TOF to separate the spin components; the size of each spin component cloud is large and overlaps each other. To solve this problem, we need to increase the current of our Stern-Gerlach coils so that we can separate the spin component cloud faster and farther. Right now the power supply of the coils is at the limit of 500 A.

The preliminary data shows an interesting result on thermal spin relaxation. Improving the experiment apparatus for thermal spin study is one of our future plans.

CHAPTER 9

CONCLUSION AND FUTURE DIRECTION

We have been focused very deep into the theory and experiments of a spinor Bose-Einstein condensate. In this chapter, we will look at our work from a broader perspective and look forward to the future directions.

9.1 Conclusion

The world has been changing faster than ever, thanks to the development of science and technology. The birth of Newtonian physics in the 17th century has changed how human perceive the world around us: from the apple falling to the Earth, to the orbit of the Earth around the Sun, and even the industrial revolution that changed the world forever. The understanding beyond Newtonian physics has enabled humans to reach further from the Earth, to outside the Solar system, to stars, galaxies and beyond by Einstein's theory of general relativity, and to reach deeper into the smaller and smaller objects at the atom scale and beyond by the theory of quantum physics. One of modern technology's driving forces is to move towards controlling systems at the quantum scale. The ability to control quantum systems is crucial in order to study the system scientifically and extract useful and practical applications. In this thesis, we have demonstrated different quantum control methods in a spin-1 Bose-Einstein condensate, from non-equilibrium dynamics stabilization, parametric excitation, to rectifier phase control of many-body systems. We also extended our study to thermal atoms above the Bose-Einstein transition temperature. They all looked unrelated even to me when I first started the study. How do they combine together to become a tool set for quantum control? The dynamics of a large number of physical systems can be described as the dynamics of a pendulum. There are two

dynamical configurations of a pendulum, an oscillation about the stable equilibrium point ("down" position) called a classical pendulum and a motion about an unstable equilibrium point("up" position). The spinor dynamics of a condensate, depending on the quadratic Zeeman energy (magnetic field strength), have coherent oscillation dynamics like a classical pendulum and non-equilibrium dynamics like an inverted pendulum. The dynamic stabilization controls the non-equilibrium dynamics of a quantum many-body system; this is equivalent to stabilizing an inverted pendulum. The parametric excitation, on the other hand, manipulates the coherent oscillation of spinor condensates; this is equivalent to exciting the oscillation of a classical pendulum. In addition, we demonstrated the rectifier phase method to control coherent oscillations of spinor systems. In a classical pendulum, this is equivalent to the change in the oscillation amplitude by changing the rod length and angle of a pendulum. In many systems, the dynamics can be categorized as either equilibrium dynamics or non-equilibrium dynamics; the control methods demonstrated in this thesis provide a general framework to dynamically control quantum systems. Even though the experiment is carried out in a spin-1 Bose-Einstein condensate, we would see no reason that the idea of dynamical quantum control can not be applied to other systems and other fields, for instance, our neighboring anti-ferromagnetic Bose-Einstein condensate in Prof. Raman's lab.

In addition to Bose-Einstein condensates, we also studied spin relaxation in thermal atoms above the BEC transition temperature. Thermal atoms are easier to produce and have a longer trap lifetime than Bose-Einstein condensates in our system; therefore, the applications for thermal atoms are robust and practical. We are looking forward to carrying on the study of thermal atoms in the future.

9.2 Future Directions

9.2.1 Toward to Double Magneto-Optical Trap BEC

Our Bose-Einstein condensate is created by 3D magneto-optical trap (MOT) set up which is described in the experimental apparatus chapter. One of the disadvantages of the 3D MOT is the loading time. It takes approximate 15 s for the MOT to accumulate enough atoms into the CO_2 dipole trap to make a BEC. The long loading time is due to the low density of gas in the ultra-high vacuum and the high velocity of the gas. For experimental statistics, we normally have to repeat experiment hundreds to thousands times depend on the procedure. The trap loading time adds up very quickly and our data taking process can easily be 24 hours to 48 hours. These hours are nothing if we had a large collaboration like Large Hadron Collide (LHC). However, our experiment is normally run by 2–3 graduate students. If we can increase the data taking speed, we can effectively "work less for more". To improve the trap loading time, we implement a double MOT-BEC [149]. The apparatus setup includes a 2D MOT [150, 151, 152] and a 3D MOT [131]. The 2D MOT traps atoms along the longitudinal axis of the glass rectangular tube acting as a slow atom source for the 3D MOT. The differential pressure hole connects the 2D and 3D MOTs to keep the pressure at the 3D MOT lower than 2D MOT (vapor of atom source). It only takes 1$\sim$2 s to initial load atom into 3D MOT. The implementation of the double MOT BEC thus significantly improves our speed of data taking; moreover, we can implement other improvements learned from the previous setup.

9.2.2 Improve Squeezing

From the study of parametric excitation squeezing, we notice that our measurements are limited by the detection limit which is about -6 dB. In the past, the detection limit was -12 dB. However, due to the background scattering noise of a glowing CO_2 laser lens, the detection limit goes up. The experimental simulation shows

that parametric excitation can generate squeezing up to -20 dB as shown in Figure 7.1. Improving the detection limit will enable us to examine the squeezing level and generates squeezed states from parametric excitation.

9.2.3 Investigate Quantum Phase Transitions

In our study, we focus on two extreme regimes $q < 2|c|$ and $q > 2|c|$. The quantum phase transition (QPT) occurs at $q = 2|c|$ where the ground state experiences an abrupt change [39, 40, 41]. Tuning the value of quadratic Zeeman energy q around the QPT critical point $2|c|$ (by quenching the magnetic field) will enable us to explore the fundamental and universal physical phenomenon in a spinor BEC system.

9.2.4 Thermal Spin Relaxation and Beyond

The preliminary result in thermal spin relaxation has shown a promising result. The dynamics of spin relaxation and the equilibrium population show the dependence on the trap lifetime of condensate. Exploring the dynamics for different magnetic fields would answer our question whether the magnetic fields play a significant role for population equilibrium of the thermal gas above the BEC critical temperature. Since creating a thermal gas above the BEC critical temperature is simpler than making a BEC, it would be convenient to use a thermal gas as a tool to study quantum phenomena and explore their applications.

APPENDIX A

SIMULATION METHOD

The original simulation is written in Mathematica [64]. To increase the computational speed, we rewrote the simulation in C++. Benjamin Land has done a great job in optimizing the code. We will discuss how to perform the simulation.

A.1 Quantum Simulation

The Hamiltonian for spinor BEC can be written in the Fock basis [84, 64]

$$\begin{aligned}\mathcal{H}_{k,k'} &= \left(\lambda_a' M^2 + 2\lambda_a' k(2(N-2k)-1) + q(2k+|M|)\right)\delta_{k,k'+1} \\ &\quad +2\lambda_a' \Big((k'+1)\sqrt{(N-2k')(N-2k'-1)}\delta_{k,k'+1} \\ &\quad +k\sqrt{(N-2k'+1)(N-2k'+2)}\delta_{k,k'-1}\Big) \end{aligned} \tag{A.1}$$

The Hamiltonian $\hat{\mathcal{H}}$ is a symmetric diagonal matrix, everywhere is zero except for the three diagonal terms. The basis of the wave function are represented in the Fock state $|\psi\rangle = |N, M, k\rangle$ where N is the total number of atom, $M = N_1 - N_{-1}$ is the magnetization, and k is the number of pair $m_f = \pm 1$. The wave function can be presented as a vector of $\frac{N}{2}+1$ components, which is the combination of linear independent unit vectors $|k\rangle$.

$$\begin{aligned}|\psi\rangle &= \sum_{k=0}^{\frac{N}{2}+1} a_k(t)|k\rangle \\ |k\rangle &= (0,0,..,k^{th}=1,..,0)^T \qquad k\in[0,\frac{N}{2}]\end{aligned}$$

The time-dependent Shcrödinger equation reads

$$i\hbar\frac{\partial}{\partial t}\psi = \hat{\mathcal{H}}\psi$$

For the condensate where all the atoms are prepared at $m_f = 0$ state, the initial wave function is

$$\psi(0) = |1,\ 0,\ 0,\ ..,\ 0\rangle$$

Applied fourth-order Runge-Kutta method, we can calculate the wave function $\psi(t + dt)$ from $\psi(t)$

$$\psi(t + dt) \quad = \quad \psi(t) + \frac{1}{6} dt(k_1 + 2k_2 + 2k_3 + k_4)$$

where

$$\begin{aligned} k_1 &= \frac{1}{i\hbar}\hat{\mathcal{H}}\psi(t) \\ k_2 &= \frac{1}{i\hbar}\hat{\mathcal{H}}(\psi(t) + \frac{dt}{2}k_1) \\ k_3 &= \frac{1}{i\hbar}\hat{\mathcal{H}}(\psi(t) + \frac{dt}{2}k_2) \\ k_4 &= \frac{1}{i\hbar}\hat{\mathcal{H}}(\psi(t) + dtk_3) \end{aligned}$$

The microwave phase shift rotates the quadrature phase of the condensate in spin-nematic space about the x or $\hat{\mathcal{Q}}_{zz}$ axis. For a quadrature phase shift of $\Delta\theta$, the wave function after phase shift is

$$|\psi(t)\rangle_{\Delta\theta} \quad = \quad e^{-i\hat{\mathcal{Q}}_{zz}\Delta\theta/2}|\psi(t)\rangle = \sum_{k=0}^{N/2} e^{-i2k\Delta\theta} a_k(t)|k\rangle$$

The atom loss is taken into account by changing the spinor dynamical rate $c = c_0(\frac{N(t)}{N})^{-2/5} = c_0 e^{-\frac{2}{5}\frac{t}{\tau}}$ for trap life time τ and spinor dynamical rate $c_0 = 2\lambda'_a N = -7.2(5)$ Hz.

A.2 Semi-Classical Simulation

The semi-classical equation is solved by numerical integrating the coupled Gross-Pitaevskii equations [109].

$$\begin{aligned} i\hbar\frac{\partial\zeta_1}{\partial t} &= E_1\zeta_1 + c\left[(\rho_1-\rho_{-1}+\rho_0)\zeta_1 + \zeta_{-1}^{\dagger}\zeta_0^2\right] \\ i\hbar\frac{\partial\zeta_0}{\partial t} &= E_0\zeta_0 + c\left[(\rho_1+\rho_{-1})\zeta_0 + 2\zeta_0^{\dagger}\zeta_1\zeta_{-1}\right] \\ i\hbar\frac{\partial\zeta_{-1}}{\partial t} &= E_{-1}\zeta_{-1} + c\left[(\rho_{-1}-\rho_1+\rho_0)\zeta_{-1} + \zeta_1^{\dagger}\zeta_0^2\right] \end{aligned} \tag{A.2}$$

The wave equation $\psi = \{\zeta_1, \zeta_0, \zeta_{-1}\} = (\sqrt{\frac{1-\rho_0+m}{2}}e^{i\chi_+}, \rho_0, \sqrt{\frac{1-\rho_0-m}{2}}e^{i\chi_-})^T$ [109, 51, 64] and $\rho_i = \psi_i^{\dagger}\psi_i$ for $i = 0, \pm 1$. To obtain the initial value for $\rho_0,\ m,\ \chi_+,\ \chi_-$, we use the expectation value of the spin and quadrature operators

$$\begin{aligned} \langle S_x\rangle &= \sqrt{2\rho_0\rho_+}\cos\chi_+ + \sqrt{2\rho_0\rho_-}\cos\chi_- \\ \langle Q_{yz}\rangle &= -\sqrt{2\rho_0\rho_+}\sin\chi_+ - \sqrt{2\rho_0\rho_-}\sin\chi_- \\ \langle S_y\rangle &= -\sqrt{2\rho_0\rho_+}\sin\chi_+ + \sqrt{2\rho_0\rho_-}\sin\chi_- \\ \langle Q_{xz}\rangle &= \sqrt{2\rho_0\rho_+}\cos\chi_+ - \sqrt{2\rho_0\rho_-}\cos\chi_- \\ \langle Q_{zz}-Q_{yy}\rangle &= \rho_+ + \rho_- - 2\rho_0 + 2\sqrt{\rho_+\rho_-}\cos\theta_m \\ \langle Q_{xx}-Q_{zz}\rangle &= -\rho_+ - \rho_- + 2\rho_0 + 2\sqrt{\rho_+\rho_-}\cos\theta_m \end{aligned}$$

The magnetization $m = \rho_+ - \rho_- = 0$, thus $\rho_\pm = \frac{1-\rho_0}{2}$. These equations can be simplified as

$$\begin{aligned} \langle S_x\rangle &= 2\sqrt{\rho_0(1-\rho_0)}\cos\frac{\theta_s}{2}\cos\frac{\theta_m}{2} \\ \langle Q_{yz}\rangle &= -2\sqrt{\rho_0(1-\rho_0)}\sin\frac{\theta_s}{2}\cos\frac{\theta_m}{2} \\ \langle S_y\rangle &= -2\sqrt{\rho_0(1-\rho_0)}\cos\frac{\theta_s}{2}\sin\frac{\theta_m}{2} \\ \langle Q_{xz}\rangle &= -2\sqrt{\rho_0(1-\rho_0)}\sin\frac{\theta_s}{2}\sin\frac{\theta_m}{2} \\ \langle Q_{zz}-Q_{yy}\rangle &= \rho_+ + \rho_- - 2\rho_0 + 2\sqrt{\rho_+\rho_-}\cos\theta_m \\ \langle Q_{xx}-Q_{zz}\rangle &= -\rho_+ - \rho_- + 2\rho_0 + 2\sqrt{\rho_+\rho_-}\cos\theta_m \end{aligned} \tag{A.3}$$

Using these equation one can derive the conversion from Fock state for coherent state distribution [64]

$$\begin{aligned}
\tan\chi_+ &= -\frac{S_y+Q_{yz}}{S_x+Q_{yz}} \\
\tan\chi_- &= \frac{S_y-Q_{yz}}{S_x-Q_{yz}} \\
\rho_0 &= \frac{1}{2}+\sqrt{\frac{1}{4}-\frac{1}{8}\left((\frac{S_x+Q_{xz}}{\cos\chi_+})^2+(\frac{S_y+Q_{yz}}{\cos\chi_-})^2\right)} \\
m &= \frac{1}{8\rho}\left((\frac{S_x+Q_{xz}}{\cos\chi_+})^2-(\frac{S_y+Q_{yz}}{\cos\chi_-})^2\right)
\end{aligned} \tag{A.4}$$

The expectation values of S_x, Q_{yz}, S_y, Q_{yz} are zeros, and the variance is N, if we normalize the wave function to 1 the variance then $\frac{1}{N}$. From the spinor dynamic equations, the spin mixing does not occur if we start with the initial state $|m_f=0\rangle$. If there is some fluctuation in the expectation values of S_x, Q_{yz}, S_y, Q_{yz}, the initial state will evolve.

Use this as initial condition, the spinor dynamics can be obtained by the numerical integrating the system of the coupled Gross-Pitaevskii wave equation of Eqn A.2 using fourth-order Runge-Kutta method.

$$\begin{aligned}
\frac{\partial\zeta_1}{\partial t} &= \frac{1}{i\hbar}\left(E_1\zeta_1+c\left[(\rho_1-\rho_{-1}+\rho_0)\zeta_1+\zeta_{-1}^\dagger\zeta_0^2\right]\right)=f_1(\zeta_1,\zeta_0,\zeta_{-1}) \\
\frac{\partial\zeta_0}{\partial t} &= \frac{1}{i\hbar}\left(E_0\zeta_0+c\left[(\rho_1+\rho_{-1})\zeta_0+2\zeta_0^\dagger\zeta_1\zeta_{-1}\right]\right)=f_0(\zeta_1,\zeta_0,\zeta_{-1}) \\
\frac{\partial\zeta_{-1}}{\partial t} &= \frac{1}{i\hbar}\left(E_{-1}\zeta_{-1}+c\left[(\rho_{-1}-\rho_1+\rho_0)\zeta_{-1}+\zeta_1^\dagger\zeta_0^2\right]\right)=f_{-1}(\zeta_1,\zeta_0,\zeta_{-1})
\end{aligned} \tag{A.5}$$

For a condensate prepared in $m_f=0$, the initial wave function $\psi(0)=\{0,\ 1,\ 0\}$ which is equivalent to $\zeta_0(0)=1$ and $\zeta_\pm(0)=0$. We can calculate the wave function $\psi(t+dt)$ from $\psi(t)$

$$\zeta_i(t+dt) = \zeta_i(t)+\frac{1}{6}dt(k_{i,1}+2k_{i,2}+2k_{i,3}+k_{i,4})$$

for $i = 0, \pm 1$ and

$$\begin{aligned}
k_{i,1} &= f_i(\zeta_1(t), \zeta_0(t), \zeta_{-1}(t)) \\
k_{i,2} &= f_i(\zeta_1(t) + \frac{dt}{2}k_{1,1},\ \zeta_0(t) + \frac{dt}{2}k_{0,1},\ \zeta_{-1}(t) + \frac{dt}{2}k_{-1,1}) \\
k_{i,3} &= f_i(\zeta_1(t) + \frac{dt}{2}k_{1,2},\ \zeta_0(t) + \frac{dt}{2}k_{0,2},\ \zeta_{-1}(t) + \frac{dt}{2}k_{-1,2}) \\
k_{i,4} &= f_i(\zeta_1(t) + \frac{dt}{2}k_{1,3},\ \zeta_0(t) + \frac{dt}{2}k_{0,3},\ \zeta_{-1}(t) + \frac{dt}{2}k_{-1,3})
\end{aligned}$$

The atom loss is taken into account by changing the spinor dynamical rate $c = c_0(\frac{N(t)}{N})^{-2/5} = c_0 e^{-\frac{2}{5}\frac{t}{\tau}}$ for trap life time τ and spinor dynamical rate $c_0 = 2\lambda'_a N = -7.2(5)$ Hz.

APPENDIX B

EXPERIMENTAL PARAMETERS

B.1 Table of Physical Constants

Table B.1: Fundamental physical constants (Source: 2010 CODATA)

Constant	Symbol	Value
Atomic Mass Unit	m_u	$1.660538921(73) \times 10^{-27}$ kg
Bohr Radius	a_0	$0.52917721092(17) \times 10^{-}10$ m
Boltzmann Constant	k_B	$1.3806488(13) \times 10^{-23}$ J/K
Bohr Magneton	μ_B	$9.27400968(20) \times 10^{-24}$ J/K
Elementary Charge	e	$1.60217653(14) \times 10^{-19}$ C
Permeability of Vacuum	μ_0	$4\pi \times 10^{-7}$ N/A^2
Permittivity of Vacuum	ϵ_0	$(\mu_0 c^2)^{-1}$
Planck Constant	h	$6.62606957(29) \times 10^{-34}$ J $\cdot$ s
Speed of Light	c	299792458 m $\cdot$ s^{-1}

Table B.2: Rubidium ^{87}Rb Constants (Source: 2010 CODATA and collection from Daniel A. Steck [132]

Constant	Symbol	Value
Atomic number	Z	37
Atomic mass	m	86.909180527(13) m_u
Natural abundance		27.23 %
Nuclear spin	I	3/2
Fine structure landé	g_J	2.002 319 304 373 7(80)
Nuclear g-factor	g_I	-0.000995 141 4(10)
D_2 Wavelength	λ	780.241 209 686(13) nm
D_2 Lifetime	τ	26.24(4) ns
D_2 Decay rate	Γ	$2\pi \cdot 6.6065(9)$ MHz
Linear Zeeman hyperfine $F = 1$	p_1	702.4 Hz/mG
Linear Zeeman Hyperfine $F = 2$	p_2	699.8 Hz/mG
Quadratic Zeeman hyperfine $F = 1$	q_Z	71.6 Hz/G^2

Table B.3: Experimental Parameters

Parameter	Symbol	Value
Number of atom cross trap	N	150×10^3 atoms
Number of atom single focus	N	40×10^3 atoms
Spinor dynamical rate	c	$-7.2(5) \times 2\pi$ Hz
Trap life time	τ	1.8(4) s
radial trap frequency	f_R	245$\sim$ 260 Hz
Cross trap longitudinal trap frequency	f_L	250 Hz
Single focus longitudinal trap frequency	f_L	25 Hz
BEC temperature	T_c	$<$ 300 nK

Table B.4: Formula Symbols

Symbol	Description
$\hat{a}_i^\dagger, \hat{a}_i$	creation/annihilation for $m_f = i$
$\lambda_i' = \lambda_i \int \lvert\psi(\vec{r})d^3r = 2cN$	Mean field two body coupling for channel $i = 0, 2$
$\rho_i = \frac{N_i}{N}$	Fractional population
θ_i	Phase of $m_f = i$
$\theta_s = 2\theta = \theta_1 + \theta_{-1} - 2\theta_0$	Spinor phase/quadrature phase
$a_{F=0} = 101.8(2)a_0$	Scattering length channel 0
$a_{F=2} = 100.4(1)a_0$	Scattering length channel 2
$g_0 = \frac{4\pi\hbar^2}{m}a_0$	g Two-body coupling length channel 0
$g_2 = \frac{4\pi\hbar^2}{m}a_2$	g Two-body coupling length channel 2
$\lambda_s = \frac{2g_2+g_0}{3}$	Density interaction
$\lambda_a = \frac{g_2-g_0}{3}$	Spin interaction

Table B.5: Commutators of the dipole-quadrupole basis [64]. The commutator table is applicable to both the quantum operators and the matrix form. Furthermore the unitary transformation used to go to a rotating frame does not change its structure.

$[\downarrow, \rightarrow]$	S_y	S_z	Q_{yz}	Q_{xz}	Q_{xy}	Q_{xx}	Q_{yy}	Q_{zz}
S_x	iS_z	$-iS_y$	$i(Q_{zz}-Q_{yy})$	$-iQ_{xy}$	iQ_{xz}	0	$2iQ_{yz}$	$-2iQ_{yz}$
S_y		iS_x	iQ_{xy}	$i(Q_{xx}-Q_{zz})$	$-iQ_{yz}$	$-2iQ_{xz}$	0	$2iQ_{xz}$
S_z			$-iQ_{xz}$	iQ_{yz}	$i(Q_{yy}-Q_{xx})$	$2iQ_{xy}$	$-2iQ_{xy}$	0
Q_{yz}				$-iS_z$	iS_y	0	$-2iS_x$	$2iS_x$
Q_{xz}					$-iS_x$	$2iS_y$	0	$-2iS_y$
Q_{xy}						$-2iS_z$	$2iS_z$	0
Q_{xx}							0	0
Q_{yy}								0

REFERENCES

[1] S. Bose, "Plancks Gesetz und Lichtquantenhypothese," *Zeitschrift fr Physik* **26**, 178 (1924).

[2] A. Einstein, "Quantentheorie des einatomigen idealen Gases," *Physikalisch-mathematische Klasse* , 261 (1924).

[3] A. Einstein, "Quantentheorie des einatomigen idealen Gases. 2. Abhandlung," *Physikalisch-mathematische Klasse* , 3 (1924).

[4] M. H. Anderson, J. R. Ensher, M. R. Matthews, C. E. Wieman, and E. A. Cornell, "Observation of Bose-Einstein Condensation in a Dilute Atomic Vapor," *Science* **269**, 198 (1995).

[5] K. B. Davis, M. O. Mewes, M. R. Andrews, N. J. van Druten, D. S. Durfee, D. M. Kurn, and W. Ketterle, "Bose-Einstein Condensation in a Gas of Sodium Atoms," *Phys. Rev. Lett.* **75**, 3969 (1995).

[6] C. C. Bradley, C. A. Sackett, J. J. Tollett, and R. G. Hulet, "Evidence of Bose-Einstein Condensation in an Atomic Gas with Attractive Interactions," *Phys. Rev. Lett.* **75**, 1687 (1995).

[7] M. D. Barrett, J. A. Sauer, and M. S. Chapman, "All-Optical Formation of an Atomic Bose-Einstein Condensate," *Phys. Rev. Lett.* **87**, 010404 (2001).

[8] R. Pathria *Statistical Mechanics*, International series in natural philosophy 1996.

[9] A. Jonquière, "Note on the series $\sum_{n=1}^{\infty} \frac{x^n}{n^s}$. (Note sur la série $\sum_{n=1}^{\infty} \frac{x^n}{n^s}$.)," (1889).

[10] E. A. Cornell, J. R. Ensher, and C. E. Wieman, Report No. cond-mat/9903109, 1999 (unpublished).

[11] F. London, "The-phenomenon of liquid helium and the Bose-Einstein degeneracy," *Nature* **141**, 643 (1938).

[12] C. E. Hecht, "The possible superfluid behaviour of hydrogen atom gases and liquids," *Physica* **25**, 1159 (1959).

[13] W. C. Stwalley and L. H. Nosanow, "Possible "New" Quantum Systems," *Phys. Rev. Lett.* **36**, 910 (1976).

[14] I. F. Silvera and J. T. M. Walraven, "Stabilization of Atomic Hydrogen at Low Temperature," *Phys. Rev. Lett.* **44**, 164 (1980).

[15] W. Hardy, M. Morrow, R. Jochemsen, and A. Berlinsky, "Magnetic resonance of atomic hydrogen at low temperatures," *Physica B+C* **109110**, 1964 (1982).

[16] H. F. Hess, D. A. Bell, G. P. Kochanski, D. Kleppner, and T. J. Greytak, "Temperature and Magnetic Field Dependence of Three-Body Recombination in Spin-Polarized Hydrogen," *Phys. Rev. Lett.* **52**, 1520 (1984).

[17] B. R. Johnson, J. S. Denker, N. Bigelow, L. P. Lévy, J. H. Freed, and D. M. Lee, "Observation of Nuclear Spin Waves in Spin-Polarized Atomic Hydrogen Gas," *Phys. Rev. Lett.* **52**, 1508 (1984).

[18] H. F. Hess, "Evaporative cooling of magnetically trapped and compressed spin-polarized hydrogen," *Phys. Rev. B* **34**, 3476 (1986).

[19] S. Chu, "Nobel Lecture: The manipulation of neutral particles," *Rev. Mod. Phys.* **70**, 685 (1998).

[20] C. N. Cohen-Tannoudji, "Nobel Lecture: Manipulating atoms with photons," *Rev. Mod. Phys.* **70**, 707 (1998).

[21] W. D. Phillips, "Nobel Lecture: Laser cooling and trapping of neutral atoms," *Rev. Mod. Phys.* **70**, 721 (1998).

[22] M.-S. Chang, *Coherent Spin Dynamics of a Spin-1 Bose-Einstein Condensate*, PhD thesis Georgia Institute of Technology Atlanta, USA 2006.

[23] D. G. Fried, T. C. Killian, L. Willmann, D. Landhuis, S. C. Moss, D. Kleppner, and T. J. Greytak, "Bose-Einstein Condensation of Atomic Hydrogen," *Phys. Rev. Lett.* **81**, 3811 (1998).

[24] D. M. Stamper-Kurn, M. R. Andrews, A. P. Chikkatur, S. Inouye, H.-J. Miesner, J. Stenger, and W. Ketterle, "Optical Confinement of a Bose-Einstein Condensate," *Phys. Rev. Lett.* **80**, 2027 (1998).

[25] M. R. Andrews, D. M. Kurn, H.-J. Miesner, D. S. Durfee, C. G. Townsend, S. Inouye, and W. Ketterle, "Propagation of Sound in a Bose-Einstein Condensate," *Phys. Rev. Lett.* **79**, 553 (1997).

[26] M.-O. Mewes, M. R. Andrews, N. J. van Druten, D. M. Kurn, D. S. Durfee, C. G. Townsend, and W. Ketterle, "Collective Excitations of a Bose-Einstein Condensate in a Magnetic Trap," *Phys. Rev. Lett.* **77**, 988 (1996).

[27] D. S. Jin, J. R. Ensher, M. R. Matthews, C. E. Wieman, and E. A. Cornell, "Collective Excitations of a Bose-Einstein Condensate in a Dilute Gas," *Phys. Rev. Lett.* **77**, 420 (1996).

[28] M. R. Matthews, B. P. Anderson, P. C. Haljan, D. S. Hall, C. E. Wieman, and E. A. Cornell, "Vortices in a Bose-Einstein Condensate," *Phys. Rev. Lett.* **83**, 2498 (1999).

[29] K. W. Madison, F. Chevy, W. Wohlleben, and J. Dalibard, "Vortex Formation in a Stirred Bose-Einstein Condensate," *Phys. Rev. Lett.* **84**, 806 (2000).

[30] J. R. Abo-Shaeer, C. Raman, J. M. Vogels, and W. Ketterle, "Observation of Vortex Lattices in Bose-Einstein Condensates," *Science* **292**, 476 (2001).

[31] M. R. Andrews, C. G. Townsend, H.-J. Miesner, D. S. Durfee, D. M. Kurn, and W. Ketterle, "Observation of Interference Between Two Bose Condensates," *Science* **275**, 637 (1997).

[32] I. Bloch, T. W. Hänsch, and T. Esslinger, "Measurement of the spatial coherence of a trapped Bose gas at the phase transition," *Nature* **403**, 166 (2000).

[33] M.-O. Mewes, M. R. Andrews, D. M. Kurn, D. S. Durfee, C. G. Townsend, and W. Ketterle, "Output Coupler for Bose-Einstein Condensed Atoms," *Phys. Rev. Lett.* **78**, 582 (1997).

[34] E. W. Hagley, L. Deng, M. Kozuma, J. Wen, K. Helmerson, S. L. Rolston, and W. D. Phillips, "A Well-Collimated Quasi-Continuous Atom Laser," *Science* **283**, 1706 (1999).

[35] I. Bloch, T. W. Hänsch, and T. Esslinger, "Atom Laser with a cw Output Coupler," *Phys. Rev. Lett.* **82**, 3008 (1999).

[36] B. P. Anderson and M. A. Kasevich, "Macroscopic Quantum Interference from Atomic Tunnel Arrays," *Science* **282**, 1686 (1998).

[37] M. Albiez, R. Gati, J. Fölling, S. Hunsmann, M. Cristiani, and M. K. Oberthaler, "Direct Observation of Tunneling and Nonlinear Self-Trapping in a Single Bosonic Josephson Junction," *Phys. Rev. Lett.* **95**, 010402 (2005).

[38] M. Greiner, O. Mandel, T. Esslinger, T. W. Hänsch, and I. Bloch, "Quantum phase transition from a superfluid to a Mott insulator in a gas of ultracold atoms," *Nature* **415**, 39 (2002).

[39] W. H. Zurek, U. Dorner, and P. Zoller, "Dynamics of a Quantum Phase Transition," *Phys. Rev. Lett.* **95**, 105701 (2005).

[40] B. Damski and W. H. Zurek, "Dynamics of a Quantum Phase Transition in a Ferromagnetic Bose-Einstein Condensate," *Phys. Rev. Lett.* **99**, 130402 (2007).

[41] S. Sachdev *Quantum Phase Transitions* 2001.

[42] J. Stenger, S. Inouye, D. Stamper-Kurn, H.-J. Miesner, A. Chikkatur, and W. Ketterle, "Spin domains in ground-state Bose–Einstein condensates," *Nature* **396**, 345 (1998).

[43] D. M. Stamper-Kurn, H.-J. Miesner, A. P. Chikkatur, S. Inouye, J. Stenger, and W. Ketterle, "Quantum Tunneling across Spin Domains in a Bose-Einstein Condensate," *Phys. Rev. Lett.* **83**, 661 (1999).

[44] S. Inouye, M. Andrews, J. Stenger, H.-J. Miesner, D. Stamper-Kurn, and W. Ketterle, "Observation of Feshbach resonances in a Bose–Einstein condensate," *Nature* **392**, 151 (1998).

[45] H.-J. Miesner, D. M. Stamper-Kurn, J. Stenger, S. Inouye, A. P. Chikkatur, and W. Ketterle, "Observation of Metastable States in Spinor Bose-Einstein Condensates," *Phys. Rev. Lett.* **82**, 2228 (1999).

[46] L. E. Sadler, J. M. Higbie, S. R. Leslie, M. Vengalattore, and D. M. Stamper-Kurn, "Spontaneous symmetry breaking in a quenched ferromagnetic spinor Bose-Einstein condensate," *Nature* **443**, 312 (2006).

[47] E. M. Bookjans, A. Vinit, and C. Raman, "Quantum Phase Transition in an Antiferromagnetic Spinor Bose-Einstein Condensate," *Phys. Rev. Lett.* **107**, 195306 (2011).

[48] D. Stamper-Kurn and M. Ueda, "Spinor Bose gases: Explorations of symmetries, magnetism and quantum dynamics,", 2012.

[49] C. Chin, R. Grimm, P. Julienne, and E. Tiesinga, "Feshbach resonances in ultracold gases," *Rev. Mod. Phys.* **82**, 1225 (2010).

[50] M.-S. Chang, C. D. Hamley, M. D. Barrett, J. A. Sauer, K. M. Fortier, W. Zhang, L. You, and M. S. Chapman, "Observation of Spinor Dynamics in Optically Trapped ^{87}Rb Bose-Einstein Condensates," *Phys. Rev. Lett.* **92**, 140403 (2004).

[51] M.-S. Chang, Q. Qin, W. Zhang, L. You, and M. S. Chapman, "Coherent spinor dynamics in a spin-1 Bose condensate," *Nature Physics* **1**, 111 (2005).

[52] H. Schmaljohann, M. Erhard, J. Kronjäger, M. Kottke, S. van Staa, L. Cacciapuoti, J. J. Arlt, K. Bongs, and K. Sengstock, "Dynamics of $F = 2$ Spinor Bose-Einstein Condensates," *Phys. Rev. Lett.* **92**, 040402 (2004).

[53] J. Kronjäger, C. Becker, M. Brinkmann, R. Walser, P. Navez, K. Bongs, and K. Sengstock, "Evolution of a spinor condensate: Coherent dynamics, dephasing, and revivals," *Phys. Rev. A* **72**, 063619 (2005).

[54] A. T. Black, E. Gomez, L. D. Turner, S. Jung, and P. D. Lett, "Spinor Dynamics in an Antiferromagnetic Spin-1 Condensate," *Phys. Rev. Lett.* **99**, 070403 (2007).

[55] A. Widera, F. Gerbier, S. Fölling, T. Gericke, O. Mandel, and I. Bloch, "Coherent Collisional Spin Dynamics in Optical Lattices," *Phys. Rev. Lett.* **95**, 190405 (2005).

[56] C. D. Hamley, C. S. Gerving, T. M. Hoang, E. M. Bookjans, and M. S. Chapman, "Spin-nematic squeezed vacuum in a quantum gas," *Nature Phys.* **8**, 305 (2012), 10.1038/nphys2245.

[57] C. Gross, T. Zibold, E. Nicklas, J. Estève, and M. K. Oberthaler, "Nonlinear atom interferometer surpasses classical precision limit," *Nature* **464**, 1165 (2010).

[58] M. F. Riedel, P. Böhi, Y. Li, T. W. Hänsch, A. Sinatra, and P. Treutlein, "Atom-chip-based generation of entanglement for quantum metrology," *Nature* **464**, 1170 (2010).

[59] C. Gross, H. Strobel, E. Nicklas, T. Zibold, N. Bar-Gill, G. Kurizki, and M. K. Oberthaler, "Atomic homodyne detection of continuous-variable entangled twin-atom states," *Nature* **480**, 219 (2011).

[60] B. Lücke, M. Scherer, J. Kruse, L. Pezz, F. Deuretzbacher, P. Hyllus, O. Topic, J. Peise, W. Ertmer, J. Arlt, L. Santos, A. Smerzi, and C. Klempt, "Twin Matter Waves for Interferometry Beyond the Classical Limit," *Science* **334**, 773 (2011).

[61] C. S. Gerving, T. M. Hoang, B. J. Land, M. Anquez, C. D. Hamley, and M. S. Chapman, "Non-equilibrium dynamics of an unstable quantum pendulum explored in a spin-1 BoseEinstein condensate," *Nature Communications* **3** (2012).

[62] E. M. Bookjans, C. D. Hamley, and M. S. Chapman, "Strong Quantum Spin Correlations Observed in Atomic Spin Mixing," *Phys. Rev. Lett.* **107**, 210406 (2011).

[63] L.-A. Wu, M. Xiao, and H. J. Kimble, "Squeezed states of light from an optical parametric oscillator," *J. Opt. Soc. Am. B* **4**, 1465 (1987).

[64] C. D. Hamley, *Spin-Nematic Squeezing in a Spin-1 Bose-Einstein Condensate*, PhD thesis Georgia Institute of Technology Atlanta, USA 2012.

[65] D. F. Walls and G. Milburn *Quantum optics*, Springer Study Edition 1995.

[66] K. Wódkiewicz and J. H. Eberly, "Coherent states, squeezed fluctuations, and the SU(2) and SU(1,1) groups in quantum-optics applications," *J. Opt. Soc. Am. B* **2**, 458 (1985).

[67] M. Kitagawa and M. Ueda, "Squeezed spin states," *Phys. Rev. A* **47**, 5138 (1993).

[68] I. Bloch, J. Dalibard, and W. Zwerger, "Many-body physics with ultracold gases," *Rev. Mod. Phys.* **80**, 885 (2008).

[69] J. Ma, X. Wang, C. Sun, and F. Nori, "Quantum spin squeezing," *Physics Reports* **509**, 89 (2011).

[70] S. L. Braunstein and P. van Loock, "Quantum information with continuous variables," *Rev. Mod. Phys.* **77**, 513 (2005).

[71] A. Stepheson, "On induced stability," *Philosophical Magazine* **15**, 233 (1908).

[72] W. Paul, "Electromagnetic traps for charged and neutral particles," *Rev. Mod. Phys.* **62**, 531 (1990).

[73] E. D. Courant, M. S. Livingston, and H. S. Snyder, "The Strong-Focusing Synchroton⁻A New High Energy Accelerator," *Phys. Rev.* **88**, 1190 (1952).

[74] H. Saito and M. Ueda, "Dynamically Stabilized Bright Solitons in a Two-Dimensional Bose-Einstein Condensate," *Phys. Rev. Lett.* **90**, 040403 (2003).

[75] H. Saito, R. G. Hulet, and M. Ueda, "Stabilization of a Bose-Einstein droplet by hyperfine Rabi oscillations," *Phys. Rev. A* **76**, 053619 (2007).

[76] R. L. Compton, Y.-J. Lin, K. Jiménez-García, J. V. Porto, and I. B. Spielman, "Dynamically slowed collapse of a Bose-Einstein condensate with attractive interactions," *Phys. Rev. A* **86**, 063601 (2012).

[77] W. Zhang, B. Sun, M. S. Chapman, and L. You, "Localization of spin mixing dynamics in a spin-1 Bose-Einstein condensate," *Phys. Rev. A* **81**, 033602 (2010).

[78] N. Bar-Gill, G. Kurizki, M. Oberthaler, and N. Davidson, "Dynamic control and probing of many-body decoherence in double-well Bose-Einstein condensates," *Phys. Rev. A* **80**, 053613 (2009).

[79] E. Boukobza, M. G. Moore, D. Cohen, and A. Vardi, "Nonlinear Phase Dynamics in a Driven Bosonic Josephson Junction," *Phys. Rev. Lett.* **104**, 240402 (2010).

[80] F. Sols and S. Kohler, "Shapiro resonances in an isolated ac-driven double Bose-Einstein condensate," *Laser Physics* **14**, 1259 (2004).

[81] A. Zenesini, H. Lignier, D. Ciampini, O. Morsch, and E. Arimondo, "Coherent Control of Dressed Matter Waves," *Phys. Rev. Lett.* **102**, 100403 (2009).

[82] T. M. Hoang, C. S. Gerving, B. J. Land, M. Anquez, C. D. Hamley, and M. S. Chapman, "Dynamic Stabilization of a Quantum Many-Body Spin System," *Phys. Rev. Lett.* **111**, 090403 (2013).

[83] L.-M. Duan, J. I. Cirac, and P. Zoller, "Quantum entanglement in spinor Bose-Einstein condensates," *Phys. Rev. A* **65**, 033619 (2002).

[84] C. K. Law, H. Pu, and N. P. Bigelow, "Quantum Spins Mixing in Spinor Bose-Einstein Condensates," *Phys. Rev. Lett.* **81**, 5257 (1998).

[85] C. Klempt, O. Topic, G. Gebreyesus, M. Scherer, T. Henninger, P. Hyllus, W. Ertmer, L. Santos, and J. J. Arlt, "Multiresonant Spinor Dynamics in a Bose-Einstein Condensate," *Phys. Rev. Lett.* **103**, 195302 (2009).

[86] R. Ernst, G. Bodenhausen, and A. Wokaun *Principles of Nuclear Magnetic Resonance in One and Two Dimensions* 1987.

[87] L. Viola and S. Lloyd, "Dynamical suppression of decoherence in two-state quantum systems," *Phys. Rev. A* **58**, 2733 (1998).

[88] M. Faraday, "On a Peculiar Class of Acoustical Figures; and on Certain Forms Assumed by Groups of Particles upon Vibrating Elastic Surfaces," *Philosophical Transactions of the Royal Society of London* **121**, 299 (1831) http://rstl.royalsocietypublishing.org/content/121/299.full.pdf+html.

[89] L. Rayleigh, "XXXIII. On maintained vibrations," *Philosophical Magazine Series 5* **15**, 229 (1883).

[90] E. I. Butikov, "Parametric excitation of a linear oscillator," *European Journal of Physics* **25**, 535 (2004).

[91] D. Terwagne and J. W. M. Bush, "Tibetan singing bowls," *Nonlinearity* **24**, R51 (2011).

[92] S. Shapiro, "Josephson Currents in Superconducting Tunneling: The Effect of Microwaves and Other Observations," *Phys. Rev. Lett.* **11**, 80 (1963).

[93] N. F. Pedersen, M. R. Samuelsen, and K. Saermark, "Parametric excitation of plasma oscillations in Josephson Junctions," *Journal of Applied Physics* **44**, 5120 (1973).

[94] C. K. Bak, B. Kofoed, N. F. Pedersen, and K. Saermark, "Parametric excitation of plasma oscillations in a Josephson tunnel junction," *Journal of Applied Physics* **46**, 886 (1975).

[95] B. Josephson, "Possible new effects in superconductive tunnelling," *Physics Letters* **1**, 251 (1962).

[96] A. Eckardt, T. Jinasundera, C. Weiss, and M. Holthaus, "Analog of Photon-Assisted Tunneling in a Bose-Einstein Condensate," *Phys. Rev. Lett.* **95**, 200401 (2005).

[97] R. Ma, M. E. Tai, P. M. Preiss, W. S. Bakr, J. Simon, and M. Greiner, "Photon-Assisted Tunneling in a Biased Strongly Correlated Bose Gas," *Phys. Rev. Lett.* **107**, 095301 (2011).

[98] Y.-A. Chen, S. Nascimbène, M. Aidelsburger, M. Atala, S. Trotzky, and I. Bloch, "Controlling Correlated Tunneling and Superexchange Interactions with ac-Driven Optical Lattices," *Phys. Rev. Lett.* **107**, 210405 (2011).

[99] C. Sias, H. Lignier, Y. P. Singh, A. Zenesini, D. Ciampini, O. Morsch, and E. Arimondo, "Observation of Photon-Assisted Tunneling in Optical Lattices," *Phys. Rev. Lett.* **100**, 040404 (2008).

[100] V. V. Ivanov, A. Alberti, M. Schioppo, G. Ferrari, M. Artoni, M. L. Chiofalo, and G. M. Tino, "Coherent Delocalization of Atomic Wave Packets in Driven Lattice Potentials," *Phys. Rev. Lett.* **100**, 043602 (2008).

[101] A. Alberti, V. Ivanov, G. Tino, and G. Ferrari, "Engineering the quantum transport of atomic wavefunctions over macroscopic distances," *Nature Physics* **5**, 547 (2009).

[102] E. Haller, R. Hart, M. J. Mark, J. G. Danzl, L. Reichsöllner, and H.-C. Nägerl, "Inducing Transport in a Dissipation-Free Lattice with Super Bloch Oscillations," *Phys. Rev. Lett.* **104**, 200403 (2010).

[103] C. Pethick and H. Smith *Bose-Einstein Condensation in Dilute Gases* 2001.

[104] L. Pitaevskii and S. Stringari *Bose-Einstein Condensation*, International Series of Monographs on Physics 2003.

[105] T.-L. Ho, "Spinor Bose Condensates in Optical Traps," *Phys. Rev. Lett.* **81**, 742 (1998).

[106] H. Pu, C. K. Law, S. Raghavan, J. H. Eberly, and N. P. Bigelow, "Spin-mixing dynamics of a spinor Bose-Einstein condensate," *Phys. Rev. A* **60**, 1463 (1999).

[107] T. Ohmi and K. Machida, "Bose-Einstein Condensation with Internal Degrees of Freedom in Alkali Atom Gases," *Journal of the Physical Society of Japan* **67**, 1822 (1998).

[108] S. Yi, O. E. Müstecaplıoğlu, C. P. Sun, and L. You, "Single-mode approximation in a spinor-1 atomic condensate," *Phys. Rev. A* **66**, 011601 (2002).

[109] W. Zhang, D. L. Zhou, M.-S. Chang, M. S. Chapman, and L. You, "Coherent spin mixing dynamics in a spin-1 atomic condensate," *Phys. Rev. A* **72**, 013602 (2005).

[110] G. I. Mias, N. R. Cooper, and S. M. Girvin, "Quantum noise, scaling, and domain formation in a spinor Bose-Einstein condensate," *Phys. Rev. A* **77**, 023616 (2008).

[111] M. Planck, "On the Law of Distribution of Energy in the Normal Spectrum," *Annalen der Physik* **4**, 553 (1901).

[112] G. Baym and C. J. Pethick, "Ground-State Properties of Magnetically Trapped Bose-Condensed Rubidium Gas," *Phys. Rev. Lett.* **76**, 6 (1996).

[113] F. Dalfovo and S. Stringari, "Bosons in anisotropic traps: Ground state and vortices," *Phys. Rev. A* **53**, 2477 (1996).

[114] K. M. Jones, E. Tiesinga, P. D. Lett, and P. S. Julienne, "Ultracold photoassociation spectroscopy: Long-range molecules and atomic scattering," *Rev. Mod. Phys.* **78**, 483 (2006).

[115] J. D. Sau, S. R. Leslie, M. L. Cohen, and D. M. Stamper-Kurn, "Spin squeezing of high-spin, spatially extended quantum fields," *New Journal of Physics* **12**, 085011 (2010).

[116] I. Carusotto and E. J. Mueller, "Imaging of spinor gases," *Journal of Physics B: Atomic, Molecular and Optical Physics* **37**, S115 (2004).

[117] J. Vanier and C. Audoin *The quantum physics of atomic frequency standards*, , The Quantum Physics of Atomic Frequency Standards No. v. 1 1989.

[118] D. R. Romano and E. J. V. de Passos, "Population and phase dynamics of $F = 1$ spinor condensates in an external magnetic field," *Phys. Rev. A* **70**, 043614 (2004).

[119] F. Bloch, "Nuclear Induction," *Phys. Rev.* **70**, 460 (1946).

[120] G. J. Milburn, J. Corney, E. M. Wright, and D. F. Walls, "Quantum dynamics of an atomic Bose-Einstein condensate in a double-well potential," *Phys. Rev. A* **55**, 4318 (1997).

[121] A. Vardi and J. R. Anglin, "Bose-Einstein Condensates beyond Mean Field Theory: Quantum Backreaction as Decoherence," *Phys. Rev. Lett.* **86**, 568 (2001).

[122] T. Zibold, E. Nicklas, C. Gross, and M. K. Oberthaler, "Classical Bifurcation at the Transition from Rabi to Josephson Dynamics," *Phys. Rev. Lett.* **105**, 204101 (2010).

[123] S. Raghavan, A. Smerzi, S. Fantoni, and S. R. Shenoy, "Coherent oscillations between two weakly coupled Bose-Einstein condensates: Josephson effects, Pi oscillations, and macroscopic quantum self-trapping," *Phys. Rev. A* **59**, 620 (1999).

[124] A. J. Leggett, "Bose-Einstein condensation in the alkali gases: Some fundamental concepts," *Rev. Mod. Phys.* **73**, 307 (2001).

[125] A. Smerzi, S. Fantoni, S. Giovanazzi, and S. R. Shenoy, "Quantum Coherent Atomic Tunneling between Two Trapped Bose-Einstein Condensates," *Phys. Rev. Lett.* **79**, 4950 (1997).

[126] J. Ruostekoski and D. F. Walls, "Bose-Einstein condensate in a double-well potential as an open quantum system," *Phys. Rev. A* **58**, R50 (1998).

[127] R. Gati and M. K. Oberthaler, "A bosonic Josephson junction," *Journal of Physics B: Atomic, Molecular and Optical Physics* **40**, R61 (2007).

[128] M. D. Barrett, *A QUEST for BEC: an all optical alternative*, PhD thesis Georgia Institute of Technology Atlanta, USA 2002.

[129] E. M. Bookjans, *Relative number squeezing in a Spin-1 Bose-Einstein condensate*, PhD thesis Georgia Institute of Technology Atlanta, USA 2010.

[130] C. S. Gerving, *Dynamics of a Quantum Inverted Pendulum Explored in a Spin-1 BEC*, PhD thesis Georgia Institute of Technology Atlanta, USA 2013.

[131] E. L. Raab, M. Prentiss, A. Cable, S. Chu, and D. E. Pritchard, "Trapping of Neutral Sodium Atoms with Radiation Pressure," *Phys. Rev. Lett.* **59**, 2631 (1987).

[132] D. A. Steck, "Rubidium 87 D Line Data,".

[133] G. Barwood, P. Gill, and W. Rowley, "Frequency measurements on optically narrowed Rb-stabilised laser diodes at 780 nm and 795 nm," *Applied Physics B* **53**, 142 (1991).

[134] S. Bize, Y. Sortais, M. S. Santos, C. Mandache, A. Clairon, and C. Salomon, "High-accuracy measurement of the 87 Rb ground-state hyperfine splitting in an atomic fountain," *EPL (Europhysics Letters)* **45**, 558 (1999).

[135] G. Audi, O. Bersillon, J. Blachot, and A. Wapstra, "The Nubase evaluation of nuclear and decay properties," *Nuclear Physics A* **729**, 3 (2003), ¡ce:title¿The 2003 NUBASE and Atomic Mass Evaluations¡/ce:title¿.

[136] R. Grimm, M. Weidemller, and Y. B. Ovchinnikov, "Optical Dipole Traps for Neutral Atoms,", volume 42 of *Advances In Atomic, Molecular, and Optical Physics* pp. 95 – 170 Academic Press 2000.

[137] H. Metcalf and P. Van der Straten *Laser cooling and trapping*, Graduate Texts in Contemporary Physics Series 1999.

[138] S. Giovanazzi, A. Smerzi, and S. Fantoni, "Josephson effects in dilute Bose-Einstein condensates," *Phys. Rev. Lett.* **84**, 4521 (2000).

[139] L. Landau and E. Lifshitz *Mechanics*, Course of theoretical physics 1976.

[140] P. L. Kapitza, "Dynamic stability of a pendulum when its point of suspension vibrates," *Soviet Phys. JETP* **21**, 588 (1951).

[141] S. Vega and A. Pines, "Operator formalism for double quantum NMR," *The Journal of Chemical Physics* **66**, 5624 (1977).

[142] W. Kaiser and C. G. B. Garrett, "Two-Photon Excitation in CaF_2: Eu^{2+}," *Phys. Rev. Lett.* **7**, 229 (1961).

[143] C. Klempt, O. Topic, G. Gebreyesus, M. Scherer, T. Henninger, P. Hyllus, W. Ertmer, L. Santos, and J. J. Arlt, "Parametric Amplification of Vacuum Fluctuations in a Spinor Condensate," *Phys. Rev. Lett.* **104**, 195303 (2010).

[144] Y. Endo and T. Nikuni, "Population Dynamics of a Spin-1 Bose Gas above the Bose–Einstein Transition Temperature," *Journal of the Physical Society of Japan* **78**, 094005 (2009).

[145] M. Erhard, H. Schmaljohann, J. Kronjäger, K. Bongs, and K. Sengstock, "Bose-Einstein condensation at constant temperature," *Phys. Rev. A* **70**, 031602 (2004).

[146] H. K. Pechkis, J. P. Wrubel, A. Schwettmann, P. F. Griffin, R. Barnett, E. Tiesinga, and P. D. Lett, "Spinor Dynamics in an Antiferromagnetic Spin-1 Thermal Bose Gas," *Phys. Rev. Lett.* **111**, 025301 (2013).

[147] Y. Endo and T. Nikuni, "Spin Dynamics of a Trapped Spin-1 Bose Gas above the Bose-Einstein Transition Temperature," *Journal of Low Temperature Physics* **152**, 21 (2008).

[148] E. Wigner, "On the Quantum Correction For Thermodynamic Equilibrium," *Phys. Rev.* **40**, 749 (1932).

[149] S. Dorscher, A. Thobe, B. Hundt, A. Kochanke, R. L. Targat, P. Windpassinger, C. Becker, and K. Sengstock, "Creation of quantum-degenerate gases of ytterbium in a compact 2D-/3D-magneto-optical trap setup," *Review of Scientific Instruments* **84**, 043109 (2013).

[150] E. Riis, D. S. Weiss, K. A. Moler, and S. Chu, "Atom funnel for the production of a slow, high-density atomic beam," *Phys. Rev. Lett.* **64**, 1658 (1990).

[151] J. Nellessen, J. Werner, and W. Ertmer, "Magneto-optical compression of a monoenergetic sodium atomic beam," *Optics Communications* **78**, 300 (1990).

[152] J. Yu, J. Djemaa, P. Nosbaum, and P. Pillet, "Funnel with orientated Cs atoms," *Optics Communications* **112**, 136 (1994).